Properties of convective gravity waves derived by combining global modeling and satellite observations

Quang Thai Trinh

Dissertation

zur Erlangung des Grades
Doktor der Naturwissenschaften (Dr. rer. nat.)

vorgelegt der

Bergischen Universität Wuppertal
Fakultät für Mathematik und Naturwissenschaften
Wuppertal, 2016

Properties of convective gravity waves derived by combining global modeling and satellite observations

Quang Thai Trinh

Abstract

Gravity waves play the key role in the dynamics of the middle atmosphere. Among different gravity wave sources, convection has been long accepted as one of the most prominent ones. However, due to the broad spectrum of convective gravity waves and limitations of current observation techniques, the contribution of these waves to atmospheric dynamics is still an open issue. Moreover, due to the same reasons, the horizontal and temporal scales of gravity waves forced by convection are not well known. These scales are usually treated in current convective gravity wave parameterizations as free parameters and they are defined by assuming typical scales of convective systems. In this study, we addressed these issues using a unique approach of combining modeling and measurements. In order to determine the scales of convective gravity waves, instead of assuming typical scales of convective systems, a systematic survey varying the spatial and temporal scales as free parameters of the Yonsei convective gravity wave source (CGWS) scheme is performed. Gravity waves are generated using this CGWS scheme and propagated upward using the Gravity wave Regional Or Global RAy Tracer (GROGRAT). Gravity wave momentum flux spectra in terms of horizontal and vertical wave numbers are calculated from simulations and compared with the respective spectrum observed by the High Resolution Dynamics Limb Sounder (HIRDLS). Based on this comparison, combinations of scale sets which reproduce the observed gravity wave spectrum are selected.

HIRDLS can only see a limited portion of the gravity wave spectrum due to visibility effects and observation geometry. To allow for a meaningful comparison of simulated gravity waves to observations a comprehensive filter that mimics the instrument limitations is applied to the simulated waves. This comprehensive observational filter takes into account both instrument visibility due to radiative transfer and retrieval as well as the complex observation geometry.

In order to analyze the contribution of convective gravity waves to the atmospheric dynamics, the zonal momentum balance is considered in vertical cross sections of gravity wave momentum flux (GWMF) and gravity wave drag (GWD), and consistency between model results and HIRDLS observations is found. Global maps of the horizontal distribution of GWMF are considered and good agreement in the structure as well as the magnitude between simulated results and HIRDLS observations is found. In particular, main convection hot spots are well repro-

duced. In addition, the latitude dependence of the zonal phase speed spectrum of GWMF and its change with altitude is shown. The latitude dependences for different climate conditions and different altitudes show a main peak in the tropics and summer subtropics associated with eastward phase speeds between several m/s and about 30 m/s.

The current study is unique in two aspects: the complexity and comprehensiveness of the observational filter and the fact that the model spectral distribution is determined merely from observed spectral distributions. In advance to previous studies, the spatial distribution is used only afterwards for validation. Due to the limitation of HIRDLS instrument, only long horizontal wavelength waves are addressed in the current approach. However, the momentum flux of these waves are found to be significant and relevant for the driving of the Quasi-Biennial Oscillation (QBO). Findings of the current study therefore provide the key information for estimating relative contributions of different convective gravity wave scales to the whole convective gravity wave spectrum.

Contents

Chapter 1

Introduction

Atmospheric gravity waves play an important role in the dynamics of the middle atmosphere (e.g. *McLandress*, 1998; *McIntyre*, 1998; *Kim et al.*, 2003; *Alexander et al.*, 2010). Due to this importance, the number of studies focusing on gravity waves has been growing over the last decades. Gravity waves are usually generated in the troposphere by various sources, such as orography, convection, or spontaneous adjustment of jet streams. While propagating upwards, the wave amplitude increases due to the exponential decline of the atmospheric air density. This amplitude increase continues until the amplitude saturation level is reached, where gravity waves break, deposit momentum and accelerate or decelerate the background flow. This process strongly depends on the refraction of the gravity waves by the background wind field, thus forming a two-way interaction between mean winds and gravity waves. Hence, gravity waves significantly affect the global circulation, for instance the quasi-biennial oscillation (QBO), the semiannual oscillation (SAO), wind reversals in the mesosphere and lower thermosphere, and the summer time branch of the stratospheric Brewer–Dobson circulation.

The QBO is the oscillation of the zonal wind in the tropical stratosphere, which has a period of about 28 months. The QBO is important for atmospheric dynamics due to its significant influence on the tracer transport (*Huang et al.*, 2008; *Punge et al.*, 2009; *Shu et al.*, 2012; *Khosrawi et al.*, 2013), on sudden stratospheric warmings (e.g. *Pascoe et al.*, 2006), as well as weather in the troposphere and even at the surface (*Ebdon*, 1975; *Boer and Hamilton*, 2008; *Marshall and Scaife*, 2009). Contribution of gravity waves to the QBO driving is significant and can be seen in both simulations and observations. For example, using numerical simulation, *Dunkerton* (1997) showed that the dynamics of the QBO cannot be realistically reproduced without considering intermediate inertia-gravity waves and mesocale gravity waves. In order to estimate the contribution from different wave scales to the QBO dynamics, *Ern and Preusse* (2009) analyzed temperature data from the Sounding of the Atmosphere using Broadband Emission Radiometry (SABER) satellite instrument and temperature data from European Centre for Medium-Range Weather Forecasts (ECMWF). Their analysis indicated that about 30–50% of the observed wind reversal and only 20–35% of the expected total wave forcing is

contributed by Kelvin waves. This implies that the larger part of the wave forcing has to be attributed to other waves, likely mesocale gravity waves. Further studies demonstrating the important contribution of gravity waves to the QBO driving can be found in *Alexander and Ortland* (2010); *Evan et al.* (2012); *Ern et al.* (2014).

The semiannual oscillation (SAO) is the oscillation of the zonal mean zonal wind in the equatorial upper stratosphere and lower mesosphere which has a period of 6 months. Similar to the QBO, the SAO plays a significant role in the tracer transport in the stratosphere (*Gray and Pyle*, 1986; *Huang et al.*, 2008; *Shu et al.*, 2012) and in the timing of sudden stratospheric warmings (e.g. *Pascoe et al.*, 2006). Contribution of gravity waves to the SAO driving was first studied by *Dunkerton* (1982). His theoretical study suggested that momentum deposition by the selective transmission of vertically-propagating gravity waves and Kelvin waves is the major driver of the SAO observed near the tropical mesopause. On the other hand, an observational study of *Hitchman and Leovy* (1988) showed that Kelvin waves contribute about 30%–70% to the total forcing near the stratopause level. With that estimate, *Hitchman and Leovy* (1988) proposed that the missing forcing of the SAO at the stratopause level may be related to small-scale gravity waves, which were not resolved by the general circulation models. The suggestion of *Dunkerton* (1982) and *Hitchman and Leovy* (1988) about the important role of gravity waves in driving the SAO was strengthened by later studies of *Sassi et al.* (1993); *Sassi and Garcia* (1994); *Hamilton et al.* (1995) and *Burrage et al.* (1996). In particular, using an equatorial beta-plane model, *Sassi and Garcia* (1997) showed that near the stratopause, between 25% and 50% of the forcing of the westerly SAO phase is provided by intermediate-scale Kelvin and inertia–gravity waves. In the mesosphere, contribution by intermediate-scale waves to the westerly SAO phase is even larger. Moreover, these intermediate-scale waves are suggested to be the only driver of the easterly SAO phase in the mesosphere. These results were supported later by observational studies (e.g. *Ern et al.*, 2015) as well as several model studies (*Scaife et al.*, 2002; *Osprey et al.*, 2010; *Peña-Ortiz et al.*, 2010).

The mesosphere and lower thermosphere (MLT) reversals of the zonal wind wind, the pole to pole circulation in the mesosphere, and the cold summer mesopause were puzzling issues of atmospheric research for a long time until the theoretical study of (*Lindzen*, 1981) successfully explained the mesospheric wind reversals by introducing acceleration induced by gravity waves. Based on Lindzen's theory, simulations conducted by *Matsuno* (1982) showed a deceleration of the mesospheric wind and a reverse of flow near and above the mesopause level caused by momentum flux deposited by gravity waves. This momentum flux deposition, consequently, drives the circulation from the summer pole to the winter pole in the mesosphere. This circulation increases the upward motion at the summer pole and downward motion at the winter pole. Over the summer pole, upwelling air expands and cools causing the temperature to drop. On the other hand, downwelling air over the winter pole leads to compression and hence, increase in temperature at the winter mesopause. This leads to a temperature gradient, with highest temper-

ature at the winter pole and lowest temperature at the summer pole. The latter is place of the coldest temperatures on the Earth and is known as the cold summer mesopause (e.g., *Björn*, 1984). An observational evidence for these theoretical assumptions or models can be found, for example, in *Ern et al.* (2013).

By the same driving mechanism as in the mesosphere, wave-induced acceleration significantly impacts global circulations in the stratosphere. In particular, gravity waves are widely accepted as the main driver of the summer-time branch of the stratospheric Brewer–Dobson circulation (e.g. *Rosenlof*, 1996; *Alexander and Rosenlof*, 1996, 2003). The winter-time branch of the Brewer–Dobson circulation is mostly driven by planetary waves. However, as predicted by general circulation models, gravity waves may significantly contribute to the trend of this winter-time branch in a warming climate (*Garcia and Randel*, 2008; *Li et al.*, 2008; *McLandress and Shepherd*, 2009; *Butchart et al.*, 2010).

Another important impact of gravity waves is their influence on atmospheric chemistry. For instance, gravity waves significantly influence the formation of polar stratospheric clouds (PSCs). These PSCs cause the ozone depletion in the winter polar vortex as they activate chemical reactions of chlorine substances (*Solomon et al.*, 1986). The PSCs are typically formed at very low temperature resulting from stable vortex conditions. However, in the presence of gravity waves, temperature decreases locally and PSCs can be formed at higher background temperature (*McDonald et al.*, 2009; *Carslaw et al.*, 1999). This happens particularly in the polar regions over gravity wave hotspots due to two reasons: (1) the background temperature hovers slightly above the model temperature threshold to form PSCs, and (2) strong gravity wave activity leads to sufficiently large temperature perturbations, which cause the temperature to fall below the threshold.

In another example, simulations by *Garcia and Solomon* (1985) showed that seasonal behavior of the eddy diffusion resulted from gravity wave breaking considerably impacts the distribution of chemical species in the mesosphere and lower thermosphere. *Garcia and Solomon* (1985) validated their simulation with observations from airglow emissions and an excellent agreement was found.

Figure 1.1 summaries the above detailed ways of gravity wave impacting on atmospheric dynamics as well as atmospheric chemistry. In particular, gravity waves contribute significantly to the driving of the QBO, SAO in the tropics. In the stratosphere, together with planetary waves, gravity waves provide important forcing for driving stratospheric branches of the Brewer–Dobson circulation, particularly for the summertime branch. In the mesosphere, where most of the gravity wave breaking occurs, they are assumed to be the main driver of the mesospheric branch of the Brewer–Dobson circulation. Moreover, gravity waves cause the cold summer mesopause and strongly influence the formation of PSCs in the winter polar vortex. Via the QBO and downward coupling processes, gravity waves can significantly impact the troposphere as well as weather on the Earth's surface (e.g. *Holton and Tan*, 1980).

Gravity waves can be generated by different sources. Among various sources of gravity waves, convection has been long recognized as one of the most prominent

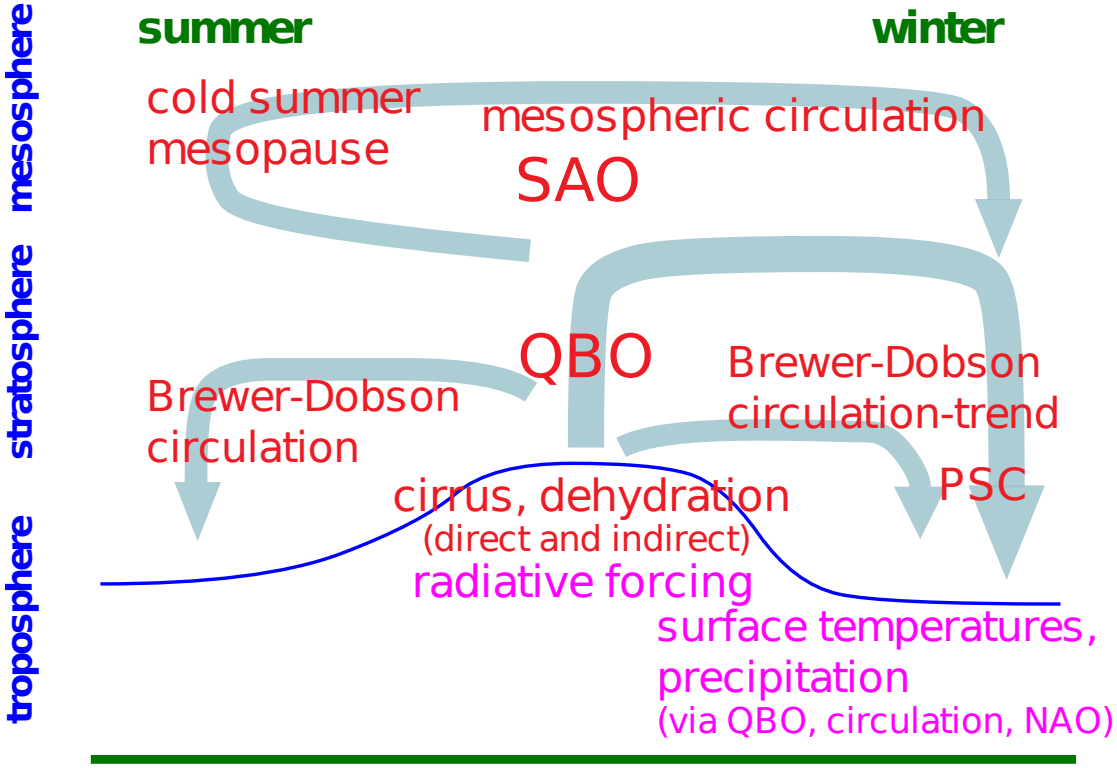

Figure 1.1: Impact of gravity waves on the dynamics and chemistry of the middle atmosphere. Gravity waves contribute significantly to the driving of the QBO and SAO in the tropics. In the stratosphere, together with planetary waves, gravity waves provide important forcing for driving the Brewer–Dobson circulation, particularly for driving the summertime branch and a predicted trend due to climate change. In the mesosphere, gravity waves are assumed to be the main driver of the Brewer–Dobson circulation. Thereby, gravity waves cause the cold summer mesopause. In addition, gravity waves strongly influence the formation of PSCs in the winter polar vortex. Via the QBO and other downward coupling processes, gravity waves can significantly impact the troposphere and surface weather. (Adapted from *Preusse et al.* (2012))

sources, particularly at low latitudes, where cumulus clouds are commonly found. Therefore, convective gravity waves are expected to play a key role in the driving of tropical processes such as the QBO and the SAO. Furthermore, satellite observations show evidence of poleward propagation of convective gravity waves (e.g. *Ern et al.*, 2004, 2011). Hence, convective gravity waves likely also contribute to the cold summer mesospause and the driving of the Brewer–Dobson circulation in the mesosphere. Moreover, observational and numerical modeling studies (e.g. *Sato*, 1993; *Alexander and Pfister*, 1995; *Vincent and Alexander*, 2000; *Beres et al.*, 2002) have indicated that momentum flux of convective gravity waves can be as high as 0.01-0.1 Pa, which is comparable to momentum flux from orographic gravity waves at high winter latitudes. This implies a substantial eddy momentum forcing to the large-scale flow supplied by these convective gravity waves when they are dissipating or breaking. This important role of convective gravity waves in the global-scale dynamics makes convective gravity waves a topic of special interest. However, current non-orographic gravity wave parameterizations do not allow for feedback of sources with weather and climate. Therefore, physical parameters are desired and accordingly, several parameterizations of GWD induced by cumulus convection have been developed (e.g., *Rind et al.*, 1988; *Kershaw*, 1995; *Chun and Baik*, 1998, 2002; *Beres et al.*, 2004; *Song and Chun*, 2005). This, however, enhances the number of free parameters quantifying the influence of different sources. Understanding the dynamical contribution of gravity waves from a specific source is essential for including physical source paramterizations into general circulation models (GCMs) in a reliable way. This motivates the first science question of this thesis:

What are the contributions of convective gravity waves to the atmospheric dynamics?

One of the difficulties in studying contributions to atmospheric dynamics from convective gravity waves is the not well-known convective gravity wave spectrum. Depending on the horizontal wavelength and vertical wavelength, these waves interact differently with the atmospheric background and hence contribute differently to the dynamics. However, convective gravity waves have a very broad spectrum and each type of current observation techniques can cover only a certain part of this broad spectrum. This makes the scales of convective gravity waves an open issue. This open issue motivates the following question:

What are the scales of gravity waves above convection?

The scales of gravity waves influence their behavior in different physical processes. For example, saturation of gravity waves is strongly related to horizontal and vertical scales of the waves and the saturation can hardly be represented without correctly defining the gravity wave scales. With the same amplitude, shorter horizontal wavelength waves carry higher momentum flux. Therefore, an inadequate representation of wave scale in models can contribute to the difference of vertical gradient between modeled GWMF and observed GWMF as shown in *Geller et al.* (2013). Furthermore, poleward propagation of gravity waves also depends significantly on horizontal scale of the waves: the longer horizontal scale,

the stronger poleward propagation is found. Parameterizations of GWD induced by cumulus convection mentioned above are used in the GCMs, where the column base assumption is applied and gravity waves are allowed to propagate only vertically in the column where they are excited. Therefore, the impact of horizontal scale on poleward propagation in those parameterizations cannot be properly represented, although this impact is known to be significant (e.g. *Kalisch et al.*, 2014).

Observations provide evidence that different scales of convective gravity waves exist. These scales can be of a few kilometers (*Jewtoukoff et al.*, 2013), a few tens kilometers (e.g. *Taylor et al.*, 1987; *Dewan et al.*, 1998), several hundreds kilometers (e.g. *Pfister et al.*, 1993a) to several thousands kilometers (e.g. *Preusse*, 2001). More observational studies of convective gravity waves are described in chapter 3. To deal with the scale issue, previous model studies often determined the scales by first using educated guesses and then validated these scales via spatial distribution (e.g. *Choi et al.*, 2009, 2012). Until recently, the statistics of convective gravity wave scales have been provided only by limb sounder observations (*Ern and Preusse*, 2012). Determining the scales of convective gravity waves based on these limb sounder observations can provide significant insights to reveal the open issue of scales above convection. However, this method of determination has not been applied until recently. The reason is that the scales observed by limb sounders are influenced strongly by the complex observation geometry as well as instrument visibility, and these influences have not been carefully investigated. Therefore, in order to properly employ the useful observations from limb sounders, the following question need to be carefully considered:

How are the observed gravity wave scales influenced by observation geometry and visibility effects?

Until recently, the influence of visibility and retrieval on gravity waves observed by limb sounders has been preliminarily studied by *Preusse et al.* (2002) and *Ern et al.* (2005). However, a study considering both visibility effects and the complex observation geometry has not been investigated. Such a comprehensive study is performed in the current thesis.

In this thesis, these above-mentioned questions are addressed by combining simulations and limb sounder observations. For simulations, convective gravity waves are generated using the Yonsei convective gravity wave source scheme. The propagation of these waves is calculated using ray tracing method. For comparing simulated results with observations, a comprehensive observational filter that mimics the instrument limitations is developed and applied to the simulated waves. Gravity wave momentum flux spectra in terms of horizontal and vertical wave numbers are calculated from simulations and compared with the respective observed spectrum. Based on this comparison, the scales of convective gravity waves above convection are determined. In order to analyze the contributions of convective gravity waves to the atmospheric dynamics, the zonal momentum balance is considered in vertical cross sections of GWMF as well as in vertical cross sections of vertical gradients of GWMF. Furthermore, global maps of the horizontal distribution of GWMF are considered. Also, the latitude dependence

of the zonal phase speed spectrum of GWMF is shown. The study conducted in this thesis is unique in two aspects: (1) the complexity and comprehensiveness of the observational filter, and (2) the fact that the model spectral distribution is determined merely from observed spectral distributions.

In this dissertation, chapter 2 briefly introduces gravity wave theory. The Yonsei convective gravity wave source scheme is described in chapter 3. Chapter 4 presents the ray-tracing method to calculate trajectories and wave characteristics along trajectories of gravity waves. The comprehensive observational filter for satellite limb sounding of gravity waves is addressed in chapter 5. In chapter 6, a systematic survey of the Yonsei convective gravity wave sources scheme is performed using observations from the High Resolution Dynamics Limb Sounder (HIRDLS). Relative contribution of gravity waves seen by HIRDLS to the atmospheric dynamics is also discussed in chapter 6. Finally, a summary and outlook is given in chapter 7.

Chapter 2

Background of gravity waves

In this chapter, the generation mechanism of gravity waves as well as important formulas are introduced. These topics are describe in more detailed in *Fritts and Alexander* (2003) and only a brief overview is presented in this chapter.

2.1 Generation mechanism

To understand the fundamental mechanism of a gravity wave, we consider an air parcel in the troposphere, which is displaced adiabatically to a higher altitude level. As the air parcel is lifted up to a higher altitude, its temperature decreases. Following the law for ideal gas, the density of this air parcel increases. Therefore, at this higher altitude level, the gravity force becomes stronger than the buoyancy and the resulting force points downward. The air parcel hence moves downward under the impact of the resulting force. At the rest position, due to the inertia, the air parcel continues moving downward to a lower altitude level. At this lower altitude level, the opposite process occurs: the temperature of the air parcel increases and its density decreases. Consequently, the buoyancy is stronger than the gravity force and resulting force moves the air parcel upwards. This oscillation repeats and thus forms gravity waves.

The displacement process of the air parcel can be described as a harmonic oscillation by the following equation:

$$\frac{d^2z}{dt^2} = -N^2 z \tag{2.1}$$

where z is the coordinate in the vertical direction, t is time, and N is the buoyancy frequency or the Brunt-Väisälä frequency. Calculating the acceleration we obtain:

$$N = \sqrt{\frac{g}{T}\left(\frac{\partial T}{\partial z} - \Gamma\right)} \tag{2.2}$$

where g is the gravitational acceleration, T is the absolute temperature, and Γ is the adiabatic lapse rate. For dry air $\Gamma \approx -10$ K/ km.

The buoyancy frequency N can also be written in terms of potential temperature as follows:

$$N = \sqrt{\frac{g}{\theta}\frac{\partial \theta}{\partial z}} \tag{2.3}$$

where θ is the potential temperature. The potential temperature of an air parcel at pressure p is the temperature that the parcel would acquire if it is adiabatically brought to a standard reference pressure p_0. The potential temperature θ is defined as follows:

$$\theta = T\left(\frac{p_0}{p}\right)^{\frac{R}{c_p}} \tag{2.4}$$

where p_0 is the standard reference pressure (usually 1000 millibars), p is the pressure at the considered altitude level, R is the gas constant of air, and c_p is the specific heat capacity at a constant pressure.

2.2 Important formulas

In this section, essential formulas such as fundamental fluid equations, dispersion relation, polarization relations and other relevant formulas are introduced:

The fundamental fluid equations

To study gravity waves, the fundamental fluid equations, which was first formulated by *Holton* (1982) based on conservation of momentum, mass, and energy, are widely employed:

$$\begin{aligned}
\frac{du}{dt} - fv + \frac{1}{\rho}\frac{\partial p}{\partial x} &= X \\
\frac{dv}{dt} + fu + \frac{1}{\rho}\frac{\partial p}{\partial y} &= Y \\
\frac{dw}{dt} + \frac{1}{\rho}\frac{\partial p}{\partial z} + g &= 0 \\
\frac{1}{\rho}\frac{dp}{dt} + \frac{\partial u}{\partial x} + \frac{\partial v}{\partial y} + \frac{\partial w}{\partial z} &= 0 \\
\frac{d\theta}{dt} &= Q
\end{aligned} \tag{2.5}$$

Here u, v, w are velocity components of the fluid in x, y, z directions of the Cartesian coordinate system, respectively. The air density is denoted by ρ, p is

the pressure, f is the Coriolis parameter and θ is the potential temperature. X, Y and Q are unspecific forcings, which can drive waves or affect wave dissipation.

Equations 2.5 describe the dynamics of a fluid in general. In order to study gravity waves, scale separation and linearization are usually applied to Equations 2.5. The scale separation is based on the assumption that each variable in Equations 2.5 is comprised of a background flow and the small perturbation due to gravity waves. The linearization neglects the second order of small perturbations. Equations 2.5 therefore can be used to describe the dynamics of the mean flow as well as dynamics of gravity waves. In the mean flow case, X, for example, is the wave drag component. In the gravity wave dynamics case, X is the turbulent and radiative damping. In the global content of this thesis, X, Y are the wave drag.

After scale separation and linearization, a wave ansatz is applied to the fundamental fluid equations for small perturbations due to gravity waves. Solving these equations leads to the dispersion relation.

The dispersion relation

The dispersion relation relates the intrinsic angular frequency of the wave to the wave vector as well as to the physical properties of the atmosphere:

$$\hat{\omega} = \frac{N^2(k^2 + l^2) + f^2\,(m^2 + \alpha^2)}{k^2 + l^2 + m^2 + \alpha^2} \tag{2.6}$$

where $\hat{\omega}$ is the intrinsic angular frequency of the wave, i.e. the frequency with which an observer moving together with the background flow would observe the wave, (k, l, m) are wave number components, and $\alpha = 1/2H$, where H is the density scale height. Here $f = 2\Omega \sin\phi$ is the Coriolis parameter, where Ω is the Earth rotation and ϕ is latitude. The derivation of the dispersion relation can be found in e.g. *Fritts and Alexander* (2003) or in any standard text book.

Calculation of gravity wave momentum flux

Gravity wave momentum flux can be calculated based on components of the wave-induced wind perturbation as follows:

$$(F_{Px}, F_{Py}) = \rho \left(1 - \frac{f^2}{\hat{\omega}^2}\right) (\overline{u'w'}, \overline{v'w'}) \tag{2.7}$$

where F_{Px} and F_{Py} are gravity wave momentum flux components in zonal and meridional directions and u', v', w' are the components of the wind perturbation vector. The bar above the products of the wind perturbations denotes the average over a wave period.

Many global studies on gravity waves are based on temperature measurements from satellites. In order to determine GWMF from such measurements, a formula to calculate gravity wave momentum flux from temperature data is helpful. Such a

formula was derived in *Ern et al.* (2004) by first replacing the wind perturbations in Equation 2.7 by potential temperature. This can be done using the polarization relations, which relate perturbation amplitudes of different variables describing wave characteristics and atmospheric properties:

$$\begin{aligned} u' &= \left(\frac{i\hat{\omega}k - fl}{i\hat{\omega}l + fk}\right) v' \\ p' &= \left(\frac{\hat{\omega}^2 - f^2}{\hat{\omega}k + ifl}\right) u' = \left(\frac{\hat{\omega}^2 - f^2}{\hat{\omega}l - ifk}\right) v' \\ w' &= \frac{\left(m - \frac{i}{2H}\right)\hat{\omega}}{N^2 - \hat{\omega}^2} p' \\ \theta' &= \frac{N^2}{i\hat{\omega}g} w' \end{aligned} \tag{2.8}$$

where p' and θ' are the perturbations of pressure and potential temperature. Taking into account the relation between temperature and potential temperature:

$$\frac{T'}{T} = \frac{\theta'}{\theta} \tag{2.9}$$

where θ and T denote the background potential temperature and background temperature, respectively, T' denotes the temperature perturbation due to gravity wave, Equation 2.7 can be rewritten using temperature data:

$$(F_{Px}, F_{Py}) = \frac{1}{2}\rho \frac{(k,l)}{m} \left(\frac{g}{N}\right)^2 \left(\frac{\hat{T}}{T}\right)^2 \tag{2.10}$$

where (k, l, m) is the wave number vector and $\hat{T}$ is the temperature perturbation amplitude. Absolute gravity wave momentum flux then can be determined as follows:

$$F_{Ph} = \sqrt{F_{Px}^2 + F_{Py}^2} = \frac{1}{2}\rho \frac{k_h}{m} \left(\frac{g}{N}\right)^2 \left(\frac{\hat{T}}{T}\right)^2 \tag{2.11}$$

where $k_h = \sqrt{k^2 + l^2}$ is the horizontal wave number.

Calculation of gravity wave drag

Gravity wave drag quantifies how gravity waves contribute to the forcing of various global circulations (cf. Equations 2.5) via wave breaking or dissipation.

Gravity wave drag is calculated based on the vertical gradient of the gravity wave momentum flux as follows:

$$X, Y = \frac{-1}{\rho} \frac{\partial}{\partial z} \left(F_{Px}, F_{Py} \right) \tag{2.12}$$

where X, Y are the zonal and meridional components of gravity wave drag, respectively.

Chapter 3

The Yonsei convective gravity wave source scheme

3.1 Convective gravity waves: observations and models

3.1.1 Observational evidences:

Convection has been recognized as one of the most dominant sources of gravity waves for decades. Although the inherent intermittency of convective gravity waves causes a major difficulty in observing them, numerous evidence of gravity waves in the stratosphere, which closely correspond to intense convection events in the troposphere, is found. Observations were performed using different kinds of measurement instruments, such as aircraft, radar, radiosonde, and satellite.

Observations from aircraft:

Pfister et al. (1986) analyzed temperature and ozone from aircraft measurements in the lower stratosphere and found large amplitude disturbances during a flight over an intense cumulus convective cell. On other days of the campaign, when no intense convection was found, the disturbance amplitudes were significantly weaker. *Alexander and Pfister* (1995) utilized winds measured by the Meteorological Measurement System on board the ER-2 aircraft to estimate the vertical flux of horizontal momentum above deep convection. Signatures of high-frequency waves are found in association with strong convection. In particular, an overshooting cloud turret was observed below the flight path. At the same location, analysis demonstrated a change in the direction of the observed momentum flux vector from northwest to southeast. In a similar work, *Alexander et al.* (2000) strengthened the close relationship between tropical stratospheric gravity waves and deep convection using wind measurements from NASA's ER-2 aircraft in the stratosphere and cloud brightness temperature, as an indicator for deep convec-

tion below the aircraft. Particularly, strong correlation between high gravity wave momentum flux and cold, high convective clouds were found during the campaign over northern Australia and Indonesia.

Observations from radars and air sounding:

By studying winds observed by MST (Mesosphere Stratosphere and Troposphere) radar during the passage of Typhoon Kelly, *Sato* (1993) found signatures of gravity waves in the lower stratosphere, which were likely generated by intense convection reaching up to the tropopause. Later on, *Sato et al.* (1995) analyzed vertical wind disturbances during midsummer afternoons using measurements from UHF/VHF radars and radiosondes. These wind disturbances are related to cumulus convection generated by solar heating. *Sato et al.* (1995) found that wind perturbations above 3 km are likely due to gravity waves forced by cumulus convection at lower altitude levels. Also, *Karoly et al.* (1996) estimated gravity wave activity based on upper-air sounding data collected at Santa Cruz in the western tropical Pacific Ocean. Their results showed that enhancement of gravity wave activity is associated with increased convection.

Observations from radiosondes:

Tsuda et al. (1994a) found significant signatures of gravity waves above 25 km altitude by analyzing radiosonde observations over East Java, Indonesia. Since the considered region is far away from topography and regions of baroclinic instability, sources of these gravity waves are likely related to deep convection, which usually appears in this region. Moreover, *Shimizu and Tsuda* (1997) analyzed profiles of wind velocity and temperature observed by radiosondes in West Java, Indonesia and found enhancement of gravity waves activity when high convective clouds passed over the considered location. These findings again indicate that cumulus convection is likely a source of gravity waves in the equatorial area. Later on, *Vincent and Alexander* (2000) studied variations of gravity waves at Cocos Islands, which are located in the area of constantly strong convection in the Indian Ocean. Analysis of radiosonde observations showed that largest wave amplitude are found in the wet season (between December and July), when the convection is strongest. Wave parameters derived in this work agree well with the ones shown by *Tsuda et al.* (1994a) and *Shimizu and Tsuda* (1997).

Observations from satellites:

In recent years, an increasing number of satellite observations allow to study global distributions of gravity waves. These observations also demonstrate the close correspondence between gravity waves and deep convection. For instance, evidence of gravity waves generated by convection is shown in MSX (Midcourse Space Experiment) satellite images (*Dewan et al.*, 1998). Wave patterns in the form of concentric circles are observed on a radiative surface at a constant altitude level above an isolated, convective thunderstorm. *Wu and Waters* (1996a) extracted gravity wave variances from saturated radiance measurements from MLS (Microwave Limb Sounder). Global maps of gravity wave variances showed a major maximum in the polar vortex in the winter hemisphere and another second maximum in the summer subtropics. In particular, high gravity waves variances

in the stratosphere are observed over Brazil, near Madagascar, and North Australia during January, and over Central America, North Africa, and South Asia during July. *Wu and Waters* (1996a) suggested that cumulus convection in the troposphere, which is frequently found over tropical and subtropical land masses, is most likely responsible for strong activity of gravity waves in these regions. Also using MLS observations, *McLandress et al.* (2000) demonstrated a clear correlation between MLS variances and satellite observations of outgoing-longwave radiation indicating that deep convection is likely the source for gravity waves in the summer subtropics. In another study, *Jiang et al.* (2004a) showed high correlation between major convection centers and gravity wave variances by analyzing observations from MLS.

Later on, *Ern et al.* (2004) for the first time derived gravity wave momentum flux from space using temperatures observed by CRISTA (Cryogenic Infrared Spectrometers and Telescopes for the Atmosphere). Global maps of gravity wave momentum flux derived by *Ern et al.* (2004) and global maps shown by *Wu and Waters* (1996a) share many common features, in particular, the second maximum in the summer subtropics, where cumulus convection is intense. A similar second maximum in the subtropics of the summer hemisphere was also found in global maps of gravity wave momentum flux derived by *Alexander et al.* (2008) and *Ern et al.* (2011). In *Alexander et al.* (2008) and *Ern et al.* (2011), temperature profiles observed by HIRDLS (HIgh Resolution Dynamics Limb Sounder) on board the Aura satellite were analyzed. HIRDLS has better vertical resolution than CRISTA and much better vertical resolution than MLS. HIRDLS therefore can observe a broader part of the gravity wave spectrum and provide more advanced global distributions. In a case study, *Grimsdell et al.* (2010) investigated an extreme intense rainfall on 12 January 2003 near Darwin, Australia utilizing observations from AIRS (Atmospheric Infrared Sounder). The analysis showed a clear link between observed convective gravity waves and the extreme event. Correlation studies of gravity waves and convection using satellite observations are presented in *Preusse and Ern* (2005) and *Jia et al.* (2014).

3.1.2 Convective gravity wave modeling:

In parallel with an increasing number of convective gravity wave observations, source models for these waves were developed. Generally, source models rely on a fundamental assumption that the thermal forcing inside the cumulus convection, which is associated with the latent heat release, can interact with other stable layers above and wind shear to generate gravity waves. This fundamental assumption is depicted in Fig. 3.1. The interaction mechanism, however, is not fully understood and three simplified mechanisms were suggested: (1) pure thermal forcing or "resonant forcing", (2) a "transient mountain" or an "obstacle" effect, and (3) a "mechanical oscillator" effect.

Pure thermal forcing or "resonant forcing" mechanism:

The pure thermal forcing mechanism is based on the assumption, that os-

cillating updrafts and downdrafts affect the interface between the unstable and stable layers. This leads to oscillating displacements of the isentropes at the base of the stable layer. These oscillating displacements, in turn, generate vertically propagating gravity waves. The process of wave generation depends on temporal and spatial scales of the interfacial surface movement (*Townsend*, 1966). In the absence of strong wind shear, theoretical studies by *Salby and Garcia* (1987) and *Garcia and Salby* (1987) showed that the major vertical wavelength of convective gravity waves generated by the thermal forcing is twice of the heating depth. At the tropopause, the buoyancy frequency increases by a factor of two. Therefore, the waves propagating across the tropopause to the stratosphere are refracted and the vertical wavelength of these waves in the stratosphere decreases by a factor of two. Accordingly, in the absence of wind shear, vertical wavelengths in the stratosphere are expected to take the value of the depth of the heating in the troposphere. This concept was examined later by *Alexander et al.* (1995) and *Piani et al.* (2000). Observational evidence of gravity waves generated by pure thermal forcing was presented in *McLandress et al.* (2000).

Figure 3.1 shows a general schematic diagram of how convective gravity waves are generated according to simplified suggested mechanisms. A part of Fig. 3.1 presented the pure thermal forcing or "resonant forcing" mechanism: the thermal Q generates gravity waves with the major vertical wavelength λ_z equaling twice of the heating depth.

"Obstacle" effect or "transient mountain":

In the concept of the "obstacle" effect, the upcurrents of cumulus clouds act as obstacles to the horizontal flow resulting in gravity waves (*Newton*, 1960). In particular, when a stable layer moves relatively to cumulus clouds, the shape of the isentropes at the bottom of this layer is changed. This mechanism is similar to generation of orographic gravity waves when the air flows over a mountain. The role of the cumulus clouds is analogous to the role of the mountains in case of terrain-generated gravity waves. Therefore, this mechanism is also referred to as "transient mountain" mechanism. In Fig. 3.1, isentropes at the bottom of a stable layer moving relatively to the cumulus cloud is demonstrated by red solid lines. Oscillating displacements of these isentropes excite vertically propagating gravity waves. For this excitation mechanism, the ground-based phase speed of the generated waves is equal to the ground-based speed of the cumulus cloud.

Clark et al. (1986) performed a two-dimensional simulation to study the excitation mechanism of internal gravity waves above active thermal convection by considering both pure thermal forcing and "obstacle" effect mechanisms. The results showed that gravity waves can be excited by a combination of pure thermal forcing and the "obstacle" effect. In particular, the wave amplitude is much stronger in the presence of a strong wind shear at low-level altitudes, when the "obstacle" effect plays important role. With those findings, *Clark et al.* (1986) suggested that the "obstacle" effect is more effective in exciting gravity waves than the pure thermal forcing. Numerical simulation of *Clark et al.* (1986) showed a good agreement with aircraft observations on 12 June 1984 over Nebraska. Later on,

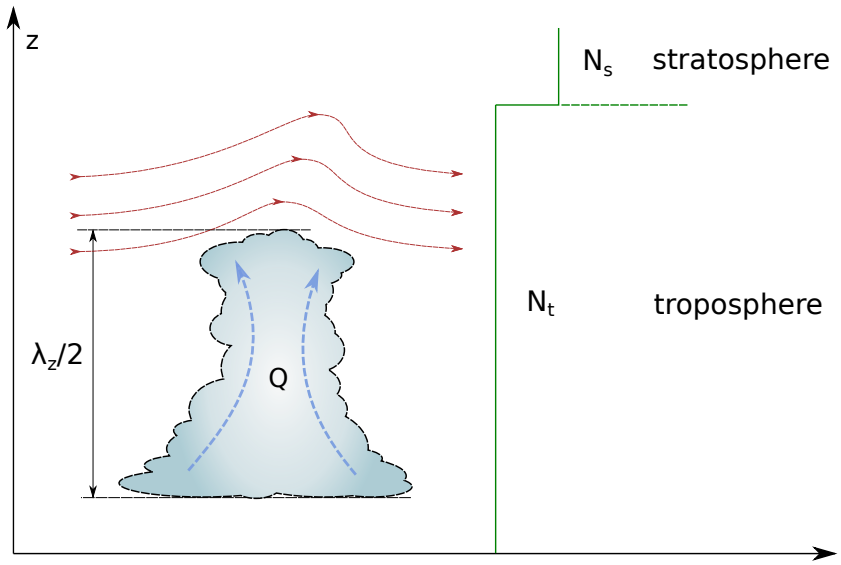

Figure 3.1: General schematic diagram of gravity waves generation by convection. The major vertical wavelength (λ_z) of gravity waves generated by pure thermal forcing is twice of the heating depth. Red lines indicate the isentropes at the bottom of a stable layer moving relatively to the cumulus cloud. Oscillating displacements of these isentropes excite vertically propagating gravity waves.

based on this mechanism, a linear model was built and validated against aircraft observations over deep convection during the NASA's 1980 Panama and 1987 Stratosphere-Troposphere Exchange Project (STEP)/ Australia Missions (*Pfister et al.*, 1993a,b). This mechanism favours generation of gravity waves propagating opposite to the background wind relative to the "transient mountain". In addition, this mechanism provides an anisotropic wave spectrum.

Mechanical oscillator:

Fovell et al. (1992) used a high-resolution two-dimensional numerical simulation to study characteristics of gravity waves generated by deep convection in storm squall lines. Different mean flow conditions relative to the storm were examined. *Fovell et al.* (1992) found that significant convective gravity waves can be excited even with very weak flow relative to the storm. Thus, they concluded that the "obstacle" effect plays only a minor role in generating gravity waves. In this case, it is suggested that gravity waves are mainly excited by the thermal forcing. *Fovell et al.* (1992) referred to this mechanism in his work as "mechanical oscillator effect" because the convective drafts, which formed periodically at the front edge of the squall line at low altitudes, moving rearward and reaching up to the tropopause, act similarly as a mechanical oscillator. The highest frequency of the generated gravity waves equals to the oscillation frequency and is about half of the tropospheric buoyancy frequency. Based on a similar mechanism, *Lane et al.* (2001) simulated tropical convective gravity waves in a three-dimensional numerical model with some additional constraints. Similar to the "obstacle" effect, the wave spectrum in case of mechanical oscillator becomes also anisotropic due to

background wind shear.

More details about these three generation mechanisms can be found in *Fritts and Alexander* (2003) and references therein. In general, convective gravity waves can be excited by a combination of different excitation mechanisms. The relative important of each mechanism may depend on the local shear, vertical configuration and time dependence of the latent heating.

Convective gravity wave parameterizations for large-scale models:

Since convectively generated gravity waves significantly impact the large-scale circulations, efforts have been made in order to include the effects of these waves into large-scale numerical models. For instance, *Rind et al.* (1988) formulated convectively forced gravity wave momentum flux based on the assumption that the gravity wave momentum flux and the vertically integrated convective mass flux are proportional. For a given convective mass flux, the momentum flux is assumed to be proportional to the buoyancy frequency at the top of the convection. In another work, *Kershaw* (1995) parameterized momentum flux due to convectively generated gravity waves by utilizing a linear, monochromatic gravity wave theory. *Kershaw* (1995) found a direct, linear dependency between the momentum flux at cloud top and the wind shear near the cloud top. A linear dependency was also found between the momentum flux and the convective intensity. Moreover, in this theory the momentum flux is inversely proportional to the buoyancy frequency above the convection. Later on, *Beres et al.* (2004) derived the momentum flux spectrum of convectively triggered gravity waves which can be implemented into the general circulation models using a linear formulation. The formulation is based on the properties of the multifrequency thermal forcing as well as wind conditions in the convective region. Gravity waves forced by steady component as well as oscillatory component of the thermal forcing are taken into account. *Beres et al.* (2004) showed that horizontal and vertical scales of the thermal forcing, the heating rate, and the tropospheric background wind are necessary to determine the spectrum of convective gravity waves at the source level. The paramterization of *Beres et al.* (2004), however, is simplified by considering the thermal forcing in a uniform vertical background wind as well as uniform stability. The Yonsei convective gravity wave source scheme (*Song and Chun*, 2005) was designed with the same purpose of integration into general circulation models. In difference from *Beres et al.* (2004), the Yonsei source scheme is based on a thermal forcing in a three-layer atmosphere with a constant wind shear at lower altitudes, a constant wind above that shear level, as well as a piece-wise constant stability altering at the cloud top. Details about history and development as well as brief mathematical description of the Yonsei convective gravity wave source scheme will be shown below in Section 3.2.

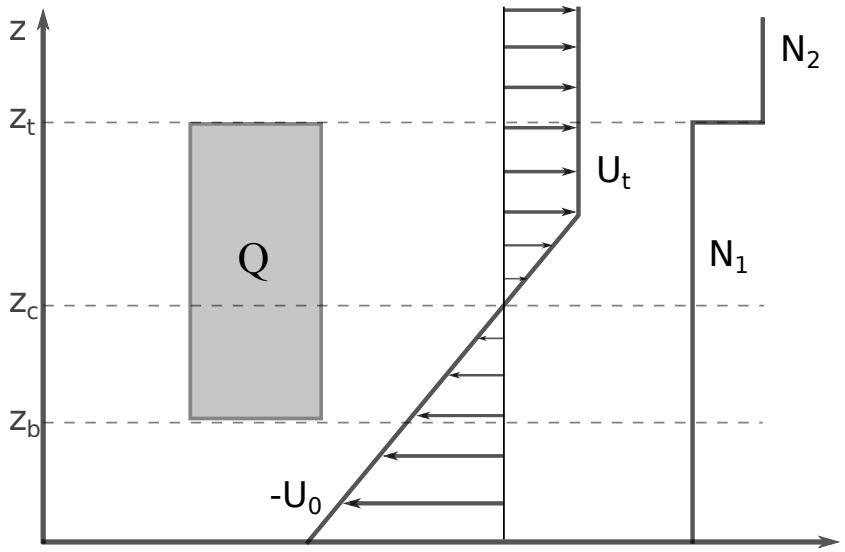

Figure 3.2: Schematic diagram of *Chun and Baik* (2002)' parameterization. Top height, bottom height of the diabatic forcing and the critical level are denoted by z_t, z_b, and z_c, respectively. U_0 and U_t are background winds at the surface and at the forcing top, respectively. Also, N_1 and N_2 denote the buoyancy frequencies below the forcing top and above the forcing top, respectively. For details see text.

3.2 The Yonsei convective gravity wave source scheme

3.2.1 History and development

The Yonsei convective gravity wave source scheme (*Song and Chun*, 2005) was developed based on the parameterization for convective gravity wave momentum flux generated by thermal forcing, which represents the latent heat due to cumulus convection (*Chun and Baik*, 1998). In the initial parameterization, *Chun and Baik* (1998) considered a forcing in a vertically uniform atmosphere, where the background wind as well as stability of the atmosphere are constant with height. By calculating linear, two-dimensional perturbations induced by diabatic heating, the vertical flux of the integrated horizontal momentum flux and its vertical derivative were determined. This parameterization was designed to include the effects of subgrid-scale gravity wave momentum flux above the cloud-top height into large-scale models. The parameterization of *Chun and Baik* (1998) was applied afterwards and considerably improved the reality of zonal wind and temperature in the southern hemisphere wintertime in the Yonsei University atmospheric general circulation model (*Chun et al.*, 2001) and in the tropics in the National Center for Atmospheric Research Community Climate Model (*Chun et al.*, 2004). Later on, this parameterization was updated and included into large-scale models by *Chun and Baik* (2002). Updates of the model were made by considering the diabatic forcing in a more realistic two-layer atmosphere having (1) constant wind shear from the ground to the cloud-top height with a critical level (where the wind

direction reverses) between cloud top and cloud bottom, and (2) a piece-wise constant buoyancy frequency below and above the cloud top. The parameterization of *Chun and Baik* (2002) is depicted in Fig. 3.2. The dynamical frame is relative to the diabatic forcing and gravity waves generated are stationary relative to the diabatic forcing. *Chun and Baik* (2002) found that the magnitude of momentum flux at cloud top is proportional to the square of the diabatic heating rate and inversely proportional to the background wind at cloud top. Also, this momentum flux magnitude depends on the stability above and below cloud-top height. Due to this dependency and the fact that the buoyancy frequency above cloud top is larger than the one below cloud top, under the same wind conditions for the same diabatic heating, the magnitude of gravity wave momentum flux in this updated paramterization is larger than the magnitude in the previous work of *Chun and Baik* (1998).

The parameterization of gravity wave drag induced by cumulus convection of *Chun and Baik* (2002) was further developed in *Song and Chun* (2005). The major development is taking into account not only stationary gravity waves (as modeled in *Chun and Baik*, 1998, 2002) but also non-stationary gravity waves relative to moving convective clouds. In this way, high-frequency gravity waves, which have been observed and simulated (as mentioned above in Section. 3.1), can be considered. Another change in *Song and Chun* (2005) is the three-layer structure of the atmosphere with (1) a linear wind shear from the ground to an altitude in between cloud top and cloud bottom without a critical level (above this shear level background wind is constant and continues being constant above the cloud top), and (2) a piece-wise constant buoyancy frequency below and above the cloud top. The gravity wave momentum flux at cloud top is calculated as a spectral combination of (1) a wave-filtering and resonance factor and (2) diabatic forcing. The two-dimensional formulation of the model was also extended to three-dimensional framework by allowing three-dimensionality of the diabatic forcing and different wave horizontal propagation directions. A brief mathematical description of this analytical model is presented below in Section. 3.2.2.

3.2.2 The current version of the Yonsei model

The analytical model of *Song and Chun* (2005) considers a diabatic forcing in three-layer atmosphere. These three layers are defined by the structure of the background wind as well as by the structure of the buoyancy frequency, i.e. stability of the atmosphere. In the lowest layer of the considered atmosphere, the background wind increases linearly from a value of U_0 at the surface to a value of U_t at an altitude of z_s. This altitude z_s presents the shear level and is located in between bottom height z_b and top height z_t of the diabatic forcing. A schematic diagram of the diabatic forcing in the three layer atmosphere is depicted in Fig. 3.3 The diabatic forcing Q represents the latent heat released by a cumulus cloud and can be described as:

$$Q = q(x,t)\zeta_q(z) \tag{3.1}$$

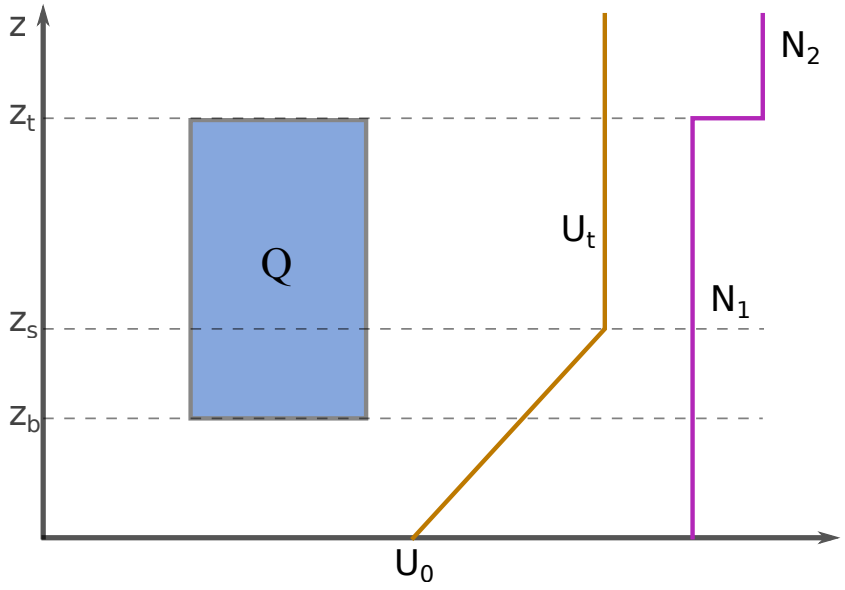

Figure 3.3: Schematic diagram of the diabatic forcing Q in the three layer atmosphere. Top height, bottom height of the diabatic forcing and the shear level are denoted by z_t, z_b, and z_s, respectively. U_0 and U_t are background winds at the surface and above the shear level, respectively. Also, N_1 and N_2 denote the buoyancy frequencies below the forcing top and above the forcing top, respectively. For details see text.

where $q(x,t)$ is the horizontal and temporal structure of Q and $\zeta_q(z)$ represents the vertical structure of Q. To formulate the convective GW source, governing equations for small-amplitude perturbation induced by Q in the two dimensional framework are first combined into a single equation for the vertical wind perturbation. Afterward, a double Fourier transform in space and time is applied to this single equation, which leads to the Taylor-Goldstein equation for convective gravity waves:

$$\frac{\partial^2 \hat{w}}{\partial z^2} + \left[\frac{N^2}{(U-c)^2} - \frac{d^2U/dz^2}{(U-c)} \right] \hat{w} = \frac{g\hat{q}\zeta_q}{c_p T_0 (U-c)^2} \tag{3.2}$$

Here $\hat{w}$ and $\hat{q}$ are the Fourier transforms of vertical wind perturbation and $q(x,t)$, respectively, c is the horizontal ground-based phase speed ($c = \omega/k$, where ω is the ground-based frequency and k is the horizontal wave number), c_p is the specific heat of air at constant pressure, T_0 is the reference temperature (temperature at the surface), U is the background wind and N is the Brunt-Väisälä frequency. Solving Equation 3.2 and using polarization relations produce Fourier transforms of horizontal and vertical wind perturbations $\hat{u}$ and $\hat{w}$.

Using $\hat{u}$ and $\hat{w}$ and Parseval's relation (*Arfken and Weber*, 1995), the space- and time-averaged momentum flux $\overline{M}$ generated by the diabatic forcing can be

calculated as follows:

$$\overline{M} = \frac{2(2\pi)^2}{L_x L_t} \int_{-\infty}^{\infty} \int_{0}^{\infty} \rho_0 \,\mathrm{Re}(\hat{u}\hat{w}^*) dk d\omega \tag{3.3}$$

where L_x and L_t are appropriate spatial and temporal scales, respectively, representing the period and area corresponding to the average momentum flux. This momentum flux is not always due to gravity waves. For $z < z_t$, this momentum flux is mainly due to the diabatic forcing itself. Therefore, momentum flux due to gravity waves is calculated from the cloud top and can be presented as a function of horizontal phase speed:

$$\overline{M}(c) = -\,\mathrm{sgn}(U_t - c)\rho_0 \frac{2(2\pi)^2}{L_x L_t} \left(\frac{g}{c_p T_0 N_1^2}\right)^2 \frac{N_2}{|U_t - c|} |X|^2 \Theta(c) \tag{3.4}$$

Here ρ_0 is the air density, $|X|$ is a function of ground-based phase speed c, the vertical configuration (ζ_q, z_b, z_t), background winds U_0, U_b, U_t, vertical wind shear α below z_s as well as stabilities N_1 and N_2. Details about X can be found in *Song and Chun* (2005). $|X|^2$ represents the resonance between vertical harmonics of natural wave modes and the diabatic forcing. $|X|^2$ also represents gravity wave filtering by the vertical propagation condition. Therefore, $|X|^2$ is referred to as the *wave-filtering and resonance factor*. $\Theta(c)$ is the diabatic source function, which is described by the following formula:

$$\Theta(c) = \frac{2q_0^2}{\delta_x} \left(\frac{\delta_x \delta_t}{16\pi}\right)^2 \frac{\sqrt{\pi/2}}{\sqrt{1 + (c - c_q)^2/c_0^2}} \tag{3.5}$$

where q_0 is the maximum magnitude of the diabatic forcing, c_q presents the moving speed of the forcing, and $c_0 = \delta_x/\delta_t$, where δ_x and δ_t are spatial and temporal scales of the forcing, respectively. δ_x and δ_t are free tunable parameters of this CGW source scheme. In chapter 6 of this thesis, reasonable ranges of these free parameters will be investigated by comparison with observations from HIRDLS.

Chapter 4

Gravity wave ray-tracing

4.1 Introduction

Ray tracing is a method for calculating the path of waves or particles through a system. This method is widely applied in numerous fields of research, such as radio signals, ocean acoustics, optical design, seismology, or plasma physics. The major difficulty of calculating wave paths in a medium is that the characteristics of the medium vary in both space and time. For example, the index of refraction in different regions of the medium may not be the same. Changes in characteristics of the medium result in changes of the wave velocity as well as wave propagation direction. In certain circumstances, this can also lead to reflection of waves from a surface. To solve this problem, the ray tracing method considers narrow beams called rays and repeatedly analyzes the propagation of wave packets along these rays through the medium in many discrete small steps. During each small step, the characteristics of the medium is considered to be constant, leading to a straight propagation of the wave. From a mathematical point of view, ray tracing will lead to solving partial differential equations.

In this section, ray tracing of gravity waves in the atmosphere is considered. A brief mathematical background of gravity wave ray tracing is presented. Furthermore, the Gravity wave Regional Or Global RAy Tracer (GROGRAT) *Marks and Eckermann* (1995); *Eckermann and Marks* (1997) is briefly introduced.

4.2 Mathematical background of gravity wave ray tracing

To derive the gravity wave ray tracing equations, we consider the linearized form of the fundamental fluid equations 2.5. By assuming that the basic state is horizontally uniform and the potential temperature $\bar{\theta}$, pressure $\bar{p}$, and density $\bar{\rho}$ change only in the vertical direction, we can obtain the dispersion relation 2.6. Using this

dispersion relation, the wave group velocity, which is the moving speed of the wave packet, can be calculated as follows:

$$\begin{aligned} c_{gx} &= \frac{\partial \omega}{\partial k} = \bar{u} + \frac{k(N^2 - \hat{\omega}^2)}{\hat{\omega}\Delta} \\ c_{gy} &= \frac{\partial \omega}{\partial l} = \bar{v} + \frac{l(N^2 - \hat{\omega}^2)}{\hat{\omega}\Delta} \\ c_{gz} &= \frac{\partial \omega}{\partial m} = -\frac{m(\hat{\omega}^2 - f^2)}{\hat{\omega}\Delta} \end{aligned} \tag{4.1}$$

where c_{gx}, c_{gy}, c_{gz} are components of the wave group velocity, k, l, m are wave number components, ω is the angular frequency, $\hat{\omega}$ is the intrinsic angular frequency, $\bar{u}$ and $\bar{v}$ are the background wind in zonal and meridional directions, $\Delta = k^2 + l^2 + m^2 + 1/4H^2$, H is the scale height, and f is the Coriolis parameter.

Following *Lighthill* (1967), the position and wave numbers of a wave packet change according to these equations:

$$\frac{dx}{dt} = \frac{\partial \omega}{\partial k}, \qquad \frac{dy}{dt} = \frac{\partial \omega}{\partial l}, \qquad \frac{dz}{dt} = \frac{\partial \omega}{\partial m}, \tag{4.2}$$

$$\frac{dk}{dt} = -\frac{\partial \omega}{\partial x}, \qquad \frac{dl}{dt} = -\frac{\partial \omega}{\partial y}, \qquad \frac{dm}{dt} = -\frac{\partial \omega}{\partial z}, \tag{4.3}$$

Using Eq. 4.2 the trajectory of a single gravity wave packet can be defined as

$$\begin{aligned} \frac{dx}{dt} &= \bar{u} + \frac{k(N^2 - \hat{\omega}^2)}{\hat{\omega}\Delta} \\ \frac{dy}{dt} &= \bar{v} + \frac{l(N^2 - \hat{\omega}^2)}{\hat{\omega}\Delta} \\ \frac{dz}{dt} &= -\frac{m(\hat{\omega}^2 - f^2)}{\hat{\omega}\Delta} \end{aligned} \tag{4.4}$$

The refraction of the wave vector can be calculated using Eq. 4.3 as follows:

$$\frac{dk}{dt} = -\frac{\partial\omega}{\partial x} = -k\frac{\partial\bar{u}}{\partial x} - l\frac{\partial\bar{v}}{\partial x} - \frac{1}{2\hat{\omega}\Delta}\left[\frac{\partial N^2}{\partial x}(k^2+l^2) - \frac{\partial\alpha^2}{\partial x}(\hat{\omega}^2 - f^2)\right]$$

$$\frac{dl}{dt} = -\frac{\partial\omega}{\partial y} = -k\frac{\partial\bar{u}}{\partial y} - l\frac{\partial\bar{v}}{\partial y} - \frac{1}{2\hat{\omega}\Delta}\left[\frac{\partial N^2}{\partial y}(k^2+l^2\ ) - \frac{\partial\alpha^2}{\partial y}(\hat{\omega}^2 - f^2)\right] \tag{4.5}$$

$$- f\frac{\partial f}{\partial y}(m^2+\alpha^2)$$

$$\frac{dm}{dt} = -\frac{\partial\omega}{\partial z} = -k\frac{\partial\bar{u}}{\partial z} - l\frac{\partial\bar{v}}{\partial z} - \frac{1}{2\hat{\omega}\Delta}\left[\frac{\partial N^2}{\partial z}(k^2+l^2) - \frac{\partial\alpha^2}{\partial z}(\hat{\omega}^2 - f^2)\right]$$

Equations 4.4 and 4.5 are known as gravity wave ray-tracing equations in the Cartesian coordinate system. They were originally formulated by *Lighthill* (1967). In the spherical coordinates, the evolution of wave number components is related not only to changes in the wave number vector but also to the spatial variation of the coordinate frame. Therefore, as shown by *Hasha et al.* (2008), equations describing the refraction of the wave vector for spherical coordinates contain additional terms. If wave number vector is denoted by $\vec{k}$ and:

$$\vec{k} = k\hat{\lambda} + l\hat{\theta} + m\hat{r}$$

where $\hat{\lambda}$, $\hat{\theta}$, $\hat{r}$ are zonal, meridional and radial unit vectors then:

$$\frac{d\lambda}{dt} = \frac{1}{rcos\theta}\left[\bar{u} + \frac{k(N^2-\hat{\omega}^2)}{\hat{\omega}\Delta}\right]$$

$$\frac{d\theta}{dt} = \frac{1}{r}\left[\bar{v} + \frac{l(N^2-\hat{\omega}^2)}{\hat{\omega}\Delta}\right] \tag{4.6}$$

$$\frac{dr}{dt} = -\frac{m(\hat{\omega}^2 - f^2)}{\hat{\omega}\Delta}$$

The refraction of the wave vector in spherical coordinate system can be rewrit-

ten as follows:

$$\begin{aligned}
\frac{dk}{dt} = & -\frac{k}{r\cos\theta}\frac{\partial\bar{u}}{\partial\lambda} - \frac{l}{r\cos\theta}\frac{\partial\bar{v}}{\partial\lambda} - \frac{1}{2\hat{\omega}\Delta}\left[\frac{(k^2+l^2)}{r\cos\theta}\frac{\partial N^2}{\partial\lambda} - \frac{(\hat{\omega}^2-f^2)}{r\cos\theta}\frac{\partial\alpha^2}{\partial\lambda}\right] \\
& - \frac{k}{r}\frac{dr}{dt} + k\tan\theta\frac{d\theta}{dt} \\
\frac{dl}{dt} = & -\frac{k}{r}\frac{\partial\bar{u}}{\partial\theta} - \frac{l}{r}\frac{\partial\bar{v}}{\partial\theta} - \frac{1}{2\hat{\omega}\Delta}\left[\frac{(k^2+l^2)}{r}\frac{\partial N^2}{\partial\theta} - \frac{(\hat{\omega}^2-f^2)}{r}\frac{\partial\alpha^2}{\partial\theta}\right. \\
& \left. - \frac{m^2+\alpha^2}{r}\frac{\partial f^2}{\partial\theta}\right] - \frac{l}{r}\frac{dr}{dt} - k\sin\theta\frac{d\lambda}{dt} \\
\frac{dm}{dt} = & -k\frac{\partial\bar{u}}{\partial r} - l\frac{\partial\bar{v}}{\partial r} - \frac{1}{2\hat{\omega}\Delta}\left[(k^2+l^2)\frac{\partial N^2}{\partial r} - (\hat{\omega}^2-f^2)\ \frac{\partial\alpha^2}{\partial r}\right] \\
& + k\cos\theta\frac{d\lambda}{dt} + l\frac{d\theta}{dt}
\end{aligned} \tag{4.7}$$

These equations can be rewritten in a more general form, which can describe ray-tracing process in both Cartesian and spherical coordinates:

$$\begin{aligned}
\dot{\vec{x}} &= \vec{\bar{U}} + \overrightarrow{\nabla}_{\vec{k}}\omega \\
\dot{\vec{k}} &= \overrightarrow{\nabla}(\vec{k}\cdot\vec{\omega} - \omega)
\end{aligned} \tag{4.8}$$

where $\vec{\bar{U}}$ represents the background flow, $\vec{x}$ is the coordinate vector, $\vec{k}$ is the wave number vector, and the dot $(\dot{})$ denotes the derivative with respect to time.

4.3 The GROGRAT ray-tracer

Based on the WKB-formalism, the Gravity wave Regional Or Global RAy Tracer (GROGRAT) was developed to describe the propagation and relevant processes of internal gravity waves in the atmosphere (*Marks and Eckermann*, 1995). In difference from earlier ray-tracing version of (*Dunkerton*, 1984), the GROGRAT model used for the first time the full gravity wave dispersion relation 2.6. This dispersion relation includes both non-hydrostatic gravity waves and the Coriolis force. With this improvement, gravity waves of all frequencies are accommodated in GROGRAT and the ray tracing can be performed in a rotating, compressible and stratified atmosphere. In general, if the temporal variation of the atmosphere is provided, GROGRAT is able to perform calculations with varying four-dimensional atmospheric background. However, GROGRAT is commonly used, including in this thesis, for three-dimensional gravity wave ray tracing.

For trajectory calculation, GROGRAT uses the ray-tracing equations, which were described in Section 4.2. The numerical integration is calculated by applying a Runge-Kutta solver. The refraction of the wave vector induced by vertical and horizontal gradients of the atmospheric backgrounds as well as meridional gradient of the Coriolis force are considered. Wave action flux is the conservative quantity along the wave trajectory in the absence of the wave dissipation. There is, however, continuous wave dissipation and damping along the trajectory and these effects are accounted for by using a realistic wave amplitude equation following the work of *Andrews et al.* (1987). In particular, amplitude damping caused by turbulence is calculated based on *Pitteway and Hines* (1963). Radiative damping due to the temperature difference between warm and cold phases of the wave is considered following *Zhu* (1994). The saturated amplitude of the wave is limited using saturation criteria of *Fritts and Rastogi* (1985).

Running of the GROGRAT model requires two input components: the launch distribution, and the atmospheric background. The launch distribution includes for each ray the following information: launch position (longitude, latitude, and altitude), wave amplitude, horizontal wave vector, and ground-based frequency of the wave. Note that the propagation direction is determined by the given components of the wave vector. These launch conditions represent gravity wave sources and can be taken from different types of gravity wave source schemes. In particular, in this thesis, the coupled model of the Yonsei convective source scheme (*Song and Chun*, 2005) and GROGRAT is used to calculate the global distribution of convective gravity waves in the stratosphere which can be compared to observations. This coupled model was first introduced in the work of *Kalisch* (2014).

The second input component of GROGRAT is the atmospheric background, which can be provided by different data sets. For this thesis, the three-hourly modern-era retrospective analysis for research and applications (MERRA) assimilated data were used. More detailed information about MERRA data as well as the convective parameterizations in the MERRA model can be found, for example, in *Rienecker et al.* (2011); *Kim and Alexander* (2013); *Wright and Fueglistaler* (2013).

An example of convective gravity wave ray tracing based on the coupled model is shown in Figure 4.1. The simulation is performed for 15th of July, 2006 at 00:00 GMT. The color code indicates the altitude of the rays. To focus on the source levels, the altitudes are limited in the range from 6 to 10 km. As we expected, convective gravity waves are generated mainly in the tropics and subtropics. Waves are also generated by stroms at mid and high latitudes. The wave trajectories in the storm regions closely follow the storm tracks.

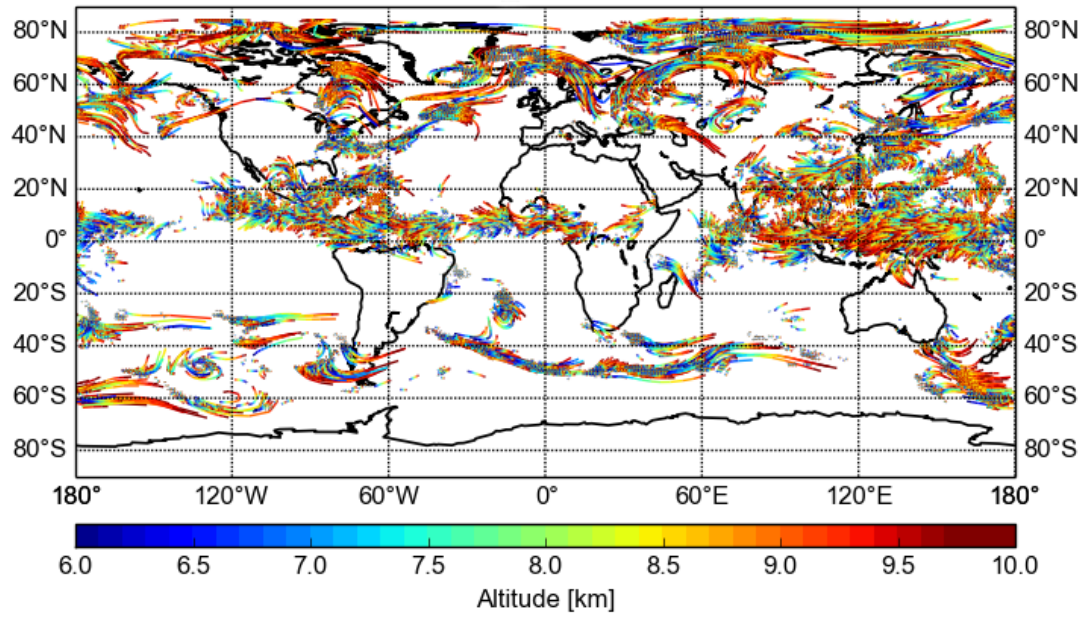

Figure 4.1: An example of convective gravity wave ray tracing. Convective gravity waves are generated using the Yonsei convective source scheme and then propagated using the GROGRAT ray tracer. The color code indicates the altitude of the rays. Altitude range in the current figure is limited only from 6 to 10 km in order to focus on the wave propagation near the source levels. As expected, many waves are generated in the tropics and subtropics. Waves are also generated by storms in the mid and high latitudes. The wave trajectories in the storm regions closely follow the storm tracks. For details see text.

Chapter 5

A comprehensive observational filter for infrared limb sounding of gravity waves

5.1 Introduction

In chapter 3, we described the Yonsei convective source scheme, which is used for generating convective gravity waves in our simulations. In chapter 4, we introduced the ray tracer (GROGRAT), which is used for propagating gravity waves to observation levels. For a meaningful comparison between simulations and observations, it is important to apply an observational filter on simulated results. In this chapter, a comprehensive observational filter for satellite limb sounding of gravity waves is developed.

In most general circulation models (GCMs), in particular those for climate runs, the effects of gravity waves are treated via parametrizations since gravity waves are small-scale processes and are not resolved in these GCMs. These parameterizations, however, use some simplifying assumptions and have a number of free tunable parameters (*Fritts and Alexander*, 2003). Observations are therefore important to validate these parameterizations. Several studies used observations to constrain and to improve gravity wave parameterizations (*Ern et al.*, 2006; *Preusse et al.*, 2009a; *Orr et al.*, 2010; *Choi et al.*, 2009, 2012; *Geller et al.*, 2013). These studies, however, are limited in using only absolutes values of gravity wave momentum flux (GWMF), which have quite large uncertainties (*Ern et al.*, 2004). In order to quantify these uncertainties and in order to capture the fact that a measured GWMF distribution, in general, may deviate from the true one in the atmosphere, the concept of the observational filter was introduced.

The importance of the observational filter was first pointed out by *Alexander* (1998). In her work for the MLS (microwave limb sounder), rocket sounding, and radiosonde measurements, the effects of the vertical resolution and of the analysis

method on the spatial distribution of gravity wave climatologies inferred from these instruments were estimated and the visibility of the waves was quantified as a function of the vertical wavelength. This function was applied to a spectrum calculated from a linear gravity wave model. The resulting global maps agreed well with global maps from MLS observations (*Wu and Waters*, 1996a). Good agreement was also found with rocket sounding data (*Eckermann et al.*, 1995) in terms of zonal mean gravity wave variance. Moreover, modeled results of *Alexander* (1998) showed reasonable agreement with radiosonde measurements (*Allen and Vincent*, 1995) in terms of the seasonal cycle of gravity wave energy density at midlatitudes.

Furthermore, significant differences in the morphology of gravity wave induced temperature variances between different limb-sounding instruments result from different observational filters. This was first hypothesized by *Alexander* (1998) and tested by *Preusse et al.* (2000) for four satellite instruments: Cryogenic Infrared Spectrometers and Telescopes for the Atmosphere (CRISTA), Global Positioning System/Meteorological Experiment (GPS/MET), Limb Infrared Monitor of the Stratosphere (LIMS) and MLS. *Preusse et al.* (2000) showed that all four instruments provide largely consistent information on zonal mean temperature variances in the middle atmosphere, if the observational filter of each instrument is approximated by a vertical visibility function, which is representative for the 300 to 800 km horizontal wavelength region. Good agreements when considering only one-dimensional filtering seem to imply that filtering of the horizontal wavelength is less important than filtering of the vertical wavelength.

As shown by *Alexander* (1998) and *Preusse et al.* (2000), global distributions of temperature variances may look very different depending on different observational filters. In particular, it was discussed whether all these measurements could be reliable when they exhibit large differences in the shape of the global distributions. The fact that applying the observational filter could explain these large differences among the various data sets emphasizes the importance of understanding the observational filter in a quantitative manner.

Another study which clearly shows the important effect of the observational filter is that of *Ern et al.* (2005), in which the wavelength filtering was applied to GWMF provided by the Warner and McIntyre model (*Warner and McIntyre*, 2001) and an aliasing correction was applied to the CRISTA data. They showed that the agreement between GWMF observed by CRISTA and respective model values at an altitude of 25 km improved significantly after vertical wavelength filtering was applied. In particular, in terms of horizontal structure, most of the features shown by CRISTA observations were reproduced. Horizontal wavelength filtering modified horizontal distributions only slightly. However, it reduced GWMF magnitude by a factor of more than 2.

In addition to infrared limb sounders, the impact of radiative transfer and retrieval was discussed also for other techniques. For instance, *Wu and Waters* (1997) showed the influence for MLS, *Gong et al.* (2012) considered the impact for AIRS (Atmospheric Infrared Sounder), *Lange and Jacobi* (2003) discussed GPS

occultation measurements. A more general overview of observational filters for different instruments can be found in *Preusse et al.* (2008) and *Alexander et al.* (2010).

In this thesis we analyze a comprehensive observational filter for infrared limb sounders, which for the first time takes into account instrument visibility as well as observation geometry with a high level of accuracy. We show how such a comprehensive filter considerably affects the gravity wave spectrum.

The developed observational filter is applied to a suitable model test case and the effects of the observational filter on the shape of the modeled GWMF spectrum with respect to horizontal and vertical wave numbers (wavelengths) are investigated. By spectral analysis, we demonstrate how various aspects of the observational filter affect gravity waves of different scales. For the test case, we use the combination of Yonsei CGWS scheme and GROGRAT described in chapters 3 and 4. The model generates a global distribution of individual waves, each fully characterized by location and a 3-D wave vector, thus forming a well-suited test case for our observational filter.

We start here by setting the free tunable parameters following previous studies. Parameter sets MF1 (δx = 5 km and δt = 20 min) and MF2 (δx = 25 km, δt = 60 min) were introduced by *Song and Chun* (2005) and *Choi et al.* (2012), respectively. We investigate in this work an additional spectrum MF3 (*Kalisch*, 2014) with a larger spatial scale (δx = 120 km and δt = 60 min).

From the generation mechanism, all discussed temporal and spatial scales (MF1, MF2 and MF3) are plausible. In the scope of this study, our aim is to quantitatively determine to which extent they are visible and to show how the different steps of the observational filter act on different wavelength scenarios and which steps are the most important ones. In particular, we will demonstrate how the observational filter affects both the magnitude and the shape of the spectral distribution.

In our efforts to understand the distribution measured by a certain instrument, we should keep in mind that our main aim is to determine the real world GWMF distribution. Previous studies (*Ern et al.*, 2006; *Orr et al.*, 2010; *Geller et al.*, 2013) primarily gave insight into the general shape of the global distribution. In particular, in *Geller et al.* (2013) substantial differences among models and measurements are found, which remain inconclusive, however: the error of GWMF is estimated to be a factor of ∼2-5 (*Ern et al.*, 2004), chiefly because of the observational filter effects described in the current work. From climate modeling studies, on the other hand, a knowledge of substantial better than a factor of two is requested (*Sigmond and Scinocca*, 2010). This means that there is a gap between what we need for climate studies and what we can provide by measurements. Application of the observational filter is one way out of this dilemma: We cannot reconstruct the true GWMF from the measurements more accurately, because there are too many unknowns in the true distribution. However, assuming we know the true distribution, we can calculate with much higher accuracy what we should observe, provided we have a sufficiently accurate description of the

observational filter.

What does that mean? Our aim is a GCM with realistic GWMF, either resolved or parameterized. If we are to compare the full modeled GWMF directly with the observations, we never can reach the required accuracy. If we apply the observational filter to the model first, we can reach the accuracy, provided a) the filter is sufficiently accurate and b), a sufficiently large part of the spectrum is visible. Even if we are only able to falsify, this allows to tell whether a model is inaccurate and hence we can initiate improvements. We still do not have the true distribution, but we can definitely rule out incorrect ones and the form of the discrepancy may give us guidance how improvement may be achieved.

This makes the comprehensive observational filter for IR limb sounders so important: IR limb sounders cover a relatively large part of the gravity wave spectrum (see condition b) and the observational filter needs to be comprehensive, because only a comprehensive filter will be accurate (see condition a).

Other types of satellite instruments have different observational filters. These techniques and whether they could be approached applying the methods described in this work, is described in Appendix B. The observational filter designed in this work describes the inevitable effects of the limb sounding technique and the modification of the spectral shape. It does not include errors either from the instrument (e.g. noise) nor potentially caused by the analysis method. The delineation from such effects is discussed in Appendix C.

5.2 Instruments and observation geometry

5.2.1 Limb-sounding technique

Infrared limb sounding from satellites is a well-established method for exploring the middle atmosphere (*Bailey and Gille*, 1986; *Gordley et al.*, 1994; *Marshall et al.*, 1994; *Riese et al.*, 1999; *Preusse et al.*, 2002). The basic geometry of limb sounding is depicted in Fig. 5.1. The instrument looks from its orbit towards the Earth's horizon, through the atmosphere and into cold space. Three exemplary lines of sight (LOS) are depicted in Fig. 5.1 by green dashed lines. The radiance measured by the instrument results from emission and reabsorption along the LOS. For optically thin emissions, reabsorption is weak and ∼50% of the measured signals comes from a 2 km-thick layer above the tangent points (purple dots), where the LOS is closest to the Earth's surface. For this case, radiative transfer can be described by a Gaussian weighting function (*Preusse et al.*, 2002, 2008) centered around the tangent point and, accordingly, measurements are associated with the tangent altitude (blue arrow) and the location of the tangent point. The precise viewing geometry varies for the individual instruments.

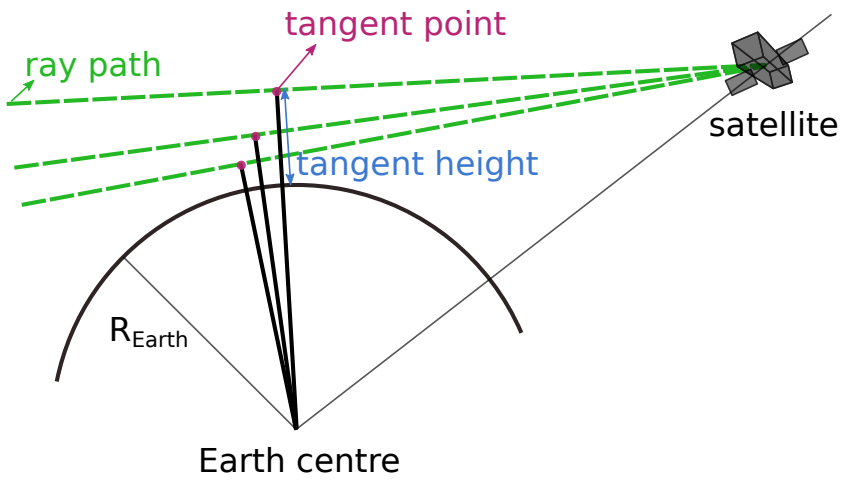

Figure 5.1: Measuring geometry of the limb-sounding technique.

5.2.2 SABER instrument

The SABER instrument uses broadband radiometers to detect limb radiance in the thermal infrared. Temperature is retrieved from the main CO_2 ν_2 emission at 15 µm (*Remsberg et al.*, 2008). SABER was launched on 7 December 2001 onboard the TIMED (Thermosphere Ionosphere Mesosphere Energetics Dynamics) satellite into an orbit at an altitude of 625 km and inclination of 74.1° and is still in operation. The angle between flight direction and LOS, called "view angle" below, is schematically shown in Fig. 5.2. It alternates between 90° for northward-looking mode and 270° for southward-looking mode in yaw maneuvers roughly every 60 days. In Fig. 5.2, the black arrow shows the flight direction, the green line (SABER-N) indicates the LOS of SABER in the northward-looking mode, while the red line (SABER-S) is the LOS in the southward-looking mode. The corresponding latitude coverage of northward- and southward-looking modes changes between 52° S to 83° N and 83° S to 52° N. More detailed information about the SABER instrument can be found, for instance, in *Mlynczak* (1997) and *Russell III et al.* (1999).

The orbital track and flight direction as well as satellite positions and corresponding tangent points for a typical southward-looking orbit of SABER are shown in Fig. 5.4a. Note that SABER views across the pole for the southern turning point. In Fig. 5.4a, green dots are the satellite positions, red triangles are the corresponding tangent points. Blue arrows along the satellite track show the flight direction, while the purple solid line indicates an example of a LOS. In addition, the latitude coverage during the year 2008 is shown in Fig. 5.3. Orange bands are coverages of the northward-looking mode, while blue bands indicate coverages of the southward-looking mode.

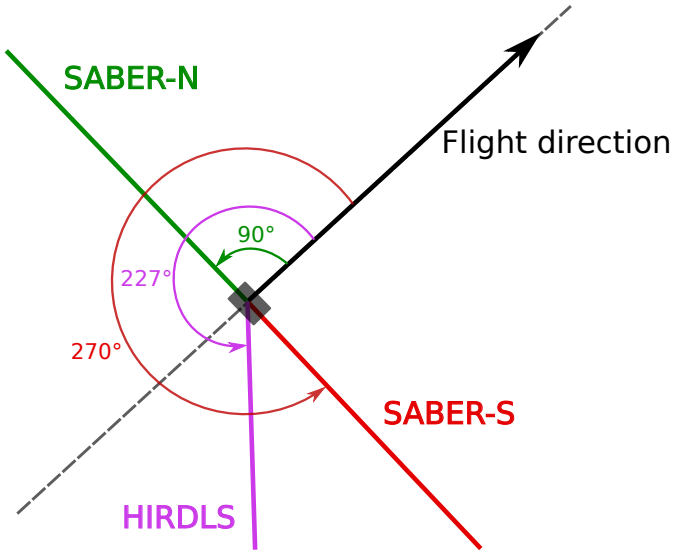

Figure 5.2: Satellite top-view of the SABER and HIRDLS viewing geometry, the black arrow shows the flight direction, green and red lines are the lines of sight (LOS) of SABER for northward- and southward-viewing modes, respectively. The purple line is the LOS of HIRDLS. For details see text.

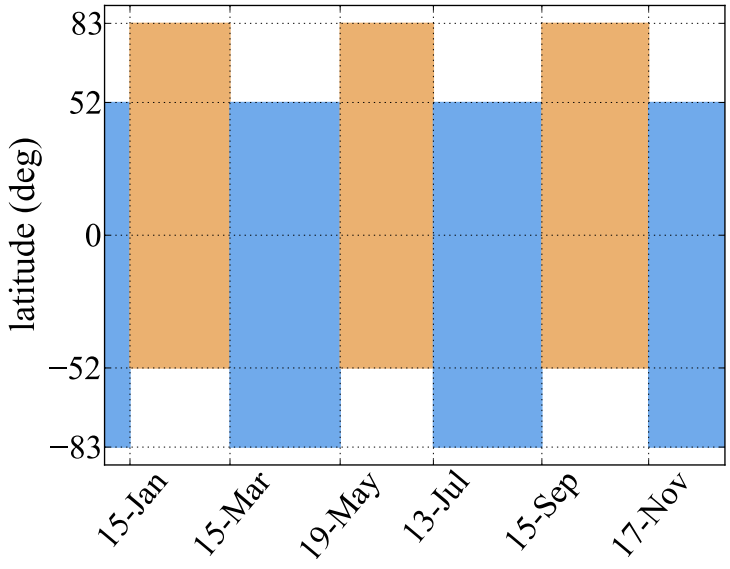

Figure 5.3: SABER latitude coverage during 2008; orange bands are coverages of northward viewing while blue bands show coverages of southward viewing. For details see text.

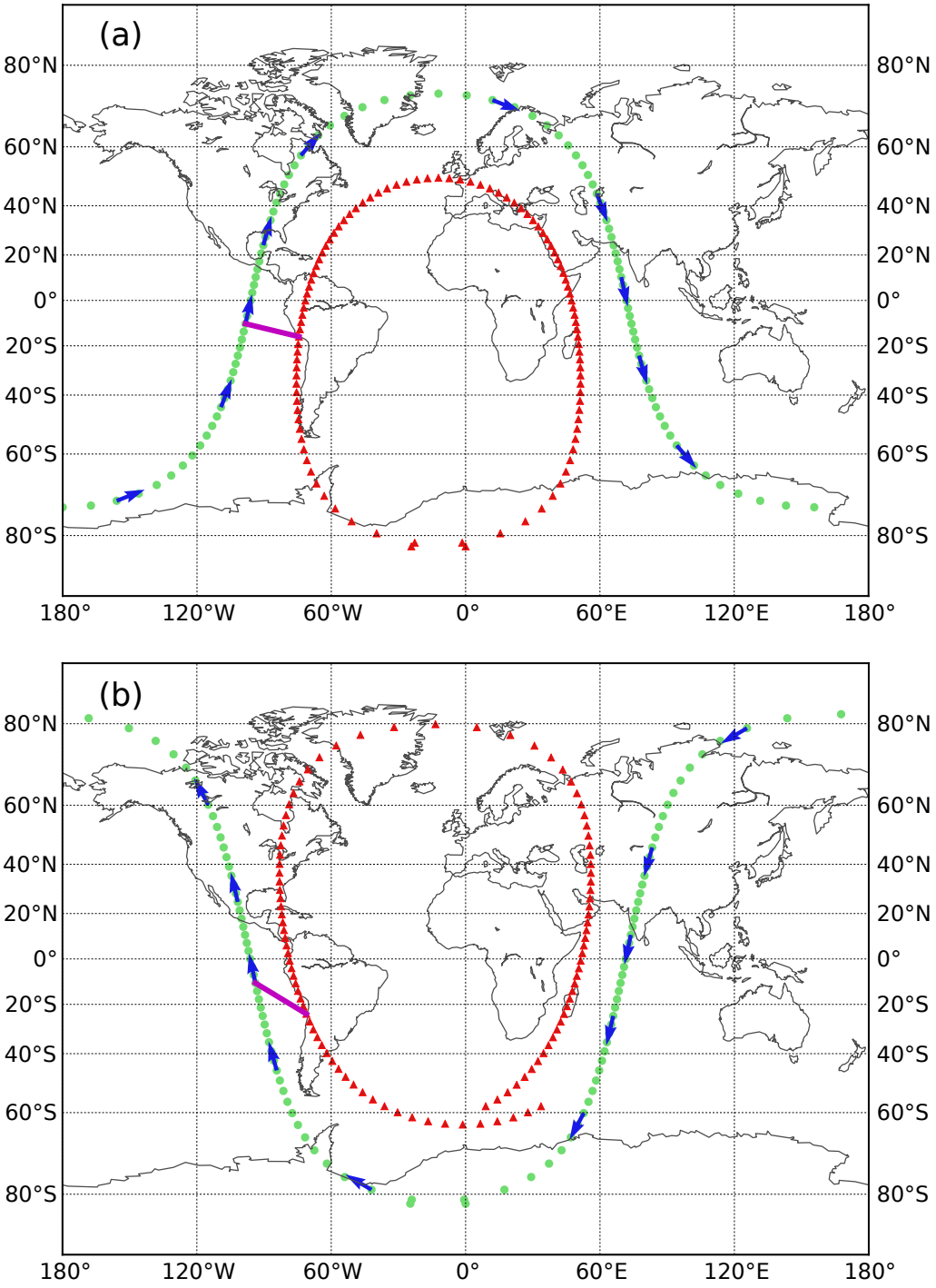

Figure 5.4: Global observation geometry of an exemplary orbit of **(a)** SABER (southward looking mode) and **(b)** HIRDLS. Satellite positions are shown by green dots and corresponding tangent points by red triangles. The thick purple line represents an exemplary LOS, while blue arrows show the flight direction. For details see text.

5.2.3 HIRDLS instrument

The HIRDLS instrument is an infrared radiometer onboard the Aura satellite, which also measures thermal emissions from the atmospheric limb. The orbit altitude and orbit inclination of Aura are 710 km and 98.2°, respectively. The HIRDLS instrument has a fixed view angle of $180 + 47 = 227°$, which leads to a latitude coverage from about 63° S to about 80° N. More detailed information about the HIRDLS instrument can be found, for instance, in *Gille et al.* (2003, 2008).

The view angle of HIRDLS is schematically depicted in Fig. 5.2 where the purple line illustrates the LOS of the HIRDLS instrument. In addition, satellite positions (green dots) and corresponding tangent points (red triangles) for an exemplary orbit are shown in Fig. 5.4b. HIRDLS's flight direction is indicated by blue arrows and the purple solid line shows an exemplary LOS.

5.2.4 Observation geometry in the local coordinate system

Our aim is to apply an observational filter to a simulated gravity wave at a specific location. So far, we have seen in Fig. 5.2 the viewing geometry of SABER and HIRDLS with respect to the satellite. Now, in order to apply the observational filter, we need to determine the observation geometry with respect to the same local geophysical coordinate system in which the wave vector of the simulated gravity wave is given. In Fig. 5.5, such an observation geometry is displayed for a short orbit segment. The instrument views in the direction of the LOS (blue solid arrows). The tangent points (blue crosses) are interpreted as the actual locations of the observations. The track of the tangent points, i.e. the track of the observations, is indicated by the green arrow. At one of the tangent points, a local coordinate system is shown (red axes). The angle between the LOS and the x direction of the local coordinate system is called β and the angle measured from the x direction to the tangent-point track is called γ. Dependences of the angles β and γ on latitude for the observation geometry of SABER and HIRDLS are shown in Appendix D.

5.3 Global gravity wave simulation

In order to demonstrate the application of the observational filter, a modeled gravity wave distribution is needed. Here, we use exemplarily ray-tracing simulations based on convective sources. Offline simulation of global gravity waves was performed by coupling the CGWS scheme (*Song and Chun*, 2005) and the gravity wave regional or global ray tracer (GROGRAT) (*Marks and Eckermann*, 1995; *Eckermann and Marks*, 1997). The CGWS scheme and GROGRAT are described in more detailed in chapter 3 and chapter 4, respectively.

In the CGWS scheme, calculation of the phase speed spectrum of GWMF requires the following quantities: maximum magnitude of the diabatic forcing

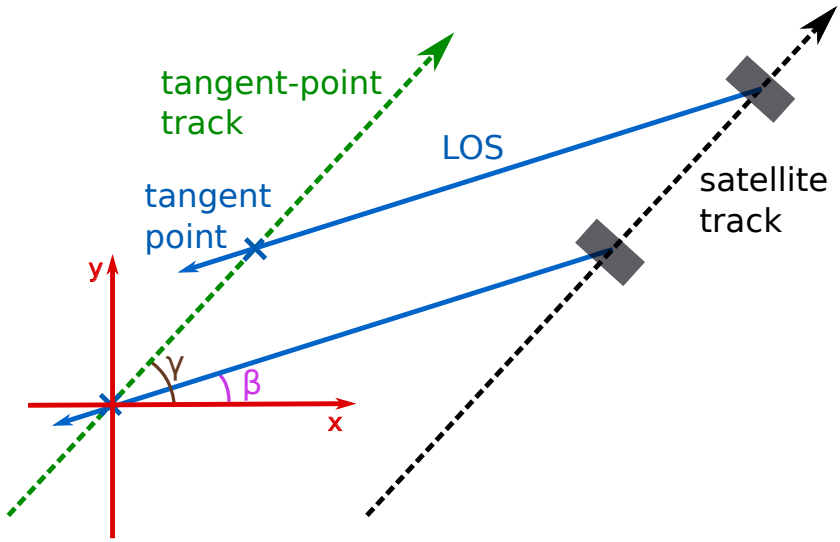

Figure 5.5: Satellite observation geometry in the local coordinate system in the two-dimensional horizontal plane. The black dashed line indicates the satellite track, while the green dashed line shows the tangent-point track. Blue lines are LOS. Red axes represent the local coordinate system. For details see text.

(q_0); bottom level (z_b) and top level (z_t) of the diabatic forcing; and moving speed of the diabatic forcing (c_q). The first three quantities were taken from latent heat data of three-hourly MERRA (modern-era retrospective analysis for research and applications) assimilated data for January 2008. The fourth is taken from the wind profile of MERRA data. MERRA data are reanalysis data provided by NASA. These data employ a major new version of the Goddard Earth Observing System Data Assimilation System Version 5 (GEOS-5). MERRA data contain several ground based, in-situ, and satellite measurements. Resolutions of MERRA data are $1/2\,^\circ$ and $2/3\,^\circ$ in longitude and latitude, respectively. In the vertical direction, MERRA data contains 72 levels up to 70 km with assimilated satellite data up to the middle mesosphere. In the current study, only data with assimilated satellite data are used and simulations are performed up to 50 km altitude. Several studies (e.g. *Bosilovich et al.*, 2011) have shown the reliability of MERRA data, especially for precipitation and heating rates. More detailed information about MERRA data as well as convective parameterization in MERRA can be found, for instance, in *Rienecker et al.* (2011); *Kim and Alexander* (2013); *Wright and Fueglistaler* (2013).

Two free parameters of the parameterization are the spatial and temporal scales (δx and δt) of the diabatic forcing. We considered three different sets of δx and δt, namely MF1 ($\delta x = 5$ km and $\delta t = 20$ min), MF2 ($\delta x = 25$ km and $\delta t = 60$ min) and MF3 ($\delta x = 120$ km and $\delta t = 60$ min) [1]. The combination of MF1 and MF2

[1]Convective parameterizations comprehend a simplified physical description of the entire dynamics of a convective system and provide only the net effects to the general circulation model. They do not provide explicit information on, e.g., the spatial scale or on the moving-speed of clouds which are therefore important free parameters of the CGWS scheme (the moving speed in terms of a representative height; for this height the background winds are assumed to

showed good agreement in spatial distribution as well as magnitude with AIRS observations (*Choi et al.*, 2012). However, it is unable to explain the spectral peaks found by *Ern and Preusse* (2012). A possible reason is that MF1 and MF2 do not describe the presence of convective clusters, which could be represented by MF3.

In order to obtain spectral distributions in terms of horizontal and vertical wave numbers (wavelengths), GWMF with corresponding horizontal and vertical wave numbers were calculated directly from the ray-tracing simulation for an altitude of 25 km. We considered global means, but took into account the latitude coverage of satellite instruments, which were mentioned in Sect. 5.2. It should be mentioned that, although the global mean is taken, the resulting spectrum will be dominated by the tropics and subtropics because the dominant convective gravity wave sources are located there. The respective simulated GWMF (symbolized by F) values were then binned according to horizontal and vertical wave numbers (k_h and m) using a technique similar to that of *Ern and Preusse* (2012). All spectra were plotted in a base 10 logarithmic scale, i.e. $\widetilde{k}_\mathrm{h} = \log_{10}(1/\lambda_\mathrm{h})$ and $\widetilde{m} = \log_{10}(1/\lambda_z)$, where λ_h and λ_z are the horizontal and vertical wavelengths, respectively. The size of each bin was set as $\delta\widetilde{k}_\mathrm{h} = 0.1$ and $\delta\widetilde{m} = 0.1$. The simulated spectral distribution is called "true spectral distribution" (or "true spectrum") because this would be the atmospheric spectrum, if the model were to accurately represent the real atmosphere. In the following sections, we will discuss how this contrasts to a spectrum that would be observed by an infrared limb sounder. An example of the true spectrum for January 2008 for the parameter set MF1 is shown in Fig. 5.6a.

5.4 The comprehensive observational filter

Based on the convective model and parameter settings for MF1, MF2 and MF3 described in Sect. 5.3 GWMF spectra were generated. In this section, we outline how an infrared limb sounder would observe these spectra, i.e. these spectra serve as reference for the influence of the observational filter. For short we will call these spectra therefore "true spectra" where "true" refers only to not being modified by any observational effects. The application of the comprehensive observational filter comprises four main processes. Each process is explained in one of the following subsections. The effects of each of these processes are shown in Fig. 5.6 by applying the observational filter for the observation geometry of the SABER instrument to

drive the moving speed). For MF1 and MF2 the assumed spatial scales δx are much smaller than a typical GCM grid distance and we have a physical consistent picture of two subgrid parameterizations. The picture is less consistent, though, if the assumed size of the convective system δx exceeds the grid spacing of the GCM. Still, such choices may be necessary, if the global gravity wave distribution shall be solely described by the ray-tracer, or if due to missing dynamical feedback between the convection parameterization and the GCM dynamical core such waves are not generated in the model (*Preusse et al.*, 2014). In this case they would need to be parameterized even if the model in principle is able to resolve the waves.

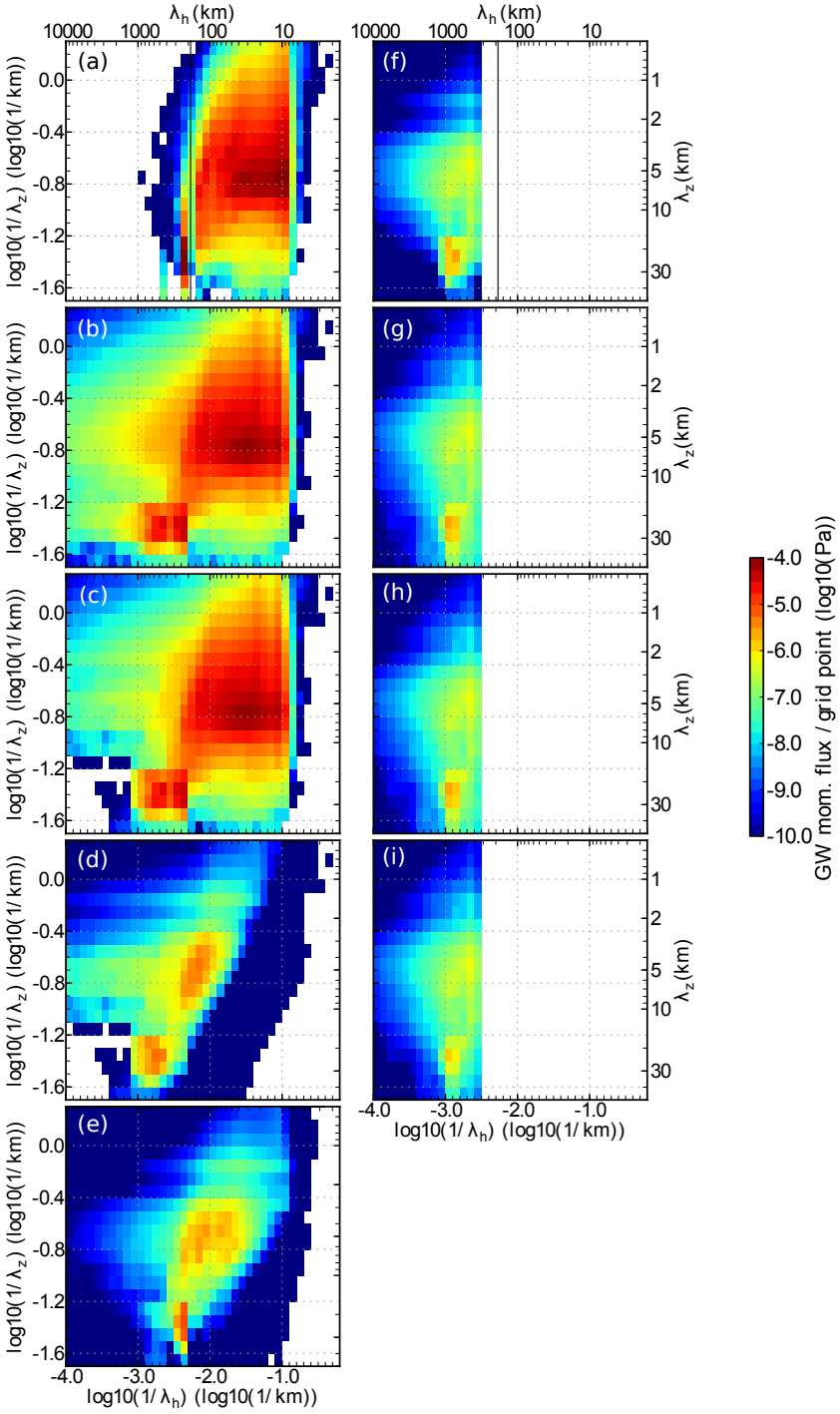

Figure 5.6: Spectral distributions of MF1 through different steps of the observational filter for January 2008 with the observation geometry of SABER, where **(a)** is the true spectrum, **(b)** along-LOS spectrum, **(c)** λ_{h} restriction spectrum, **(d)** instrument-sensitivity spectrum, **(e)** projection-on-track spectrum, **(f)** aliasing-effect spectrum, **(g)** $\lambda_{z,\,\mathrm{obs}}$ spectrum, **(h)** λ_z restriction spectrum, **(i)** observed spectrum (after the additional correction). Black vertical lines in panels (a) and (f) indicate $\lambda_h = 185$ km. For details see text.

the spectral distribution from MF1. The reason for choosing MF1 and SABER is that MF1 has the shortest spatial scale among the three parameterized spectra and that SABER has a longer sampling distance than HIRDLS. The effects of the filter on the GWMF spectrum are therefore most pronounced in this case.

5.4.1 Visibility filter

First, we consider the effects due to radiative transfer and retrieval, which also limit the waves that are visible to the instrument. We use an analytical approximation of the 2-D visibility filter for infrared limb sounding, which was derived by *Preusse et al.* (2002). This filter is based on two-dimensional cross sections through quasi-monochromatic waves. *Preusse et al.* (2002) assumed that all LOSs of a given profile form a two-dimensional plane consisting of the vertical and one horizontal axis in the viewing direction of the instrument. The similar approach was also applied for analyzing the visibility of gravity waves measured by radio occultation in the paper of *Lange and Jacobi* (2003).

Following the analytical approach of *Preusse et al.* (2002), the instrument sensitivity of infrared limb sounders for temperature amplitude is:

$$S = \frac{\lambda_z \sqrt{2}}{2\pi\Delta_z} \sqrt{1 - \cos\left(\frac{2\pi\Delta_z}{\lambda_z}\right)} \exp \frac{-cb^2}{4(c^2 + a^2)} \tag{5.1}$$

where $a = m/2R_\mathrm{E} = \pi/(\lambda_z R_\mathrm{E})$, $b = k_\mathrm{h} = 2\pi/\lambda_\mathrm{h}$, $c = 1/(2HR_\mathrm{E})$ and R_E is the Earth's radius, H scale height, k_h horizontal wave number and m vertical wave number. The values of R_E and H are 6350 and 7 km, respectively. The vertical resolution Δz is 2 km for SABER and 1 km for HIRDLS.

As shown by *Ern et al.* (2004), GWMF can be deduced from the temperature amplitude of the wave using Eq. 2.11. The sensitivity function σ for GWMF, according to Eq. (2.11), is therefore obtained by squaring the temperature amplitude ratio:

$$\sigma = S^2 \tag{5.2}$$

Figure 5.7 illustrates the sensitivity function σ for GWMF from (a) SABER and (b) HIRDLS. Comparing these two sensitivities, it is evident that HIRDLS has higher sensitivity owing to its higher vertical resolution, especially at short vertical wavelengths. For HIRDLS, a reasonable sensitivity (0.3) can be found down to a vertical wavelength of about 2 km, whereas for SABER, this limit is approximately 3.5 km. Sensitivities of the two instruments in the horizontal direction are comparable. The visibility function is a function of two variables: the vertical wavelength and the projection of the horizontal wavelength onto the LOS (see below). Figure 5.8 combines the viewing geometry of the satellite with the geometry of the observed gravity wave in the horizontal plane. In this figure, part of an exemplary wave is shown by the dashed grey curve. The red arrow

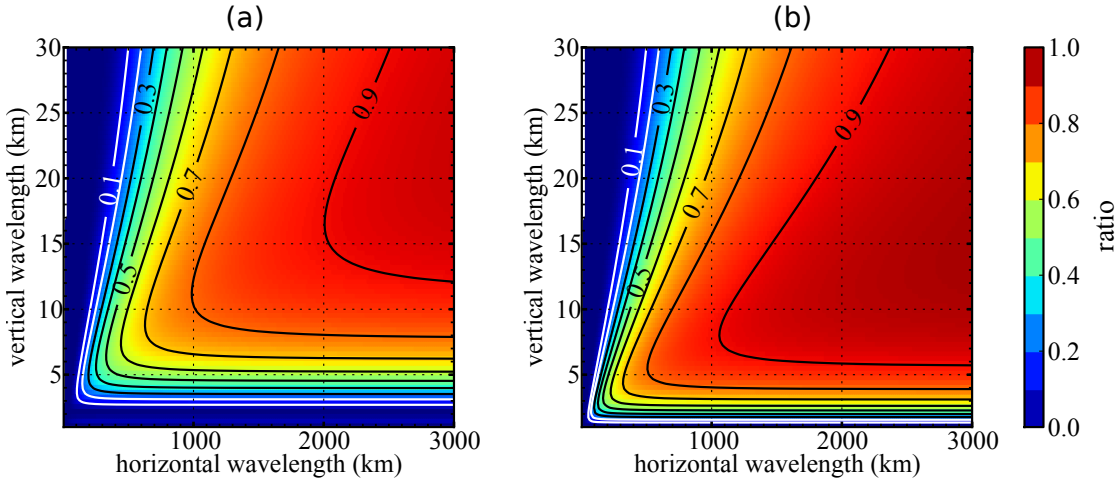

Figure 5.7: Two-dimensional sensitivity function for GWMF of **(a)** SABER and **(b)** HIRDLS.

indicates the direction of the wave vector and purple lines indicate wave fronts. ψ is the angle between the wave vector and the x direction of the local coordinate system ($\psi = \arctan(l/k)$ where k, l are wave numbers in x and y directions, respectively). The horizontal wavelength λ_{h} is shown by the two-headed arrow, which is perpendicular to the wave fronts and parallel to the wave vector. The horizontal wavelength along LOS ($\lambda_{\mathrm{h,\,LOS}}$), on the other hand, is parallel to the LOS (blue line) and is, in general, longer than λ_{h}. Knowing λ_{h} and the angle β, the along-LOS horizontal wavelength $\lambda_{\mathrm{h,\,LOS}}$ can be calculated as follows:

$$\lambda_{\mathrm{h,\,LOS}} = \frac{\lambda_{\mathrm{h}}}{|\cos(\psi - \beta)|} \tag{5.3}$$

Figure 5.6b shows the spectrum of F with respect to $\lambda_{\mathrm{h,\,LOS}}$ and λ_z. It is referred to as "along-LOS spectrum" hereafter. This spectrum, as we would expect, spreads in the direction of longer horizontal wavelengths.

The application of the visibility filter as described above assumes infinite plane wave fronts. However, three dimensional simulations of convective gravity waves from single convective towers exhibit concentric wave fronts (*Piani et al.*, 2000; *Lane et al.*, 2001). The assumption therefore is clearly non-realistic, in particular for short period, short horizontal wavelength convective gravity waves. This is problematic in cases where the horizontal wave vector is almost perpendicular to the horizontal LOS, the along-LOS wavelength approaches infinity, and the wave would therefore be regarded as visible. However, in a three-dimensional consideration, the LOS would still intersect many wave fronts resulting in a vanishing net signal. Thus, these waves should not be regarded as visible. In order to mask all waves which have short horizontal wavelengths but are only seemingly visible, we

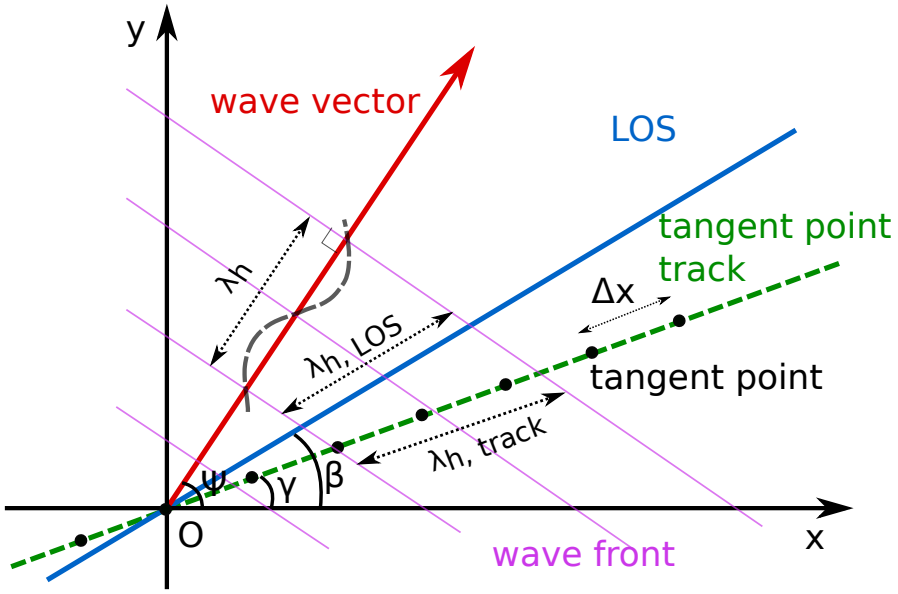

Figure 5.8: Combination of the satellite's viewing geometry and the geometry of the observed gravity wave. One LOS (blue line) is shown for the tangent point at the origin. The horizontal wavelength along LOS ($\lambda_{\mathrm{h,\,LOS}}$) can be calculated knowing the true horizontal wavelength (λ_{h}) and angles β, ψ. The projection of horizontal wavelength on tangent-point track can be calculated knowing the true horizontal wavelength (λ_{h}) and angles γ, ψ. For details see text.

firstly introduce a "stretching" factor:

$$\theta_{\mathrm{str}} = \frac{\lambda_{\mathrm{h,\,LOS}}}{\lambda_{\mathrm{h}}} \tag{5.4}$$

and secondly, we simultaneously consider whether the horizontal wavelength is short compared to the shortest visible horizontal wavelength. Here, the shortest visible horizontal wavelength is determined as the value of λ_{h} from Eq. (5.1) corresponding to a temperature sensitivity of 0.3:

$$\lambda_{\mathrm{vis}} = \lambda_{\mathrm{vis}}(\lambda_z,\ S = 0.3) \tag{5.5}$$

We also introduce the visibility ratio as:

$$\theta_{\mathrm{vis}} = \frac{\lambda_{\mathrm{h}}}{\lambda_{\mathrm{vis}}}. \tag{5.6}$$

and threshold values of θ_{str} and θ_{vis} are denoted as $\theta_{\mathrm{str,\,thresh}}$ and $\theta_{\mathrm{vis,\,thresh}}$, respectively. All waves, which have too large stretching factors ($\theta_{\mathrm{str}} > \theta_{\mathrm{str,\,thresh}}$) and simultaneously have too short horizontal wavelengths ($\theta_{\mathrm{vis}} < \theta_{\mathrm{vis,\,thresh}}$), are set to zero temperature amplitude as well as to a zero GWMF value. For this study, we chose $\theta_{\mathrm{str,\,thresh}} = 5$ and $\theta_{\mathrm{vis,\,thresh}} = 1$. As shown later, results are not

very sensitive on the choice of these threshold values (cf. Fig. 5.15). This restriction was applied before the application of the instrument sensitivity function. GWMF values after considering this restriction are given by F_{restr}. A spectral distribution of F_{restr} with respect to $\lambda_{\mathrm{h,\ LOS}}$ and λ_z, which is called "λ_{h}-restriction spectrum" hereafter, is shown in Fig. 5.6c, again using $\lambda_{\mathrm{h,\ LOS}}$ for the x axis. Comparing with Fig. 5.6b, it can be seen that part of the spectral distribution at long λ_z and long $\lambda_{\mathrm{h,\ LOS}}$ is removed.

After this consideration of the horizontal wavelength restriction, the sensitivity function was applied to GWMF. An example of this application of the SABER sensitivity function on MF1 is shown in Fig. 5.6d. This spectrum is referred to as "instrument-sensitivity spectrum" hereafter. In comparison with the previous spectrum (Fig. 5.6c), it is clear that a significant part of the spectrum associated with short vertical and horizontal wavelengths has been filtered out. The area of high-value GWMF has now shifted to the direction of longer horizontal as well as vertical wavelengths. GWMF values after applying the sensitivity function are denoted as F_{vis}.

5.4.2 Projection of the wavelength on the tangent-point track

Today's limb scanning satellite instruments provide information only along track. Therefore, from the observations of current limb sounders only the projection of the horizontal wavelength on the tangent-point track can be estimated (*Ern et al.*, 2004; *Preusse et al.*, 2009b). The horizontal sampling of current-day satellite observations is too sparse to directly infer the horizontal wavelength. This problem is circumvented by first analyzing vertical profiles and determining vertical wavelengths, amplitudes and phases dependent on altitude. The horizontal wavelength is then estimated from the phase difference of adjacent profiles at the same altitude and the distance between observations along the tangent-point track. The method was first introduced by *Ern et al.* (2004). Although there are different applications with respect to the profile analysis (*Alexander et al.*, 2008; *Wright et al.*, 2010) they all rely on phase differences along the orbital track. In particular, if the phase difference is $\Delta\Phi$ and the sampling distance between two altitude profiles is Δx, the horizontal wave number and horizontal wavelength along the tangent-point track ($k_{\mathrm{h,\ track}}$ and $\lambda_{\mathrm{h,\ track}}$) can be estimated as follows:

$$k_{\mathrm{h,\ track}} = \frac{\Delta\Phi}{\Delta x} = \frac{2\pi}{\lambda_{\mathrm{h,\ track}}} \tag{5.7}$$

In our simulation $\lambda_{\mathrm{h,\ track}}$ was calculated from the horizontal wavelength λ_{h} based on the geometric relation between them. This geometric relation is illustrated also in Fig. 5.8. In this figure, black dots are tangent points and the green dashed line shows the tangent-point track. The horizontal wavelength along the tangent-point track ($\lambda_{\mathrm{h,\ track}}$) is indicated by the two-headed arrow, which is parallel to

the tangent-point track. It is clear that the angle between the wave vector and the tangent-point track is $\psi - \gamma$. From here:

$$\lambda_{\mathrm{h,\ track}} = \frac{\lambda_{\mathrm{h}}}{|\cos(\psi - \gamma)|} \tag{5.8}$$

Due to the projection, the horizontal wave number is changed in Eq. (2.11), and as GWMF and horizontal wave number are proportional, the momentum flux calculated from $\lambda_{\mathrm{h,\ track}}$ is:

$$\frac{F_{\mathrm{track}}}{F_{\mathrm{vis}}} = \frac{k_{\mathrm{h,\ track}}}{k_{\mathrm{h}}} = \frac{\lambda_{\mathrm{h}}}{\lambda_{\mathrm{h,\ track}}} \tag{5.9}$$

or:

$$F_{\mathrm{track}} = F_{\mathrm{vis}} \frac{\lambda_{\mathrm{h}}}{\lambda_{\mathrm{h,\ track}}} \tag{5.10}$$

A spectral distribution of F_{track} in terms of $\lambda_{\mathrm{h,\ track}}$ and λ_z is shown in Fig. 5.6e. This spectrum is called "projection-on-track spectrum" hereafter and contains both the effects of visibility filtering and along-track projection.

5.4.3 Aliasing effect

Calculation of horizontal wavelength due to the aliasing effect

Satellite measurements are performed discretely which leads to a so-called aliasing effect, one of the well-known limitations of discrete sampling. The Nyquist theorem states that two samples per wave period or wavelength are necessary to properly resolve the wave. In other words, sampling distance Δx of less than a half of $\lambda_{\mathrm{h,\ track}}$ is required to properly infer the wave structure from the observed data.

For SABER, $\Delta x = 185\,\mathrm{km}$ was used as the sampling distance for our calculations. In the case of HIRDLS, Δx is different for different operation periods. The shortest pair distance at the altitude of 25 km was about 70 km and we used $\Delta x = 70\,\mathrm{km}$ for calculations of HIRDLS. More details about sampling distances of various satellite instruments can be found in *Ern et al.* (2011).

In order to estimate the horizontal wavelength caused by the aliasing effect ($\lambda_{\mathrm{h,\ alias}}$), we emulated the phase-difference method applied to the measurements. First, the phase difference $\Delta\Phi$ between two adjacent vertical profiles is required. From Eq. (5.7), $\Delta\Phi$ can be defined as follows:

$$\Delta\Phi = k_{\mathrm{h,\ track}} \Delta x = \frac{2\pi\Delta x}{\lambda_{\mathrm{h,\ track}}} \tag{5.11}$$

Without further information, we had to assume that phase differences $\Delta\Phi$ are in

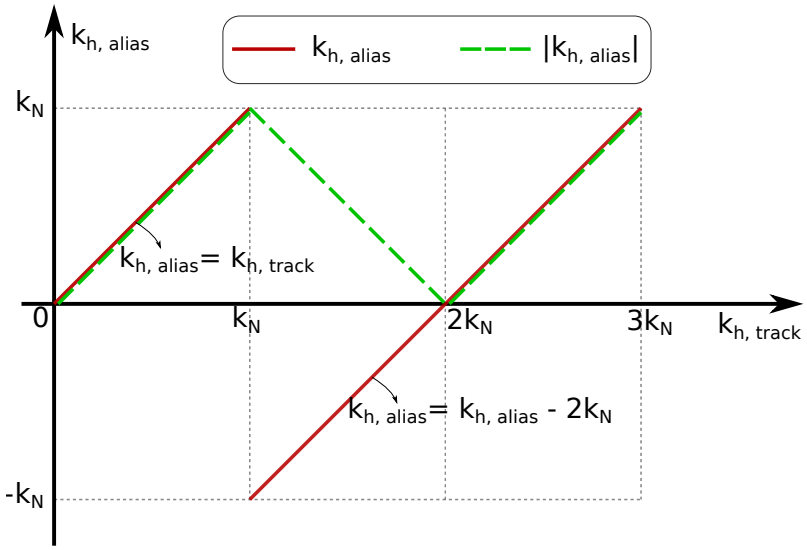

Figure 5.9: "Alias" wave number vs. wave number along tangent-point track.

the interval $[-\pi,\ \pi]$ despite the fact that the real phase differences may be larger. This is in accordance with the Nyquist theorem, where a phase difference larger than π causes a wavelength shorter than the Nyquist wavelength, which is twice the sampling distance: $\lambda_{\mathrm{N}} = 2\Delta x$, where λ_{N} is the Nyquist wavelength.

Hence, in the current work, the phase difference $\Delta\Phi$ given by Eq. (5.11) was wrapped into interval $[-\pi,\ \pi]$. This wrapping process provided $\Delta\Phi_{\mathrm{wrap}} \in [-\pi,\ \pi]$ and the absolute value of the horizontal wave number due to aliasing effect ($k_{\mathrm{h,\ alias}}$) can be calculated as follows:

$$|k_{\mathrm{h,\ alias}}| = \frac{|\Delta\Phi_{\mathrm{wrap}}|}{\Delta x} \tag{5.12}$$

The dependence of $k_{\mathrm{h,\ alias}}$ and $|k_{\mathrm{h,\ alias}}|$ upon $k_{\mathrm{h,\ track}}$, for instance, in the interval $\Delta\Phi \in [0,\ 3\pi]$, is illustrated in Fig. 5.9. Here k_N is the Nyquist limit of horizontal wave number:

$$k_N = \frac{\pi}{\Delta x} \tag{5.13}$$

Using the wrapped phase difference, $\lambda_{\mathrm{h,\ alias}}$ can be defined:

$$\lambda_{\mathrm{h,\ alias}} = \frac{2\pi}{|k_{\mathrm{h,\ alias}}|} = \frac{2\pi\Delta x}{|\Delta\Phi_{\mathrm{wrap}}|} \tag{5.14}$$

Calculation of GWMF corresponding to $\lambda_{\text{h, alias}}$

In analogy to the deduction of Eq. (2.11), the relation between F_{track} and GWMF corresponding to the aliased horizontal wavelength (F_{alias}) is:

$$\frac{F_{\text{alias}}}{F_{\text{track}}} = \frac{k_{\text{h, alias}}}{k_{\text{h, track}}} = \frac{\lambda_{\text{h, track}}}{\lambda_{\text{h, alias}}} \tag{5.15}$$

or:

$$F_{\text{alias}} = F_{\text{track}} \frac{\lambda_{\text{h, track}}}{\lambda_{\text{h, alias}}} \tag{5.16}$$

The spectral distribution of F_{alias} with respect to $\lambda_{\text{h, alias}}$ and λ_z is hereinafter referred to as the "aliasing-effect spectrum" and the aliasing-effect spectrum for MF1, January 2008 is shown in Fig. 5.6f. In comparison with the spectrum of the previous step (Fig. 5.6e), a notably large part of the spectral distribution is cut off and flipped to the left, i.e. to longer horizontal wavelengths. The cut-off part is associated with horizontal wavelengths shorter than the Nyquist wavelength of $2\Delta x = 370\,\text{km}$. Some GWMF is added to the left part of the spectrum, at wavelengths corresponding to aliased horizontal wavelengths $\lambda_{\text{h, alias}}$. The additional GWMF in the left part is according to Eq. (5.16) smaller than the original GWMF on the right-hand side of Fig. 5.6e since $\lambda_{\text{h, alias}}$ is longer than $\lambda_{\text{h, track}}$ for these waves. In this aliasing-effect spectrum of MF1, artificial peaks were caused by the aliasing effect at horizontal wavelengths of about 800 km. Overall, the magnitude of GWMF was reduced notably.

5.4.4 Calculation of observed vertical wavelength

Altitude profiles sampled by most limb sounders are non-vertical, which is an effect that also has to be considered. For SABER and HIRDLS this applies and the effect is investigated and taken into account in our simulations. In particular, we calculate the vertical wavelength, which would be observed by the satellite instrument. This wavelength is referred to as observed vertical wavelength hereafter.

From observations, the vertical wavelength is derived by analyzing altitude profiles as provided by the instrument teams. It is generally assumed that these altitude profiles are vertical and that therefore only the vertical wave structure contributes to the wave structure in the profile. However, for SABER and HIRDLS, scans are not strictly vertical: The change in altitude is performed by upward and downward scanning by the instrument. However, during upward and downward scanning, the satellite moves along its track. This leads to a slant of the profile in the direction along the tangent-point track. Also, when the LOS moves up (down), the tangent-point becomes closer to (further from) to the satellite (cf. Fig. 5.1). This leads to another slant of the profile in the direction across the tangent-point track. Because of the slant of the altitude profiles it can happen that during an

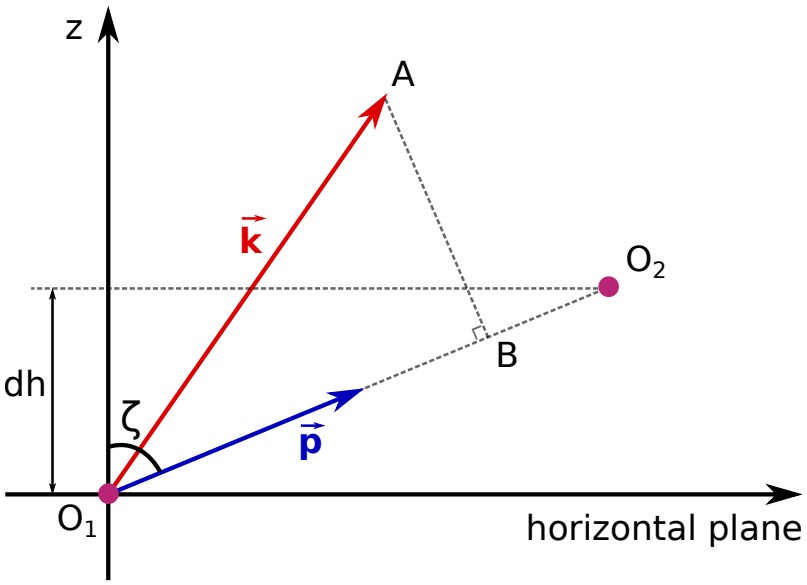

Figure 5.10: Observation geometry at a tangent point of an altitude profile. Two purple dots (O_1 and O_2) represent two tangent points. The red arrow shows the wave vector, while the blue arrow is the normalized vector of the profile vector. dh is the altitude difference between O_1 and O_2.

altitude scan not only the vertical structure of an observed wave is sampled, but also to some extent the horizontal structure.

In Fig. 5.10, two exemplary tangent points O_1, O_2 along an altitude profile are illustrated (purple dots). This could correspond to any pair of adjacent altitudes in a scan such as illustrated in Fig. 5.1. A local coordinate system at tangent point O_1 is shown where the z axis indicates the vertical direction. The altitude difference dh between two tangent points O_1 and O_2 is small (we chose d$h = 3\,\mathrm{km}$), so that the vector $\overrightarrow{O_1O_2}$ was considered to be the local profile vector. If $\vec{p}$ (blue vector) is the normalized vector of $\overrightarrow{O_1O_2}$ and $\vec{k}$ (red vector) is the wave vector, then the wave number along the profile can be defined as the scalar product of $\vec{k}$ and $\vec{p}$:

$$m_\mathrm{p} = \vec{k} \cdot \vec{p} \tag{5.17}$$

The wavelength along the profile is:

$$\lambda_{z,\,\mathrm{p}} = \frac{2\pi}{m_\mathrm{p}} \tag{5.18}$$

From $\lambda_{z,\,\mathrm{p}}$ and from the angle ζ between the normalized profile vector $\vec{p}$ and the z axis of the local coordinate system (cf. Fig. 5.10), the observed vertical

wavelength $\lambda_{z,\,\mathrm{obs}}$ is calculated:

$$\lambda_{z,\,\mathrm{obs}} = \lambda_{z,\,\mathrm{p}} \cos\zeta \tag{5.19}$$

Momentum flux corresponding to this vertical observed wavelength is symbolized as $F_{z,\,\mathrm{obs}}$. Following Eq. (2.11), GWMF is inversely proportional to the vertical wave number and thus proportional to the vertical wavelength:

$$F_{z,\,\mathrm{obs}} = F_{\mathrm{alias}} \frac{\lambda_{z,\,\mathrm{obs}}}{\lambda_z} \tag{5.20}$$

In a statistical average we will have as many upward-scanning observations as downward-scanning observations. Therefore, we calculate both solutions for each wave and show the average. The spectrum with observed vertical wavelength hereafter is referred to as "$\lambda_{z,\,\mathrm{obs}}$ spectrum" and an example for MF1 is shown in Fig. 5.6g. The spectrum was slightly redistributed towards longer vertical wavelengths. In particular, for vertical wavelengths longer than 6 km, GWMF was slightly enhanced.

For every wave, we also examined the difference between the observed vertical wavelengths for the upward and downward scans. If this difference is greater than 40 % of the average vertical wavelength, this wave will be rejected. We here follow the GWMF determination from real observations as described in *Ern et al.* (2011), where such pairs of profiles are not used by the MF calculation method. It should be noted that for other methods of MF calculation, these pairs may be used.

We symbolize GWMF after this restriction as $F_{z,\,\mathrm{obs,\,restr}}$. The spectrum with this restriction, called "λ_z-restriction spectrum" later, is shown in Fig. 5.6h. In comparison with the previous spectrum (Fig. 5.6g), only minor changes were found. In particular, the magnitude of GWMF surrounding the spectral peak at vertical wavelength of about 5 km was reduced slightly.

In the last step of the observational filter, we applied an additional correction, which was used in *Ern et al.* (2011). First, this correction removes dominant vertical oscillation of quasi-stationary planetary waves (which have a vertical wavelength ≥ 40 km) in the altitude profiles. Second, it helps to keep only those vertical wavelengths for which amplitudes can reliably be determined in the 10 km vertical window of the Maximum Entropy Method/Harmonic Analysis (MEM/HA) spectral analysis (*Preusse et al.*, 2002; *Ern et al.*, 2011). The GWMF at this last step is denoted as F_{obs}.

This is the final step of our comprehensive observational filter. The resulting spectrum is therefore considered to represent the observed spectrum and is presented in Fig. 5.6i. In comparison with Fig. 5.6h, it can be seen that contributions of long vertical wavelength waves were somewhat reduced. However, the overall spectrum is changed only slightly.

A comparison of this observed spectrum and the true spectrum (Fig. 5.6a) shows that the spectral distribution of MF1 is significantly influenced by the obser-

vational filter in both shape and magnitude. In particular, the observed spectrum consists of horizontal wavelength for which MF1 did not generate any wave events and vice versa. This is due to the fact that MF1 has a small spatial scale and produces a large amount of short horizontal wavelength gravity waves, which can hardly be observed by limb sounders. However, as mentioned before, for demonstrating the different effects of the observational filter, MF1 was chosen because the different effects contributing to the observational filter can be demonstrated clearly. Later in the manuscript we will address other setups of the CGWS that produce wave spectra that can be better observed.

All steps of the observational filter are summarized by a flowchart in Fig. 5.11. The steps with significant changes are marked by bold characters. Additional examples of applying the observational filter to all three spectra MF1, MF2, MF3 using the observation geometries of SABER as well as HIRDLS will be presented in Sect. 5.5 below.

5.5 Further examples

5.5.1 Applying the observational filter to observation geometry of SABER

In Sect. 5.4, we illustrated the observational filter by applying it to the spectrum of MF1 and using SABER geometry. In this section, we provide further examples by applying the observational filter to all spectra MF1, MF2 and MF3 and using observation geometry of both instruments (SABER and HIRDLS).

For SABER geometry, the results of applying the observational filter are presented in Fig. 5.12. As shown by "true" simulated spectra (Fig. 5.12a, g, and m), MF3 provides gravity waves with the longest horizontal wavelength. The main spectral peak of MF3 is at a horizontal wavelength of about 220 km. It has some substructure and extends to λ_h as high as few hundred km. For MF2 and MF1, this peak is located at horizontal wavelengths of about 50 and 10 km, respectively. It should be noted that the spatial scale of the cloud tower specified in the source model is imagined to act as a single bodyforce without substructure. Therefore, no waves with wavelength of the order or shorter than this bodyforce are excited. Instead, the model produces a sharp onset at the wavelength of twice this size. This sharp onset is pronounced at the source altitude. When gravity waves propagate upward, the wavelength may be modified by horizontal refraction (e.g. *Marks and Eckermann*, 1995) which slightly weakens this sharp onset. In cases of MF1 and MF2, at the considered altitude of 25 km, this sharp onset still can be seen quite clearly.

Due to this difference in the spatial scale, the observational filter affects MF1, MF2 and MF3 differently. For example, the effect of the λ_h restriction (Sect. 5.4.1) on MF1 is recognizable by comparing Fig. 5.6b and c, while for MF2 and MF3, this effect is minor and indicated by only an insignificant decrease in GWMF at

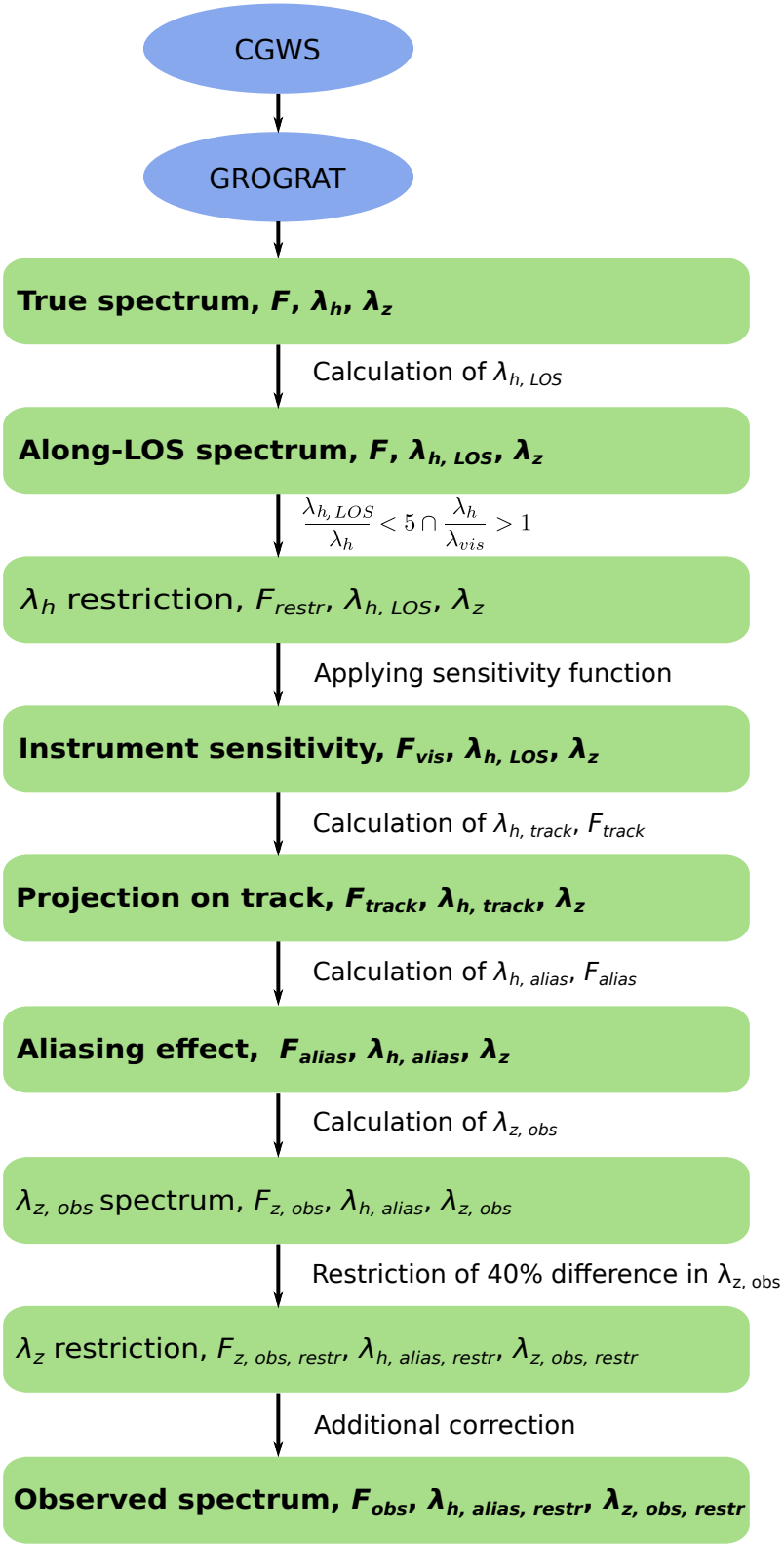

Figure 5.11: Overview of all steps the observational filter. The steps with significant changes are marked by bold characters.

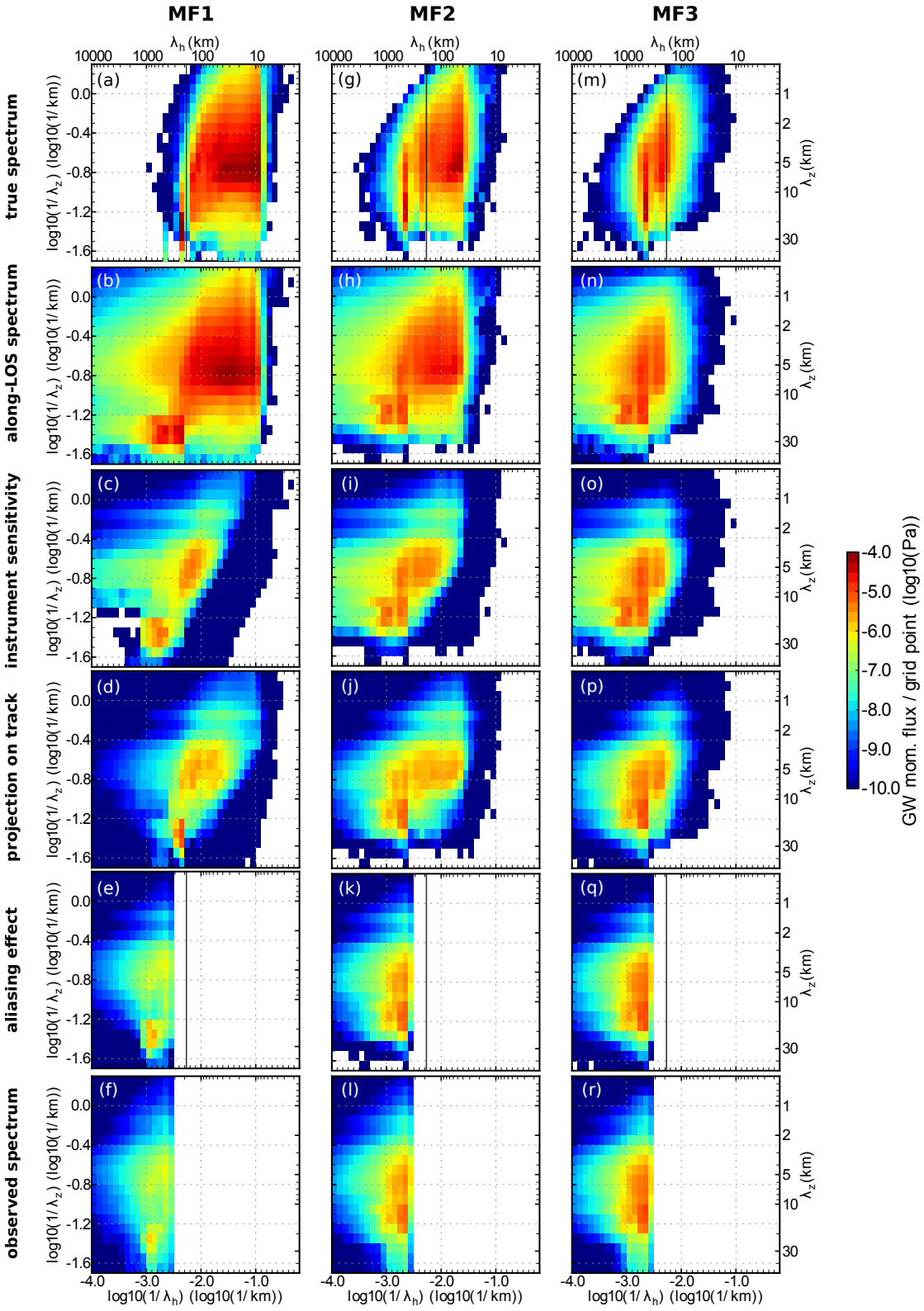

Figure 5.12: Application of the observational filter to MF1 (left column) MF2 (middle column), and MF3 (right column) for January 2008 with the observation geometry of SABER. Black vertical lines in the first and 5th rows indicate $\lambda_h = 185$ km.

long horizontal and vertical wavelengths (not shown).

However, differences can be seen much more clearly after the instrument sensitivity has been applied by comparing the second and third rows of Fig. 5.12. For MF1, a very large amount of GWMF corresponding to short horizontal as well as vertical wavelengths has been filtered out (cf. Fig. 5.12b and c). The spectral peak is shifted from a $\lambda_{\mathrm{h,\,LOS}}$ value of about 40 km (Fig. 5.12b) to a value of about 160 km (Fig. 5.12c). It should be noted that in this step, spectra are plotted with respect to the horizontal wavelength along LOS ($\lambda_{\mathrm{h,\,LOS}}$). The shift of the spectral peak with respect to the true horizontal wavelength (λ_{h}) in general is shorter. For MF2, the reduction in GWMF is considerably smaller than for MF1 (cf. Fig. 5.12h and i). Nevertheless, the GWMF magnitude is reduced quite strongly. The spectral shape changes and the area of strong GWMF moves to the direction of longer horizontal and vertical wavelengths. For MF3, part of the spectrum related to short wavelengths has also been filtered out (cf. Fig. 5.12n and o). This part, however, is smaller than for MF2 and although GWMF magnitude has decreased, the main spectral peak of MF3 remains at the same position (at $\lambda_{\mathrm{h,\,LOS}}$ of about 500 km).

Figure 5.12d, j, and p show spectra of F_{track} with respect to $\lambda_{\mathrm{h,\,track}}$ and λ_z. For MF1 and MF2, gravity waves with a horizontal wavelength shorter than 100 km contribute quite strongly to the spectrum (cf. Fig. 5.12d and j). High values of GWMF are even found at horizontal wavelengths down to about 20–30 km. In contrast, the main part of the spectrum of MF3 arises from by gravity waves with a horizontal wavelength greater than 100 km (cf. Fig. 5.12p). The influence of the aliasing effect on MF3 is therefore weaker than on MF1 and MF2. This is shown in Fig. 5.12e, k, and q. Since MF1 and MF2 contain many more short horizontal-wavelength gravity waves, an essential part of their spectra is projected to the left. For MF1, the features of the spectrum are changed significantly, as described before in Sect. 5.4. For MF2, a strong alteration is also found, although no strong artificial spectral peaks appear as in the case of MF1. In contrast, the part of MF3 projected to the left is minor in comparison with the originally long horizontal-wavelength part. Therefore, the strongest contribution to the spectrum in general, and the main peak in particular, still remains at the same position.

Figure 5.12f, l, and r shows observed spectra after the calculation of observed vertical wavelength, vertical wavelength restriction and additional correction. In comparison with aliasing-effect spectra, very minor changes were found for all spectra. In particular, spectra were redistributed slightly in the direction of longer vertical wavelengths, making them somewhat more homogeneous in this direction. The spectral peak at a vertical wavelength of about 30 km of MF1 was reduced in magnitude.

Briefly, the spectrum for MF3 was least influenced by the observational filter. For horizontal wavelengths longer than the Nyquist wavelength, major features were still conserved. The spectrum of MF1 was most influenced and significant changes were found in both shape and magnitude.

5.5.2 Applying the observational filter to observation geometry of HIRDLS

The observation geometry of HIRDLS has a shorter horizontal sampling distance. HIRDLS also has a higher vertical resolution. The results of applying the observational filter to the observation geometry of HIRDLS are presented in Fig. 5.13.

In the case of HIRDLS, "true" spectra (Fig. 5.13a, g, and m) are very similar to "true" spectra for SABER. Minor differences result from the different latitude coverage.

However, in contrast to SABER, along-LOS spectra of HIRDLS spread more strongly towards longer horizontal wavelengths (Fig. 5.13b, h, and n). This is an effect of the average orientation of the simulated gravity waves with respect to different view angles of the two instruments. This effect depends not only on the differences in viewing geometry but also on the simulated distribution of gravity waves.

The effects of the horizontal wavelength restriction were similar to those observed for SABER observation geometry with minor reductions at long horizontal and vertical wavelengths for all three spectra (not shown).

However, HIRDLS possesses better sensitivity to short-wavelength gravity waves, particularly in the vertical direction. This weakens the influence of the instrument's sensitivity to all spectra. A comparison of Figs. 5.12c, i, o and 5.13c, i, o shows that in comparison with SABER, for HIRDLS, the amount of GWMF was not reduced as much by the instrument sensitivity. For HIRDLS, GWMF was still conserved quite well in the vertical direction down to λ_z of about 2 km, while for SABER this limit was about 4 km. In the horizontal direction, since spectra of HIRDLS geometry spread more strongly with respect to $\lambda_{\mathrm{h,\,LOS}}$, gravity waves appeared to be more sensitive to the instrument. Hence, the reduction of GWMF in the horizontal direction was also lower than for spectra based on SABER geometry.

This better conservation of GWMF for HIRDLS was also found in spectra of F_{track} with respect to $\lambda_{\mathrm{h,\,track}}$ and λ_z (cf. Fig. 5.13d, j, and p). The contribution of short vertical-wavelength gravity waves to these spectra is more pronounced than in the case of SABER (Fig. 5.12d, j, and p).

Moreover, due to the shorter sampling distance, spectra in the case of HIRDLS were less influenced by aliasing than for SABER. Comparing aliasing-effect spectra of HRIDLS (Fig. 5.13e, k, and q) and SABER (Fig. 5.12e, k, and q), it is evident that for HIRDLS, a smaller part of the respective spectrum for MF1 was cut and for MF3 projected towards longer horizontal wavelengths (before the aliasing effect could take effect). The remaining part of each spectrum is therefore larger and more features are conserved.

In particular, the spectrum for MF3 and HIRDLS including the observational filter shown in Fig. 5.13q is the only one which has a well-resolved maximum that also decreases at short horizontal wavelength, similar to the observations of *Ern and Preusse* (2012). For this case (MF3), the spectral peak of the "true" spectrum

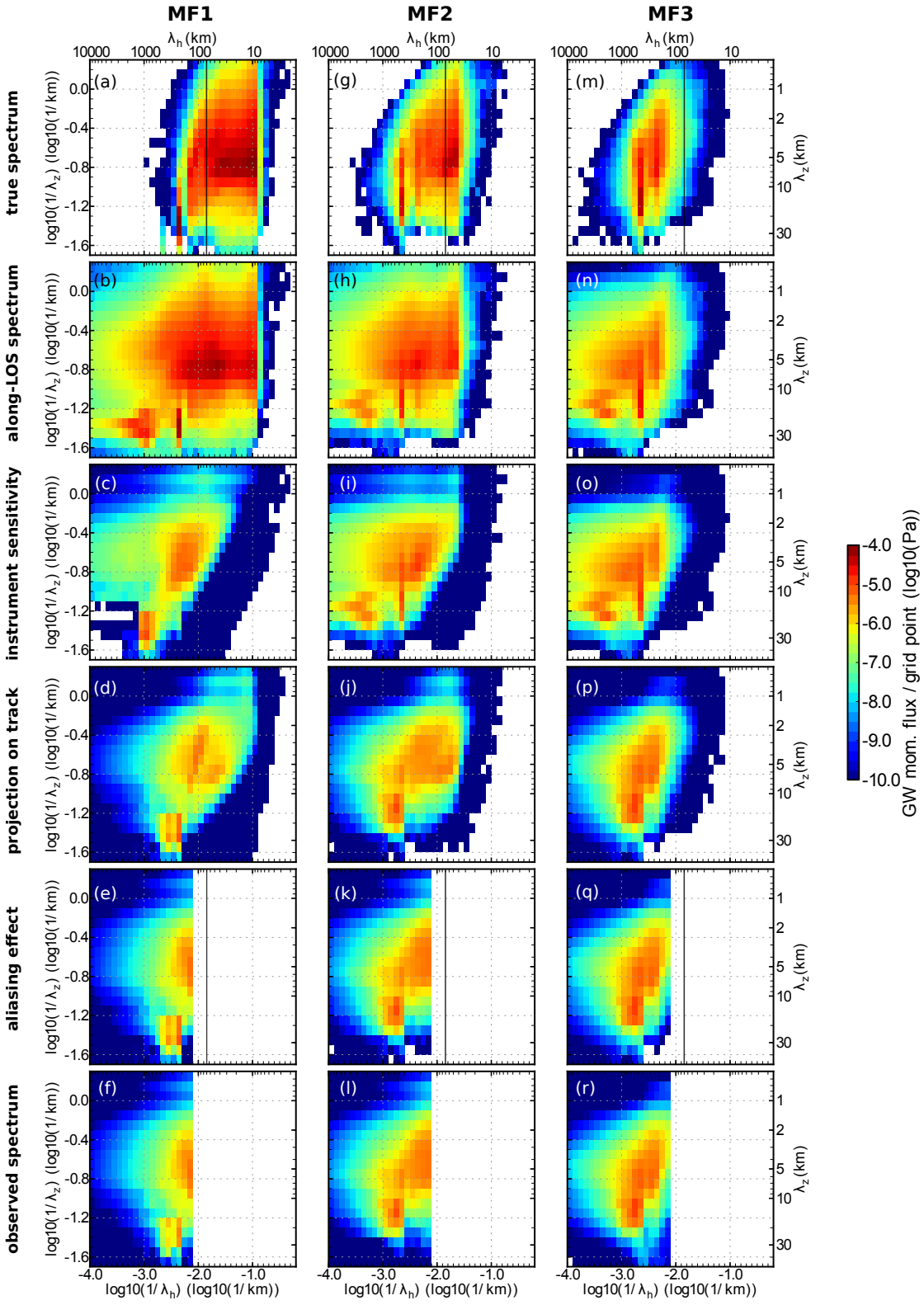

Figure 5.13: Application of the observational filter to MF1 (left column), MF2 (middle column) and MF3 (right column) for January 2008 with the observation geometry of HIRDLS. Black vertical lines in the first and 5th rows indicate $\lambda_h = 70$ km.

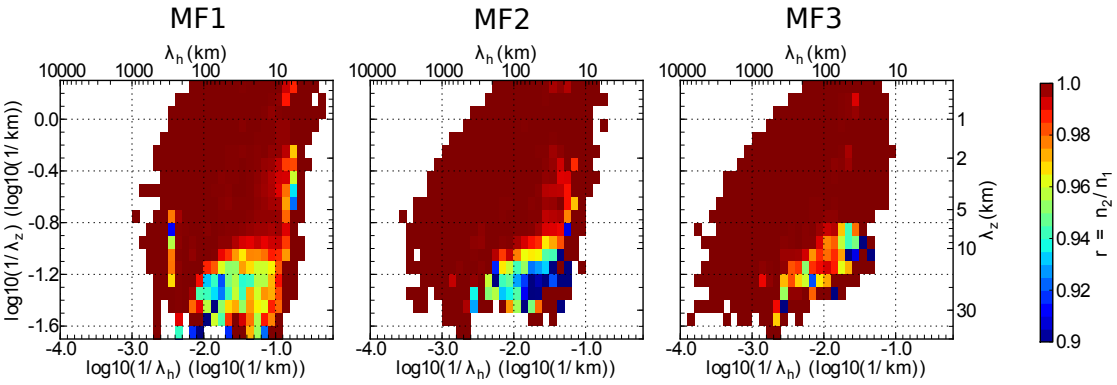

Figure 5.14: Variation of the number-of-wave-event spectrum after considering the difference between the observed vertical wavelengths for upward and downward scans. The variation is shown here for MF1 (left column), MF2 (middle column) and MF3 (right column) with the observation geometry of HIRDLS. For details see text.

is indeed captured by the observations.

Concerning the effect of "λ_z restriction", only an insignificant variation was found in the number of wave events for SABER (not shown). In the case of HIRDLS, this variation was more pronounced and the variation of the number-of-wave-event spectrum for HIRDLS is shown in Fig. 5.14. In this figure, the spectrum of the ratio $r = n_2/n_1$ is plotted with respect to the true horizontal and vertical wave numbers. Here, n_1 is the number of wave events in one bin before considering λ_z restriction, n_2 is the number of wave events in the same bin after considering this restriction. Reduced ratios were found in the lower right corner of the spectrum for all MF1, MF2 and MF3. This indicates that most of the filtered-out waves have short horizontal wavelength and long vertical wavelength. This can be explained as follows: when the horizontal wavelength is much longer than the vertical wavelength, the wave fronts are almost parallel to the horizon. In this case, the angle between the wave vector $\vec{k}$ and the normalized profile vector $\vec{p}$ is almost the same for upward scanning and downward scanning. Following Eqs. (5.17)–(5.19), the difference between observed vertical wavelengths in those two cases (upward and downward scan, respectively) is therefore insignificant. However, when horizontal wavelength and vertical wavelength are of the same order of magnitude, angles between $\vec{k}$ and $\vec{p}$ for upward and downward scanning are strongly different. This leads to a considerable difference in the observed vertical wavelengths. Figure 5.14 shows that even in the bins which were most affected, maximum profile loss was only about 10 %. On the other hand, profile loss in deriving data from HIRDLS observations using the method of *Ern et al.* (2011) was about 50 % (*Geller et al.*, 2013). This indicates that the λ_z restriction step cannot be the major reason for the observed loss of about 50 % of altitude profiles in real observations.

Figure 5.13f, l, and r shows "observed" spectra in the case of HIRDLS observation geometry. Again, in comparison with the aliasing-effect spectra, only minor

changes were found and these changes were analogous to the case of SABER.

Overall, similar to the case of SABER, MF3 was least affected while MF1 was most affected by aliasing. In particular for MF3, with observation geometry of HIRDLS, it was shown that almost all spectral features are preserved.

To conclude, for both cases of observation geometry (SABER and HIRDLS), all spectra (MF1, MF2 and MF3) shifted to the direction of longer horizontal as well as vertical wavelengths. A rather large part of each spectrum associated with short horizontal wavelengths was projected to longer horizontal wavelengths. The spectrum for MF3 has the longest spatial scale and was least influenced by the observational filter. In contrast, the spectrum for MF1 has the smallest spatial scale and was most influenced by the observational filter. The better sensitivity of HIRDLS helps to decrease the reduction of GWMF due to instrument sensitivity. In addition, HIRDLS's shorter sampling distance allows us to see a larger part of spectra after aliasing.

5.5.3 Quantification of GWMF reduction

As shown above, the magnitude of GWMF is decreased after applying filters mimicking λ_h restriction, instrument sensitivity, and aliasing. Moreover, the magnitude of GWMF also changes by calculating the observed vertical wavelength, the observed-vertical-wavelength restriction and additional correction. The changes during these last three steps, however, were minor, as we have seen from the spectra. In order to quantify the change in GWMF during the process of filtering, GWMF were integrated over all horizontal wave numbers and afterwards plotted against the vertical wave number in a base 10 logarithmic scale. The effects of the last three steps are discussed as one common step.

Figure 5.15 shows GWMF for SABER (left column) and HIRDLS (right column). The cyan dashed-dot line indicates GWMF of the true spectrum, the black solid line is GWMF after considering λ_h restriction, the blue dashed line presents GWMF after the instrument sensitivity has been considered, the orange line is GWMF after projecting on tangent-point track, the red line shows GWMF after the aliasing effect and the green line with crosses shows GWMF of the observed spectrum.

For both SABER and HIRDLS, the reduction due to the whole filtering process is largest for MF1 and smallest for MF3. It is indicated by the notable difference between GWMF of the true spectrum (cyan dashed-dot line) and the observed spectrum (green line with crosses). It is about 2.5 orders of magnitude for MF1 viewed by SABER (Fig. 5.15a) and about 2 orders of magnitude for MF1 viewed by HIRDLS (Fig. 5.15d). This difference is smaller in the case of MF2 (Fig. 5.15b and e) and is smallest in the case of MF3 (Fig. 5.15c and f). For MF3, the difference is only about half an order of magnitude. This agrees well with the fact that the spectrum for MF1 is most influenced and the spectrum for MF3 is least influenced by the observational filter, as discussed above.

Moreover, for all spectra and for both observation geometries, it is clear that the

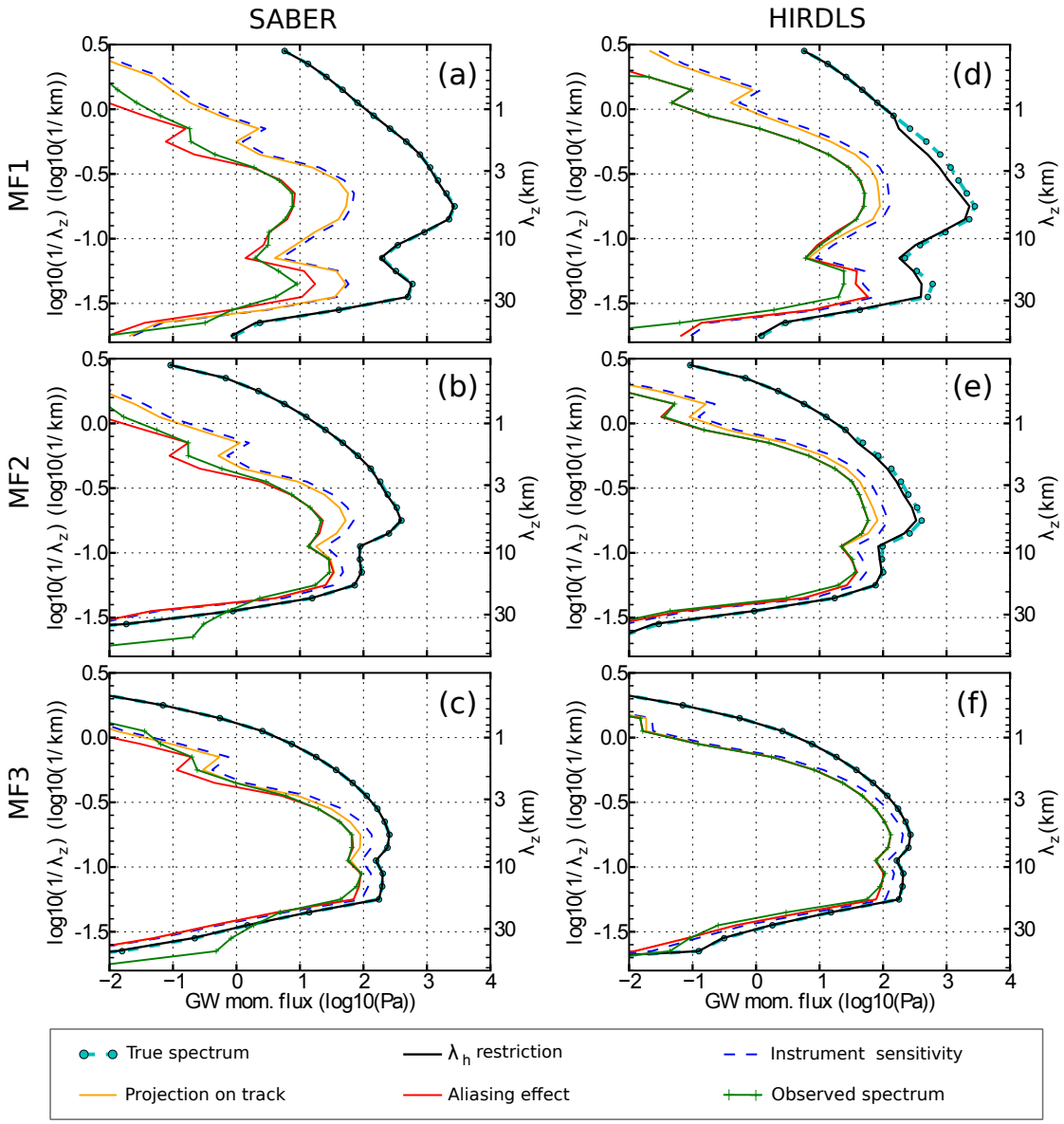

Figure 5.15: GWMF reduction during the observational filtering for **(a, d)** MF1, **(b, e)** MF2, and **(c, f)** MF3 with the observation geometry of SABER (left column) and HIRDLS (right column).

instrument sensitivity is the factor that reduces GWMF the most. This reduction can be seen by comparing the black line and the dashed blue line. The difference between these two lines is the largest difference between two adjacent lines in all panels. Moreover, this reduction was strongest for MF1, decreasing from MF1 to MF3 due to the increase in spatial scales. Again, this finding is in agreement with the change in spectra described above in this section.

In addition, the reduction in the case of HIRDLS was weaker than in the case of SABER, which is explained by the better sensitivity of the HIRDLS instrument. For example, after considering the instrument sensitivity of HIRDLS, GWMF of MF1 and MF2 (Fig. 5.15d and e) was about 2.1–2.2 (in the unit of base 10 logarithmic scale) while for SABER the value of GWMF dropped to about 1.8 (Fig. 5.15a and b). The contribution of short vertical-wavelength gravity waves from about 1 to about 3 km was also much larger in the case of HIRDLS than for SABER. For MF3 (Fig. 5.15c and f), the difference between these two observation geometries was lower than for MF1 and MF2, however, it is still recognizable even in the base 10 logarithmic scale.

The second strongest factor of GWMF reduction for SABER is aliasing, as can be seen by comparing the orange and the red lines, which are separated quite clearly from each other (except in the case of MF3). Again, the effect of aliasing decreases from MF1 to MF3 due to the increase in the spatial scales of the waves. Moreover, since the sampling distance of HIRDLS is shorter (70 km) than for SABER (185 km), less GWMF reduction by aliasing was found for HIRDLS.

The process of projecting the horizontal wavelength on the tangent-point track reduces GWMF less than instrument sensitivity and the aliasing effect in most cases; the exceptions are MF2 and MF3 for HIRDLS. Furthermore, the reduction by this factor was very similar for all spectra MF1, MF2 and MF3. This is due to the fact that the reduction is mainly induced by $|\cos(\psi - \gamma)|$, which does not depend on the spatial scale of the individual waves.

Minor redistribution of the spectra by the last three steps is shown by the difference between the red line and the green line with crosses. GWMF values at the spectral peak (at a vertical wavelength of about 30 km) were reduced by the additional correction. This can be seen clearly in Fig. 5.15a and d.

The step of λ_h restriction affected GWMF least. In the base 10 logarithmic scale, GWMF of true spectrum (the cyan dashed-dot line) and GWMF after considering λ_h restriction (the black solid line) were nearly the same in almost all panels.

In addition, cyan dashed-dot lines in Fig. 5.15 (true spectra) show that GWMF given by MF1 is the largest with a peak at about 3.5 (in the base 10 logarithmic scale). For MF2, this value is about 2.7 and for MF3 it is only about 2.4. The relative importance of these different spectra (MF1, MF2, MF3) in the whole GWMF spectrum is, however, still unknown and may be adjusted (e.g. by intermittency or efficiency factors) as the relative importance of various convective process in exciting gravity waves is still badly constrained.

More details about the reduction in GWMF during the observational filter are

presented in Table 5.1. Here, the total GWMF of the true spectrum is 100 %. The percentages of the remaining GWMF in other steps of the observational filter (instrument sensitivity, projection on track, aliasing effect and observed spectrum) are shown for all spectra.

Table 5.1: Percentages of remaining GWMF at main steps during the observational filter.

Spectrum	Step	SABER	HIRDLS
MF1	λ_h restriction	97.50	77.35
	instrument sensitivity	3.09	5.95
	projection on track	2.58	4.28
	aliasing	0.54	2.75
	observed spectrum	0.39	2.28
MF2	λ_h restriction	98.05	85.55
	instrument sensitivity	18.47	32.13
	projection on track	13.55	22.00
	aliasing	8.35	17.65
	observed spectrum	7.65	17.13
MF3	λ_h restriction	99.72	99.79
	instrument sensitivity	46.32	67.55
	projection on track	31.91	44.86
	aliasing	27.21	44.80
	observed spectrum	25.62	43.52

5.6 Conclusion

Prior publications have revealed the importance of the observational filter. Observational filters for different measurement techniques have been studied with a special focus on instrument visibility (e.g. *Alexander*, 1998; *Preusse et al.*, 2000) or careful consideration of observation geometry (e.g. *Wu and Eckermann*, 2008). In this study, for the first time, a comprehensive observational filter for infrared limb sounders with a high level of accuracy, which takes into account the visibility of waves to an infrared limb sounder as well as a sophisticated representation of the observation geometry, was developed.

The comprehensive observational filter contains four main processes: visibility filter, projection of the wavelength on the tangent-point track, aliasing effect and the calculation of the vertical observed wavelength. The first process comprises the following elements: the determination of the wavelength along the LOS, restriction of horizontal wavelength, application of the approximate sensitivity function (radiative transfer). The second process includes the determination of

the along-track wavelength and the calculation of the corresponding GWMF. The third process calculates the projection of waves towards much longer wavelengths by aliasing and the associated reduction of GWMF. The last step calculates the vertical wavelength which would be observed by the instrument and the corresponding GWMF.

The observation geometries of SABER and HIRDLS instruments were considered in our study. The results show that the most important processes, which have significant influences on the spectrum are: visibility filter (for both SABER and HIRDLS observation geometries), aliasing for SABER and projection on tangent-point track for HIRDLS.

We found that the vertical wavelength distribution was mainly affected by the "visibility filter" process, which relates to the radiative transfer and retrieval. This process reduced the short vertical-wavelength gravity waves, but did not largely change the shape of the vertical-wavelength spectrum. This is shown in Fig. 5.15. In this figure, all panels other than Fig. 5.15a show largely the same vertical wavelength distribution and in particular the peak at the same vertical wavelength as the original spectrum. For the horizontal structure, depending on the horizontal scale of the original spectrum, the observational filter can have stronger or weaker effects. For the original spectrum containing a short horizontal scale, in addition to the significant influence of the visibility filter, the spectrum was projected onto a longer horizontal wavelength interval which originally was not populated. In this case, a strong contribution to the spectrum was found until the Nyquist wavelength. In other words, a pronounced spectral peak, which stands out from other parts of the spectrum, was not generated. GWMF for this case (MF1) was largely reduced, possibly making such spectral contributions difficult to observe by infrared limb instruments. In the case of the long-horizontal-scale original spectrum, a pronounced peak was found. This finding suggests that a pronounced spectral peak is an indication of longer horizontal wavelengths in the original distribution.

We also found that during the filtering procedure, GWMF values of the spectrum containing very short horizontal wavelengths were reduced considerably. Moreover, due to the measurement geometry, altitude profiles are oblique, which results in a slight shift of the vertical wavelength. Simulating this effect we find that it does not affect the evaluation of profile pairs which need to match closely in their vertical wavelength (*Ern et al.*, 2011). For average spectra the overall effect is a negligible shift in the vertical wavelength distribution. In the current work, calculations were averaged for ascending and descending orbits because no significant differences between two of them were found (not shown). However, this depends on the particular observation geometry of each instrument. For another instrument, these differences might be significant and may have to be taken into account. In addition, the error caused by the instrument noise, as discussed below in Appendix C, is negligible and therefore is not considered in this observational filter.

The comprehensive observational filter is a powerful tool for comparing grav-

ity wave modeling with observations. This can be applied, as in our case, to the modeling of individual monochromatic waves by a single-wave gravity wave model. However, also numerical-model data can be spatially and spectrally decomposed. For instance, *Preusse et al.* (2014) used monochromatic fits in small volumes for comparing ECMWF data to observations. In their work, this observational filter was applied in order to increase the significance of the observation. Our main interest is the meaningful comparison between global observations and global gravity wave modeling with uncertainties smaller than those uncertainties assumed for global gravity wave observations alone (*Ern et al.*, 2004; *Geller et al.*, 2013). This shall result in improved understanding of the distributions of gravity waves in the real world and, hopefully, in realistic representations of gravity waves in GCMs employed for weather prediction and climate projection.

The example of the three parameter sets of convective gravity waves may be taken as a first example how such constraints of global gravity wave modeling may work. In the following chapter we will now use the tools prepared in chapters 3– 5 in order to infer improved estimates of the free parameters of the Yonsei model and, presumably, also improved spectral information for the real atmosphere.

Chapter 6

Tuning of a convective gravity wave source scheme based on satellite observations

6.1 Introduction

So far, in this dissertation, we have described and developed important tools for our research approach: the Yonsei CGWS scheme was described in chapter 3, the ray tracer was introduced in chapter 4, the comprehensive observational filter was developed in chapter 5. In this chapter, we employ these tools to study the physics of gravity waves. In particular, we determine the scales of convective gravity waves above convection and analyze the contribution of these waves to the dynamics of the atmosphere.

As mentioned in chapter 1 of this dissertation, the broad spectrum of convective gravity waves and the limitation of current observation techniques make the scales of convective gravity waves an open issue. In order to deal with this open issue, the spatial scale δx and the temporal scale δt of the diabatic forcing in the Yonsei CGWS scheme are free tunable parameters. These scales δx and δt cannot be determined from theory. Until recently, these scales were determined by assuming typical scales of clouds or convective systems. For instance, the primary scale set MF1 of the Yonsei CGWS scheme (*Song and Chun*, 2005) has $\delta x = 5$ km and $\delta t = 20$ min. These scales are selected based on mesoscale simulations conducted by *Song et al.* (2003). The primary scale set MF1 shows good agreement with gravity wave temperature variance (GWTV) from Microwave Limb Sounder (MLS) observations on board the Upper Atmosphere Research Satellite (*Choi et al.*, 2009) and with gravity wave momentum flux (GWMF) from three-dimensional mesoscale simulations (*Choi and Chun*, 2011). However, MF1 underestimates the GWTV observed by Atmospheric Infrared Sounder (AIRS) on board the Aqua satellite, and therefore an additional scale set MF2 ($\delta x = 25$ km,

δt = 60 min) was added (*Choi et al.*, 2012). GWTV given by the combination of MF1 and MF2 matches AIRS observations well in both horizontal distribution and magnitude. Nevertheless, this combination cannot explain the gravity wave spectrum observed by HIRDLS, which peaks at longer horizontal wavelength of about 600 km and vertical wavelength of about 10 km (*Ern and Preusse*, 2012). A possible reason is that MF1 and MF2 do not describe the presence of large-scale convective systems.

Recently, an increasing number of studies show evidence of the essential contribution of such large-scale convective systems to the global climatology. For example, in the paper of *Liu and Zipser* (2015), snapshots of precipitation systems (precipitation features (PFs)) observed by the precipitation radar on board the Global Precipitation Mission (GPM) were analyzed. The largest PFs are found with sizes greater than 100,000 km^2. *Liu and Zipser* (2015) reported that PFs with size greater than 48,756 km^2 contribute 28% of total global precipitation. For PFs with size larger than 10,000 km^2, this contribution is 54%.

In the work of *Khouider and Moncrieff* (2015) a modified version of a previously developed multicloud model is used for parameterizing mesoscale convective systems (MCSs). For the condition of a typical double African and equatorial jet shear flow, a linear analysis of this modification shows an additional new scale-selective instability with a maximum of approximately 400 km. In addition, in the work of *Kilpatrick and Xie* (2015), surface wind observations from the Advanced SCATterometer (ASCAT) are utilized to estimate the downdrafts of MCSs. These observations show the existence of MCSs with the scale of 100-300 km.

On one hand, the gravity wave spectra for MF1 and MF2 are not in agreement with the spectra observed by HIRDLS. On the other hand, there is an increasing number of recent studies showing the importance of large scale convective systems. This indicates a need of finding new larger scales δx and δt for the CGWS scheme, which can represent larger scale convective systems and correctly reproduce the spectrum observed by limb sounders. In this chapter, spatial scale δx and temporal scale δt are determined using a unique approach: not by forward estimation assuming typical scales of convective systems but by systematically variation and verification based on GWMF spectra observed from HIRDLS. For that purpose a wide range of spatial and temporal scale sets of the CGWS scheme is surveyed. Based on that survey and observations from HIRDLS, combinations of scale sets which fit best to the observed gravity wave spectrum are selected for January and July 2006. We also introduce an additional tuning parameter that controls the initial wave amplitude and therefore determines breaking levels. Details about this parameter will be explained later in Sec. 6.3.2. To analyze the contribution of convective gravity waves to the atmospheric dynamics, we compare zonal cross sections of observed and simulated GWMF and its vertical gradient. Again, the observational filter, which mimics the limitation of the instrument due to visibility effects and observation geometry is applied, and we can investigate the relation between absolute GWMF and GWD. Finally, we consider different source regions in global maps and discuss the interaction of gravity waves with the background

wind employing phase speed spectra of the zonal momentum flux.

We introduce the model setup in Sect. 6.2. The systematic survey of different scale sets for the CGWS scheme is shown in Sect. 6.3. Also in Sect. 6.3 zonal mean cross sections of GWMF, its vertical gradient, GW drag as well as global maps and GWMF spectrum in terms of zonal phase speed and latitude are presented. Finally, summary and discussion are given in Sect. 6.4.

6.2 Model setup

Simulations are performed for January and July 2006 using three main elements: First, convective gravity waves are generated using the CGWS scheme developed at Yonsei University (*Song and Chun*, 2005). The waves are propagated upward using the Gravity wave Regional Or Global RAy Tracer (GROGRAT) (*Marks and Eckermann*, 1995; *Eckermann and Marks*, 1997). Finally, a comprehensive observational filter for limb sounders (*Trinh et al.*, 2015) is applied for comparison with HIRDLS observations. The CGWS scheme is presented in chapter 3, the GROGRAT is introduced in chapter 4, and the comprehensive observational filter is described in chapter 5.

The CGWS scheme of *Song and Chun* (2005) describes the momentum flux of convective gravity waves at cloud top $\overline{M(c)}$ as a function of the phase speed of the waves (Eq.3.4, chapter 3). For computational efficiency in our implementation the momentum flux spectrum $\overline{M}(c)$ is not sampled continuously, but up to 10 maxima in the phase speed range from -100 m/s to 100 m/s are selected. These discrete values are used as input for the GW ray tracer, launched at the cloud top, and propagated away from the source. Shallow heating depths are not effective in exciting far-propagating gravity waves. Therefore, simulations are run only for heating depths equal or larger than 3.5 km. When coupling the GW ray tracer to the CGWS scheme, there is a further tuning potential to adapt the global distributions. We can reduce the launch amplitude by a factor of $1/\sqrt{\alpha}$ and simultaneously multiply the number of launched rays by a factor of α. In this way we retain the same total GWMF at launch but reduce the amplitude of the individual waves. This may be interpreted by spreading the same total GWMF over a larger area, i.e. assuming that the wave packet has a larger spatial extent. An important consequence is that by reducing the amplitude of the individual waves, saturation is reached at higher altitudes in the atmosphere. Furthermore, the latent heat input data are taken from three-hourly MERRA (modern-era retrospective analysis for research and applications) assimilated data. Detailed information about MERRA data as well as convective parameterization in MERRA are provided, for example, in *Rienecker et al.* (2011); *Kim and Alexander* (2013); *Wright and Fueglistaler* (2013).

The momentum flux of convective gravity waves supplied by the CGWS scheme is used for the GROGRAT simulations. In particular, the momentum flux is used to calculate wave amplitude following Eq. 2.11. The horizontal components of wave number are calculated based on the phase speed, spatial scale and temporal scale.

The intrinsic angular frequency is then calculated using intrinsic phase speed and horizontal wave number. Together with longitude, latitude coordinates and cloud top altitude, these data (wave amplitude, horizontal components of wave number and intrinsic angular frequency) provide a launch distribution for our ray tracing simulations. In addition, the MERRA data are also used to provide background wind and temperature fields for our GROGRAT simulations.

The comprehensive observational filter for HIRDLS, as described in details in chapter 5, is applied to output data from the ray tracing simulations. Model results after applying the observational filter can be compared directly to observations from HIRDLS.

6.3 Results

6.3.1 A systematic survey of the Yonsei CGWS scheme

The purpose of this systematic survey is to find sets of the free parameters δx and δt which describe spectra in terms of horizontal and vertical wave numbers observed by HIRDLS. These observed spectra for southern hemisphere summer 2006 (averaged over December 2005, January and February 2006) and for northern hemisphere summer 2006 (averaged over Jun, July and August 2006) are shown in Fig. 6.1.

The spectra presented in Fig. 6.1 are generated by binning absolute GWMF observed by HIRDLS according to horizontal and vertical wave numbers (k_h and m) using a technique similar to that of *Ern and Preusse* (2012). The base 10 logarithmic scale is employed here, i.e. the x axis shows $\widetilde{k}_\mathrm{h} = \log_{10}(1/\lambda_\mathrm{h})$ while the y axis shows $\widetilde{m} = \log_{10}(1/\lambda_z)$. Here λ_h and λ_z denote the horizontal and vertical wavelengths, respectively. The sizes of each bin in x and y direction are $\delta\widetilde{k}_\mathrm{h} = 0.1$ and $\delta\widetilde{m} = 0.1$.

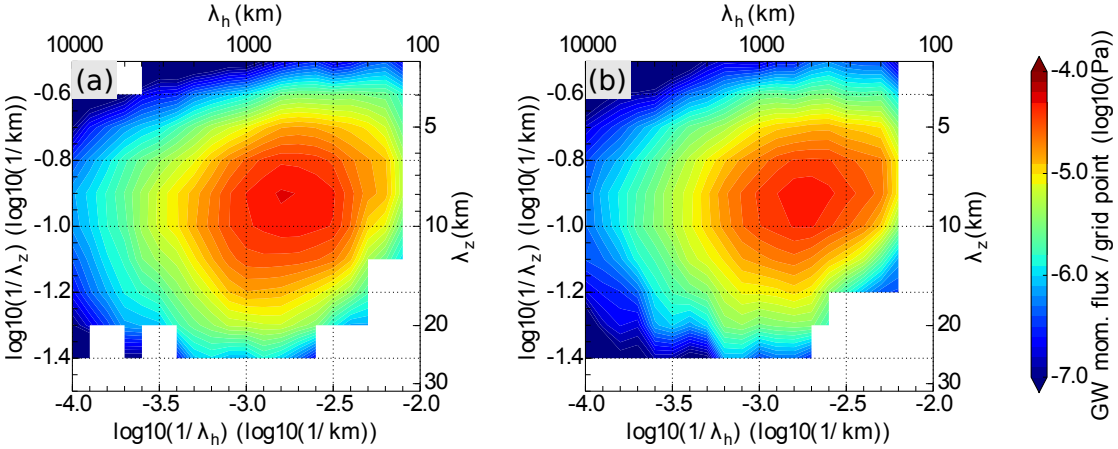

Figure 6.1: Spectra observed by HIRDLS for (a) southern hemisphere summer 2006 and (b) northern hemisphere summer 2006. For details see text.

It is noteworthy that spectra in Fig. 6.1 are averaged over regions, which are defined as deep convection regions in *Ern and Preusse* (2012). These regions are shown in Fig. 6.2. For the northern hemisphere and June, July, August, three regions of deep convection are indicated by three red rectangles. For the southern hemisphere and December, January, February, three regions of deep convection are indicated by three green rectangles. The longitude-latitude coordinates of these regions are listed in Table 6.1.

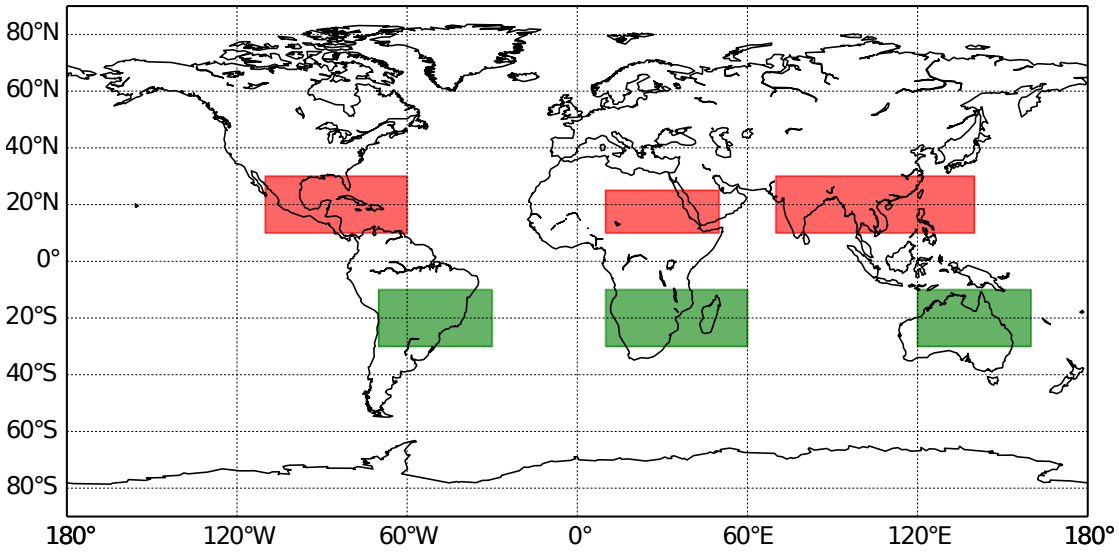

Figure 6.2: Regions of deep convection. For the northern hemisphere, three regions of deep convection are demonstrated by three red rectangles. For the southern hemisphere, three regions of deep convection are indicated by three green rectangles.

Table 6.1: Regions of deep convection during 2006

	Northern Hemisphere			Southern Hemisphere		
	region 1	region 2	region 3	region 1	region 2	region 3
latitude 1 [deg]	10	10	10	-30	-30	-30
latitude 2 [deg]	30	25	30	-10	-10	-10
longitude 1 [deg]	-110	10	70	-70	10	120
longitude 2 [deg]	-60	50	140	-30	60	160

It is interesting that the observed spectrum for southern hemisphere summer (Fig. 6.1a) is somewhat different from the one for northern hemisphere summer (Fig. 6.1b) in shape as well as location of the spectral peak. The exact reason for these differences are unknown but several reasons are likely candidates for these difference. For instance, differences can caused by the observational filter, or by different background wind filtering in different hemispheres. Furthermore,

Table 6.2: Surveyed and selected spatial and time scales (δx, δt) as well as intermittency factor (ζ) for the Yonsei CGWS scheme.

Scales used for surveying		Selected scales for January			Selected scales for July		
δx (km)	δt (min)	δx (km)	δt (min)	ζ	δx (km)	δt (min)	ζ
4	**10**	80	240	1.0	40	80	1.0
8	20	120	120	0.4	160	100	1.0
12	**40**	200	150	0.4	250	240	1.0
25	80	250	360	0.7			
40	**120**						
80	240						
120	360						
250	**720**						
400							
800							
1200							

differences in convective source characteristics in two hemispheres can also play a role.

For the systematic survey of the spatial and temporal scales we tested the whole set of combinations given by the surveyed scales in the first two columns in Table 6.2. These scales are selected on one hand to cover the whole potential ranges, on the other hand with the appropriate step width to optimize computational efficiency. An appropriate step width also helps to distinguish the changes between the spectra for different parameter settings. Figures 6.3 and 6.4 provide overviews of the results for January and July 2006, respectively, by a reduced set of filtered, simulated GW spectra. In Fig. 6.3 and 6.4, for a better visualization, only spectra corresponding to the values given in bold in Table 6.2 are shown.

Spectra in Fig. 6.3 and Fig. 6.4 are shown for the altitude of 25 km and averaged over the same regions defined as deep convection regions (c.f. Fig. 6.2 and Table 6.1). The spectra presented in Fig. 6.3 and 6.4 are generated by binning absolute GWMF from ray-tracing calculation according to horizontal and vertical wave numbers (k_{h} and m) using the same technique as used for observed spectra in Fig. 6.1.

In Fig. 6.3 and Fig. 6.4 the color shading represents the GWMF spectra simulated by the Yonsei CGWS, propagated to observation altitude by GROGRAT and filtered according to the comprehensive observational filter. The dashed contour lines indicate the spectrum observed by HIRDLS for regions of deep convection. For these simulated spectra, spatial scale δx increases from the right column to the left column in Fig. 6.3 and Fig. 6.4. The temporal scale δt increases from the bottom to the top in Fig. 6.3 and Fig. 6.4. As shown by Fig. 6.3 and Fig. 6.4, the horizontal wavelength of the spectral peak increases as the spatial scale δx of the convective system increases. Due to the resonance effect formulated in the

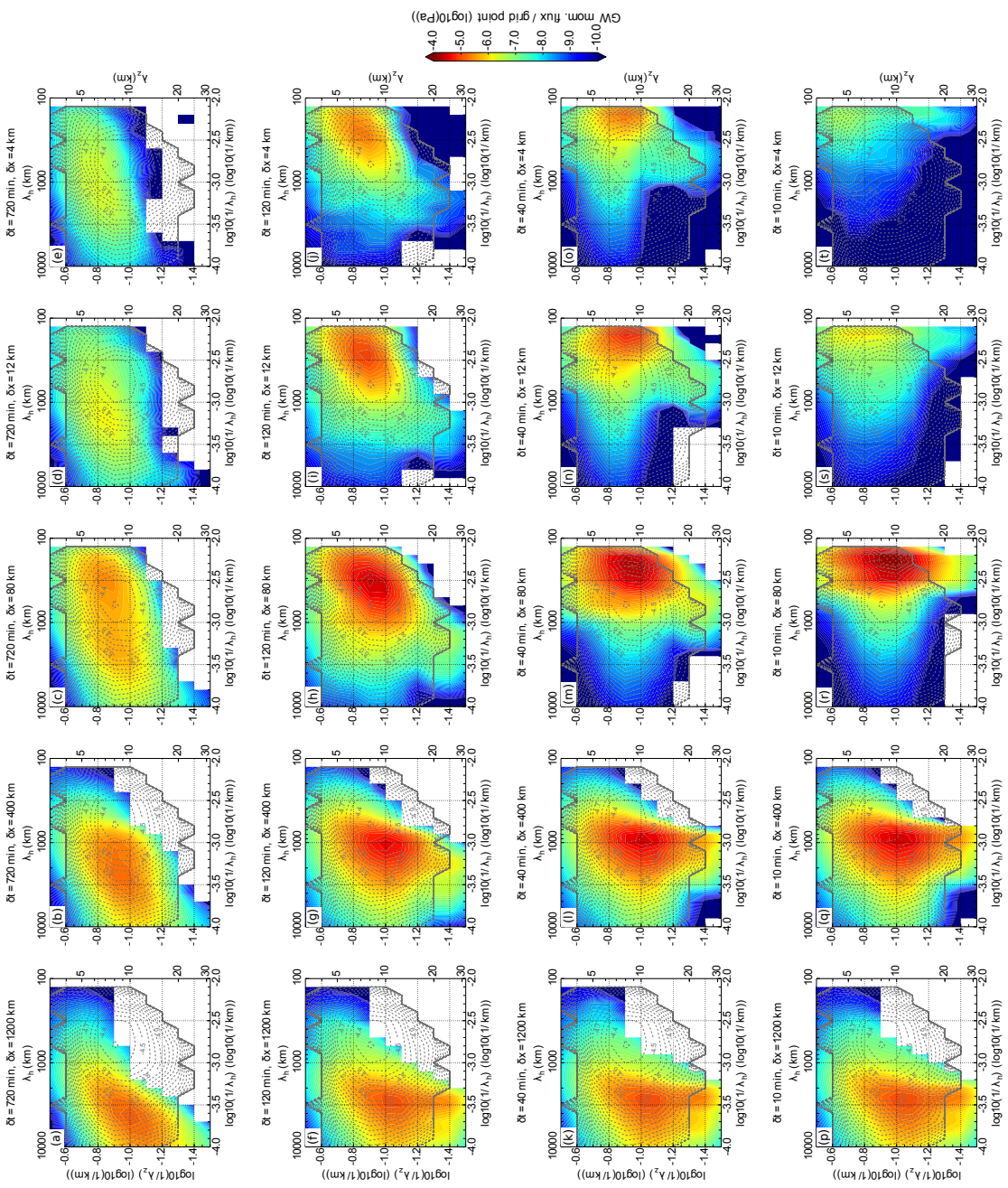

Figure 6.3: A systematic survey of the CGWS scheme depending on different spatial and temporal scales of the convective system for January 2006. The color code shows the simulated GWMF spectra of CGWs generated by the Yonsei CGWS scheme, propagated upward to 25 km altitude using GROGRAT and filtered according to the observational filter. The dashed contour lines show the spectrum for regions of deep convection observed by HIRDLS.

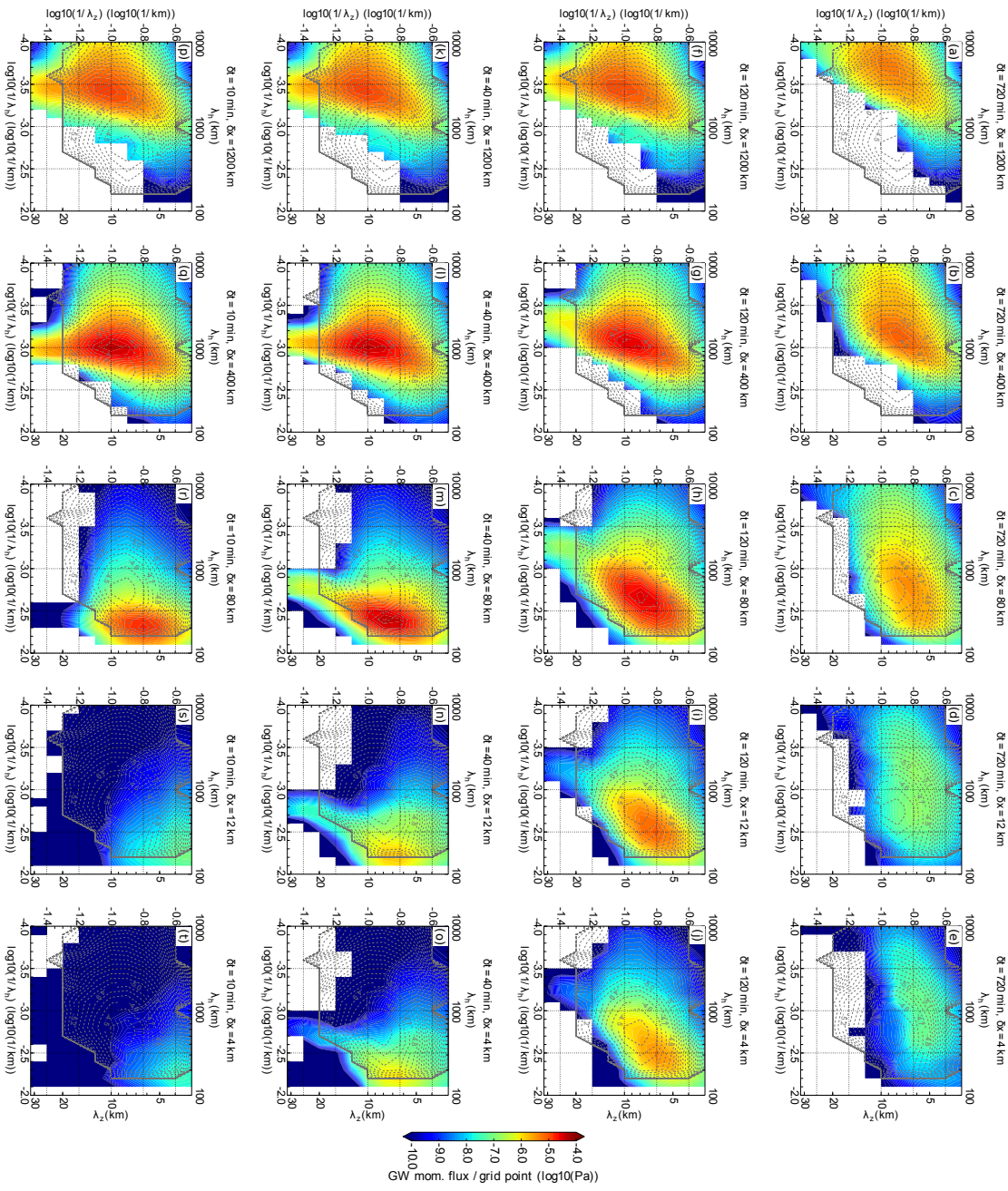

Figure 6.4: Same as Fig. 6.3, but for July 2006

CGWS scheme, the phase speed and hence the vertical wavelength associated with the spectral peak depend only weakly on the temporal scale δt of the convective system. It can also be seen in Fig. 6.3 and Fig. 6.4 that gravity waves forced by convective systems with very short spatial and temporal scales (e.g. Fig. 6.3n, o, s, t and Fig. 6.4n, o, s, t) are strongly suppressed in HIRDLS observations due to the observational effect, as shown also in chapter 5.

Some of the spectra (e.g. Fig. 6.3g, h, l and Fig. 6.4g, h, l) show a spectral peak, which locates closely to the observed spectral peak. To complement the survey grid with a parameter set providing a close match with the observed spectral peak, we calculated additional spectra with $\delta x = 200$ km and $\delta t = 150$ min for January 2006 and $\delta x = 160$ km and $\delta t = 100$ min for July 2006.

As mentioned in the introduction of this chapter, studies of large-scale convective system (*Liu and Zipser*, 2015; *Khouider and Moncrieff*, 2015; *Kilpatrick and Xie*, 2015) indicate that CGW forcing is a multi-scale problem with major contributions by a few dominant scales. For this reason we combine several spectra from the systematic survey in order to obtain a best fit to the observed spectra. Spectra are super-imposed by minimizing the following function:

$$\eta = M_{obs} - \sum_i \zeta_i M_i / \sum_i \zeta_i \tag{6.1}$$

where M_i is a single spectrum from the systematic survey, ζ_i is the respective intermittency factor, and M_{obs} is the observed GWMF spectrum. Combinations of M_i with respective ζ_i, which give the best fit to the observed spectrum, are chosen from minimization of η. For computational efficiency, we limit the maximum number of combined spectra to 4 and only largest ζ_i are selected. The selected spatial scale δx, temporal scale δt as well as corresponding intermittency factor ζ are shown in Table 6.2 for January and July 2006. Figure 6.5 shows the resulting combined spectra for January (left column) and July (right column), without observational filter (upper row) and after application of the observational filter (lower row). Again, the color code indicates the simulation results and the dashed lines indicate the observations.

As shown by Fig. 6.5c and Fig. 6.5d, the filtered simulated spectrum matches the observed spectrum very well in both shape and location of the spectral peak for both conditions of January and July 2006. As mentioned above in this section, Fig. 6.3 and Fig. 6.4 show that the horizontal wavelength of the spectral peak increases as the spatial scale δx of the convective system increases. However, the vertical wavelength of the spectral peak depends only slightly on the temporal scale δt due to both resonance effect and observational filter effects. Therefore, it is non-trivial that the vertical wavelength of the spectral peak of the filtered simulated spectrum matches the observed respective one. The match of filtered simulated spectrum and observed spectrum therefore indicates the validation of the CGWS scheme.

Comparison of Fig. 6.5a, b and Fig. 6.5c, d shows that the observational filter not only reduces the magnitude, but also significantly changes the shape of

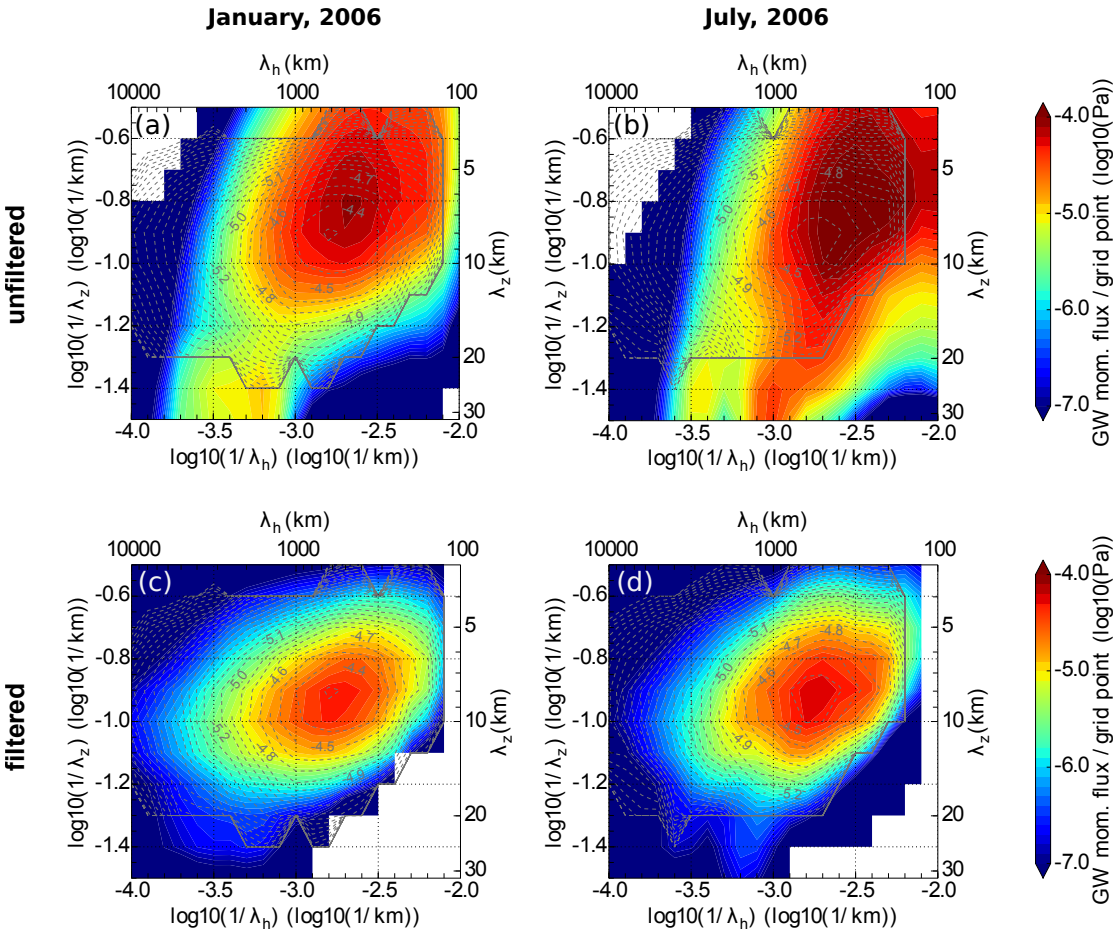

Figure 6.5: Unfiltered combined gravity wave spectra of selected scale sets for (a) January 2006 and (b) July 2006 and filtered combined spectra of selected scale sets for (c) January 2006 and (d) July 2006. All spectra are shown for the altitude level of 25 km. The color code represents combined filtered simulated spectra; the dashed contour lines represent spectra observed by HIRDLS for regions of deep convection.

the spectrum. In particular, contributions of short horizontal wavelength waves as well as short vertical wavelength waves strongly decrease and are also partly shifted to longer horizontal wavelengths. Moreover, the unfiltered spectrum for July 2006 contains more short vertical and horizontal wavelength waves than the unfiltered spectrum for January 2006. Therefore, the unfiltered spectrum for July is influenced much more stronger by the observational filter than the unfiltered spectrum for January.

The selected scale sets for January and July 2006 are somewhat different (cf. Table 6.2), which may related to slight difference in the observed spectrum for different hemispheres as mentioned while describing Fig. 6.1 above. These differences, however, are minor and one set of scales could be used in case simplification is necessary, for instance for investigating the diurnal cycle of tropical and sub-

tropical waves.

The selected scale sets quantitatively agree well with those found in the convective system studies, which were mentioned in the introduction of this chapter. For the considered regions of deep convection, convectively generated gravity waves are dominant and tuning convective scales based on these regions is clearly possible. For other regions, other sources such as orography, windshear, imbalanced jets can be more dominant. Since we cannot isolate convective gravity waves based on observations in these regions, the current tuning is less meaningful or even not possible there. Global runs in this study are performed by adopting parameter choices determined by deep convection regions for the entire respective hemisphere. This is one of the limitations of this approach.

Furthermore, from results of the systematic survey (Fig. 6.3, Fig. 6.4) and observed spectra (Fig. 6.1) it can be seen that some scale sets with short temporal scale as well as horizontal scale of several ten kilometer (for instance $\delta t = 10\,\mathrm{min}$ and $\delta x = 80\,\mathrm{km}$ in Fig. 6.3) can appear with only a very low intermittency factor in any combination, which reproduces the observed spectrum. This seems to indicate a gap between the large scales founded in this thesis and the short scales used in previous studies.

6.3.2 Zonal average of convective GWMF and its vertical gradients

In section 6.3.1 we have determined the spatial scales of convective gravity waves. In this section we use those results to investigate the interaction of convective gravity waves with the atmospheric background wind. In particular, zonal averages of GWMF and its vertical gradient are calculated and shown in Fig. 6.6 for January and in Fig. 6.7 for July 2006. In all panels of Fig. 6.6 and Fig. 6.7, contour lines indicate zonal average zonal wind for the respective month. In order to generate zonal averages of absolute GWMF, the values from ray-tracing calculation are first binned onto a three-dimensional grid with bin sizes of 10° in longitude, 2° in latitude and 1 km in altitude. Results are normalized by total number of rays and the zonal averages are calculated.

Figure 6.6a and Figure 6.7a show simulated absolute GWMF without observational filter effects for January and July, respectively. Both Fig. 6.6a and Fig. 6.7a show a main maximum of GWMF in the summer subtropics spreading from the equator to about 25 ° S (Fig. 6.6a) or to about 25 ° N (Fig. 6.7a), which is consistent with the latitude band of deep convection (e.g. *Jiang et al.*, 2004a). The width and magnitude of this maximum decreases with altitude due to wave dissipation, wave breaking and wind filtering. For January, this decrease is significant and strongly related to wind filtering at the altitude of about 20 km, where GWs encounter a wind reversal.

Figure 6.6b and Figure 6.7b show filtered, simulated absolute GWMF for January and July, respectively. Due to the observational filter the magnitude of GWMF is reduced by about half an order of magnitude. Moreover, for January, stronger

GWMF reduction is found at altitudes below and around the tropopause.

Observed GWMF from HIRDLS for January and July are shown in Fig. 6.6c and Fig. 6.7c, respectively. For comparing filtered, simulated GWMF (Fig. 6.6b, Fig. 6.7b) with observed GWMF (Fig. 6.6c, Fig. 6.7c) it is very important to keep in mind that the model results show GWMF only from convective sources, while observations from HIRDLS contain GWMF from a variety of sources. As convection is believed to dominate the summer subtropics, we expect model and observations to match at low latitudes while at mid and high latitudes HIRDLS observations indicate an additional enhancement due to other sources. Accordingly, the simulated maximum in Fig. 6.6b matches the maximum in Fig. 6.6c in the summer subtropics, where CGWs dominate. The same agreement can be seen by comparing Fig. 6.7b and Fig. 6.7c. In particular, centers of these maxima are both located at about 15 °S for austral summer (Fig. 6.6b, c) or at about 15 °N for boreal summer (Fig. 6.7b, c). Also, the structure of these maxima in the tropics from about 20 km to about 40 km altitude in both simulations and observations follow the contour line of the wind reversal. However, the magnitude of the simulated maximum is somewhat lower than the observed one. Moreover, the width of the simulated maximum is slightly narrower than the observed one. These differences can be interpreted by a lack of contributions from other sources than convection. The observed maximum at high winter latitudes is due to other sources (e.g. orography, jets and fronts) and cannot be simulated by our setup.

Different measures of the vertical gradient:

Vertical cross sections of the absolute value of GWMF span several orders of magnitude and accordingly a logarithmic color scale is used, which emphasizes the major features while the precise vertical structure is difficult to discern. On the other hand, for discussing the interaction of gravity waves with the background flow it is important to consider the exerted zonal mean drag in the zonal direction:

$$X = -\langle 1/\rho \cdot d/dz(F_x)\rangle \tag{6.2}$$

where ρ is atmospheric density, F_x is the zonal GWMF and $\langle\ \rangle$ denotes the zonal mean. Unfortunately measurements can provide only a vertical gradient P:

$$P = -\langle 1/\rho \cdot d/dz(|\Omega(\vec{F})|)\rangle \tag{6.3}$$

where $\vec{F}$ is the horizontal vector of GWMF, Ω denotes the observational filter and $|\ |$ denotes absolute values in 2D, i.e. here $\sqrt{\Omega(F_x)^2 + \Omega(F_y)^2}$, where F_y is the meridional GWMF. In fact, differences between X and P can be significant: waves dissipating, because they reach saturation amplitudes, but propagating in opposite directions cancel each other when calculating X but contribute both positively in calculating P. Moreover, waves propagating conservatively but moving out of the observational filter Ω will enhance P but they do not contribute to the real drag X. Therefore, P may exhibit different patterns from X. However, P still emphasizes the vertical gradient and in this respect it is the closest proxy for X we

can gain from measurements. The model setup in this thesis allows us to calculate both X and P and hence to compare P to the observations. Furthermore, we can study the various contributions of dissipation, drag and observational filter by calculating different combinations of the vertical derivative, the observational filter and the absolute value.

Physical interpretation:

Figure 6.6d and Figure 6.7d show the simulated zonal drag X for January and July 2006, respectively. In the tropics (15 ° S-15 ° N) drag is exerted in regions of vertical wind shear. Positive drag is found for positive shear and negative drag for negative shear as expected for the driving of the QBO. Moreover, the magnitude of the simulated zonal drag X is comparable to the "missing drag" deduced in *Ern et al.* (2014)[1]. In addition, for January 2006, Fig. 6.6d shows a particularly noteworthy U-shaped structure around 30 km.

Figure 6.6e and Figure 6.7e show another type of vertical gradient of GWMF, which is calculated as follows:

$$Q = -\langle 1/\rho \cdot |\Omega(d/dz(\vec{F}))|\rangle \tag{6.4}$$

The vertical gradient Q considers the dissipation caused by those waves only which are visible to the instrument. In Fig. 6.6e the U-shaped structure is much less pronounced in comparison with Fig. 6.6d. However, in Fig. 6.6e, a strong dissipation can be seen for a wind maximum at 40-45 km altitude and 20 ° S, which is located above the strongest sources although the wind gradient is not significant. Similar strong dissipation can be seen at the same altitude range at about 20 ° N in Fig. 6.7e.

Figure 6.6f and Figure 6.7f show simulated P (the quantity that observed "potential drag" should be compared to). For January, both the U-shaped structure at around 30 km and the maximum above 40 km are visible and correspond well to similar structures in the observed vertical gradient from HIRDLS (Fig. 6.6g). In Fig. 6.6d and Fig. 6.6f, the U-shaped structure is more pronounced than in Fig. 6.6e. A possible reason for this difference is: In the U-shaped structure we presumably see many waves of low horizontal phase speeds which are refracted to very short vertical wavelengths and therefore are not visible to the satellite instrument. As the saturation is reached only when the vertical wavelength is even shorter than the short edge of the visibility filter, these waves when propagating from below first do not pass the observational filter any longer (absence in Fig. 6.6f at 30 km altitude and 15 ° N) but dissipate almost immediately above (Fig. 6.6d at 30-33 km and 15 ° N). The dissipation itself is then not visible to the satellite (low values of vertical gradient at 30-33 km and 15 ° N in Fig. 6.6e). It should be

[1] In *Ern et al.* (2014), in order to estimate the QBO driving by gravity waves, the transformed Eulerian mean zonal momentum equation (*Andrews et al.*, 1987) was utilized. All terms of this equation except the drag due to gravity waves were calculated using ERA-Interim assimilated data (*Dee et al.*, 2011). The drag due to gravity waves is then deduced based on this equation and other calculated terms and is referred to as the "missing drag".

mentioned that a related shift in the altitude of observed GWD has been discussed in *Ern et al.* (2014).

The GWD maximum at 40 to 45 km altitude is seen in Fig. 6.6e, 6.6f and 6.6g, but not in Fig. 6.6d. This is likely caused by longer vertical wavelength waves having gained saturation amplitude but not causing much net GW drag as different propagation directions contribute. In July we find closer correspondence between P and X (again with some altitude shift). The structures of P and X also agree quite well with the structures of observed vertical gradient shown in Fig. 6.7g. Similar to GWMF, the observed vertical gradients in Fig. 6.6g and Fig. 6.7g are dominated, in particular at higher latitudes, by signatures from sources other than convection. It should also be noted that a 10 km vertical analysis interval is used for HIRDLS data analysis smoothing the results vertically, which could also lead to some differences between model results and observations.

As we mentioned in Sect. 6.2, there is a further tuning potential by reducing the launch amplitude by a factor of $1/\sqrt{\alpha}$ and simultaneously multiply the number of launched rays by a factor of α. In this work, α was chosen to be 5. The choice of α does not affect the total GWMF at launch but can affect GWMF at higher altitudes and shift the saturation level to higher altitudes. Therefore, depending on the choice of α the structure and magnitude of GWMF, zonal drag, simulated P, and simulated Q may be altered. A comparison of vertical cross sections of GWMF and its vertical gradients for $\alpha = 1$ (no tuning of wave amplitude at launched level) and $\alpha = 5$ is presented in Appendix E. With a more detailed consideration of the momentum balance this tuning factor may need to be revisited.

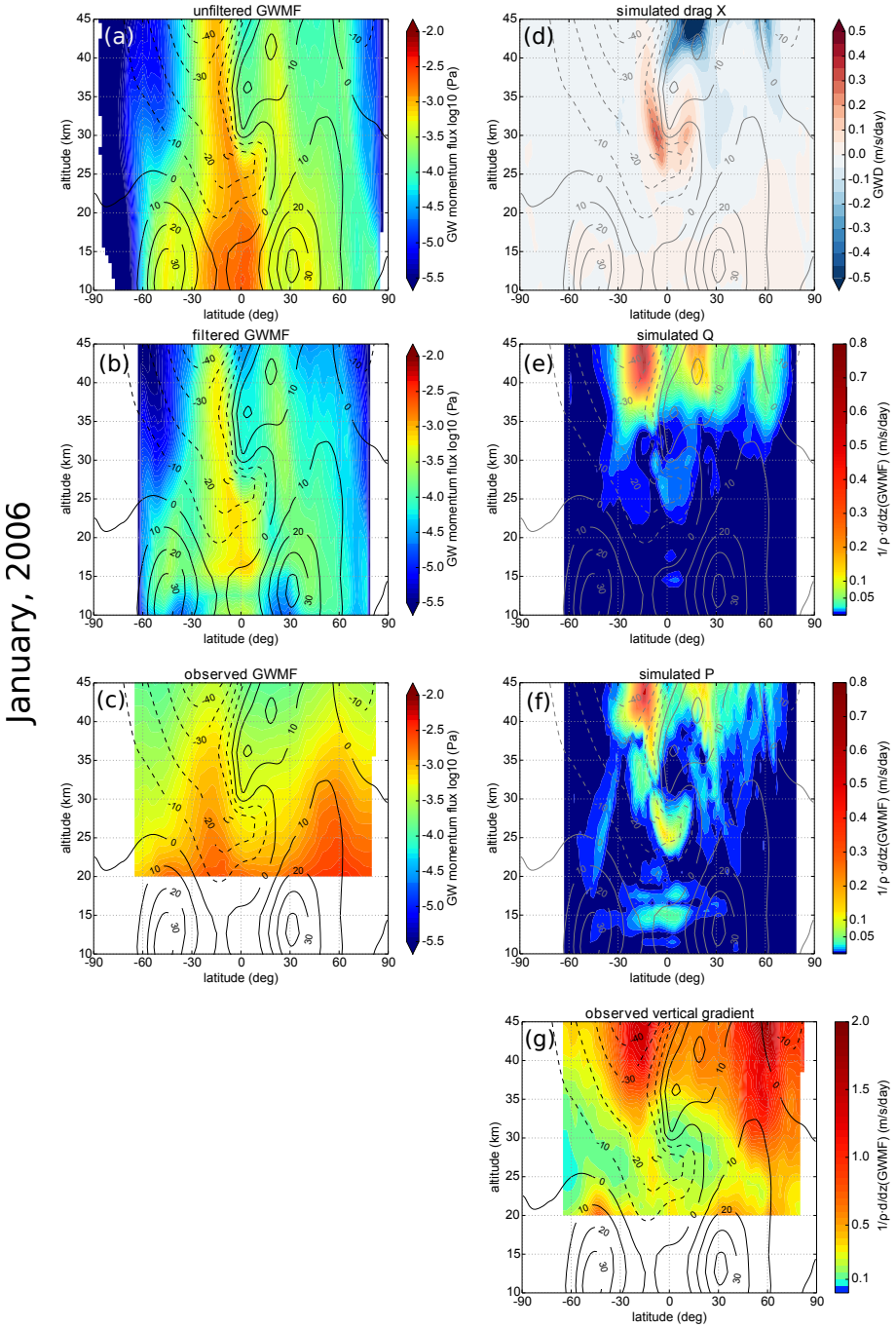

Figure 6.6: Comparison of simulated GWMF and its vertical gradients with observations from HIRDLS for January 2006. Panel (a) shows simulated unfiltered absolute GWMF, panel (b) shows simulated filtered absolute GWMF, and panel (c) shows absolute GWMF observed by HIRDLS. Simulated zonal GW drag is given in panel (d), simulated vertical gradient Q is given in panel (e) and simulated vertical gradient P is given in panel (f). Panel (g) shows the observed vertical gradient of absolute GWMF from HIRDLS. For details see text.

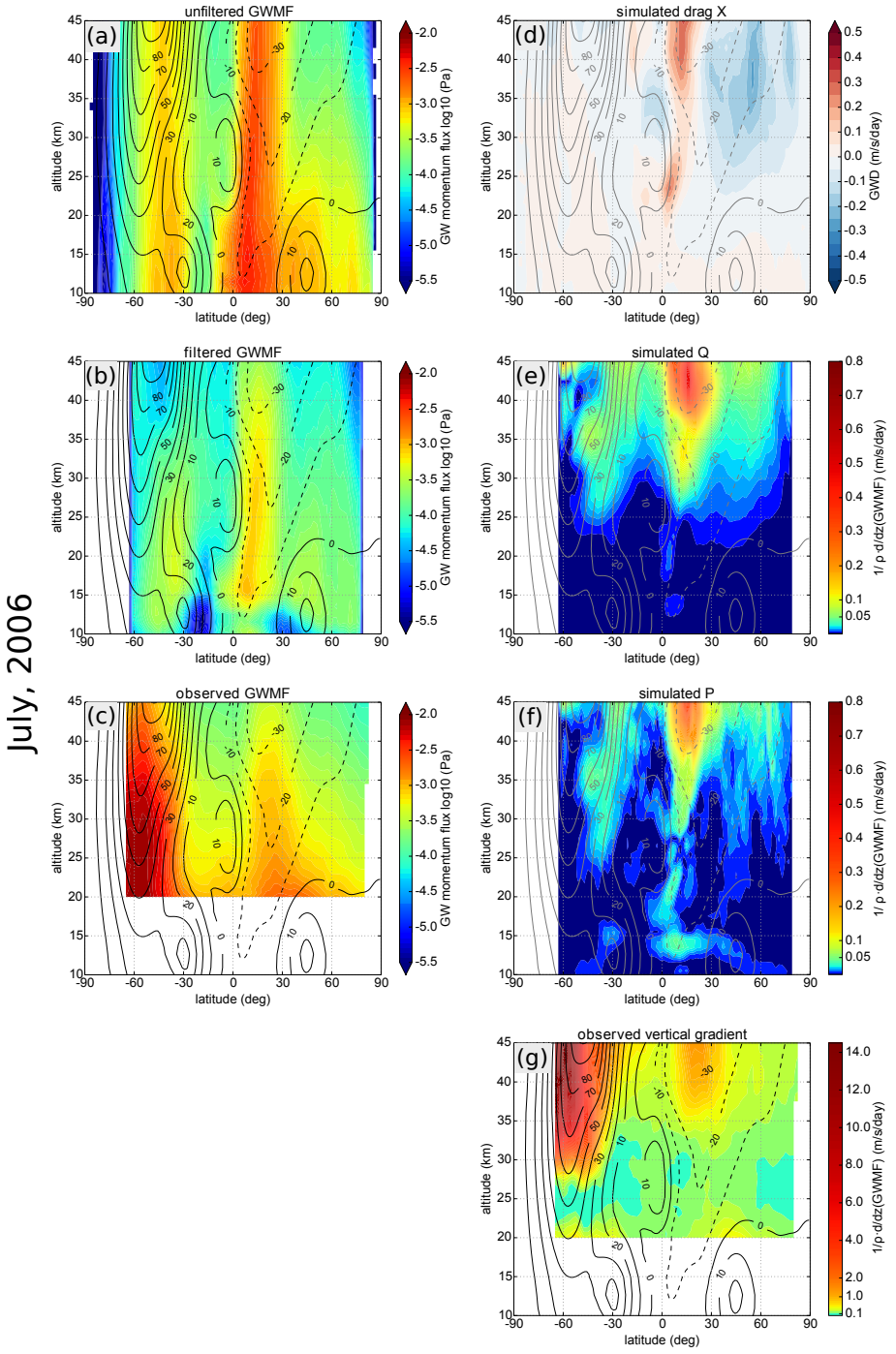

Figure 6.7: Same as Fig. 6.6, but for July 2006.

6.3.3 Horizontal distribution of GWMF and phase speed spectrum

In this section we show horizontal distributions of simulated convective GWMF as well as spectra of GWMF in terms of zonal phase speed and latitude. In Fig. 6.8 and Fig. 6.9 data for January, and in Fig. 6.10 and Fig. 6.11 data for July are shown. Figures 6.8 and 6.10 give values for 25 km altitude, while Fig. 6.9 and 6.11 give values for 40 km altitude. In each of these figures, the left column contains global maps of GWMF: panel (a) the unfiltered, simulated GWMF, panel (c) the filtered, simulated GWMF and panel (e) the observed GWMF. The right column shows zonal GWMF as a function of zonal phase speed and latitude (hereafter referred to as phase speed spectra) in bins of 4 m/s and 4 °. For both maps and spectra the color scales indicate the base 10 logarithm of GWMF. As for phase speed spectra GWMF with negative (westward) phase velocities is negative (westward GWMF), these values were multiplied by -1 before applying the logarithm. HIRDLS does not provide a propagation direction and accordingly phase speed cannot be deduced from the measurements.

In the global maps (panels (a), (c), (e)), the rectangle indicated by the magenta dashed line shows the low latitude area, where convection is assumed to dominate for the respective season. Blank areas in panels (a), (c), (e) refer to values of GWMF, which are out of the shown value range (< -5.0 ($\log_{10}$ Pa) or > -1.0 ($\log_{10}$ Pa)). In panels (b), (d), the gray thick line indicates the zonal mean of zonal wind at the considered altitude level, the magenta dashed line shows the maximum of the zonal mean zonal wind in the altitude range from cloud top to the considered altitude level, and the magenta dotted line shows the minimum of the zonal mean zonal wind in the same altitude range.

For January 2006, at 25 km altitude, high values of unfiltered GMWF are found over central south America, south Africa, a strip spreading from Madagascar to Indonesia, Indonesia and north Australia, and a strip over the Pacific ocean at around 20° S latitude spreading from 180° W to 120° W (Fig. 6.8a). After applying the observational filter, GWMF decreases about half an order of magnitude (Fig. 6.8c). In addition, the observational filter also changes the distribution of GWMF at some locations. For example, over Indonesia, a band of high GWMF at about 10° N spreading from the Philippines to 180° E, is stronger filtered out in comparison with the band of high GWMF at about 0-10° S. Figure 6.8e shows observed GWMF from HIRDLS. Comparison of filtered GWMF (Fig. 6.8c) and observed GWMF (Fig. 6.8e) shows a quite good agreement in location of GWMF peaks in the summer subtropics. In particular, the maxima over central south America, south Africa, Indonesia and north Australia are reproduced. The magnitude of filtered GWMF is lower in comparison with observed GWMF which, as discussed above, can be explained by a lack of other sources than convection.

The phase speed spectrum for January 2006 at 25 km altitude (Fig. 6.8b) shows a major peak in the tropics with eastward phase speed from several m/s to about 25 m/s, with the center of the peak at about 5 m/s. At higher phase speeds

(beyond 40-50 m/s), two minor peaks in both eastward and westward directions are found. The GWMF associated with these minor peaks is about 2 orders of magnitude lower in comparison with the main peak. In mid and high latitude regions, high GWMF values are mainly associated with westward phase speeds varying from several m/s to about 40 m/s. Figure 6.8d shows the phase speed spectrum of filtered GWMF. The observational filter in this case reduces GWMF magnitude but almost does not impact the structure of the spectrum.

The effect of wind filtering can also be found in the phase speed spectrum. This effect occurs when a wave encounters the critical level, i.e. where the background wind equals the phase speed of the wave. In this case, the intrinsic phase speed and thus the vertical wavelength approach zero causing saturation and the release of GWMF. In Fig. 6.8b and 6.8d, GWMF are mainly found in the areas where the gravity wave phase speed is larger than the maximum zonal mean zonal wind (magenta dashed line) or lower than the minimum zonal mean zonal wind (magenta dotted line). A small amount of GWMF still can be found in between these two lines because: a) these lines only indicate the zonal mean of the zonal wind and thus waves may be able to propagate due to local variations and b) many waves also have a meridional component. Still the findings indicate that filtering is dominated by the variation of the zonal wind.

For January 2006 at 40 km altitude, the horizontal band of high GWMF values in the summer subtropics becomes narrower (more concentrated around latitude of ∼15°S) and is slightly shifted poleward. The magnitude of GWMF decreases strongly with altitude, as can be seen by comparing Fig. 6.8a and Fig. 6.9a. This is also in agreement with the vertical cross section of absolute GWMF shown in Fig. 6.6a. A wind reversal at about 30 km altitude is likely the main reason for the reduced GWMF values close to the equator, or in other words, for narrowing the horizontal band of high GWMF values. The location of simulated and observed GWMF hot spots agrees well (cf. Fig. 6.9a, b, c). At 40 km altitude the measurements indicate that GWMF in the hot-spot regions, where the model results suggest deep convection as the dominant source, is enhanced about one order of magnitude compared to the background regions. This is a stronger enhancement than at 25 km altitude (about half an order of magnitude) and indicates that the non-convective background is relatively less important at 40 km.

Also the phase speed spectrum changes with altitude: the main peak of the spectrum at 40 km does not stretch over the equator as for 25 km but is limited only to the southern hemisphere. This change is according to the change of the maximum zonal wind, which is indicated by the magenta dashed line. This line surrounds the main peak in the tropics. Another major difference of the phase speed spectrum at 40 km in comparison with the one at 25 km is the absence of the peak at mid and high latitudes in the southern hemisphere at westward phase speeds (20°S to 40°S). This absence is again likely related to wind filtering as indicated by the magenta dotted lines for the difference in minimum zonal winds in Fig. 6.8b, d and Fig. 6.9b, d, respectively.

For July 2006 at 25 km altitude, unfiltered GWMF (Fig. 6.10a) shows high

values over the Caribbean sea, central Africa and the Asian Monsoon region. Figure 6.10c shows filtered GWMF with the magnitude reduced significantly due to the observational filter. Comparison of filtered GWMF (Fig. 6.10c) and observed GWMF (Fig. 6.10e) shows a quite good agreement in locations of GMWF maxima. As seen before in the zonal means, however, the observed GWMF maxima are wider, i.e. extend further to the north. In addition, the model results also show GW excitation following the warm water currents of the Gulf Stream and the Kuroshio.

Similar to January 2006 at 25 km altitude, the phase speed spectra (Fig.6.10b and Fig. 6.10d) show a main peak in the summer subtropics with eastward phase speeds from several m/s to ∼30 m/s. Moreover, two secondary peaks in the summer subtropics at high phase speeds (larger than 40-50 m/s), which are ∼2.5 order of magnitude smaller in comparison with the main peak, are also found. The observational filter decreases the GWMF magnitude but almost does not alter the structure of the phase speed spectrum. This can be seen by comparing the spectrum structure shown Fig.6.10b and Fig. 6.10d.

Similar to the January case, the magnitude of GWMF decreases with altitude (Fig. 6.11). This decrease, however, is weaker than in January. In particular, there is no strong reduction of GWMF in the tropics, which narrows the region of strong GWMF between 25 km and 40 km, such as for January.

Concerning the phase speed spectrum at 40 km altitude (Fig. 6.11b, d), a major difference in comparison with the spectrum at 25 km is much lower GWMF at mid and high latitudes in the northern hemisphere (from 40°N - 80°N). This can be seen by comparing Fig. 6.10b, d with Fig. 6.11b, d. This reduction is likely related to the change of minimum zonal wind at this latitude range, which can be seen by comparing minimum zonal mean zonal wind in Fig. 6.10b, d and Fig. 6.11b, d, respectively.

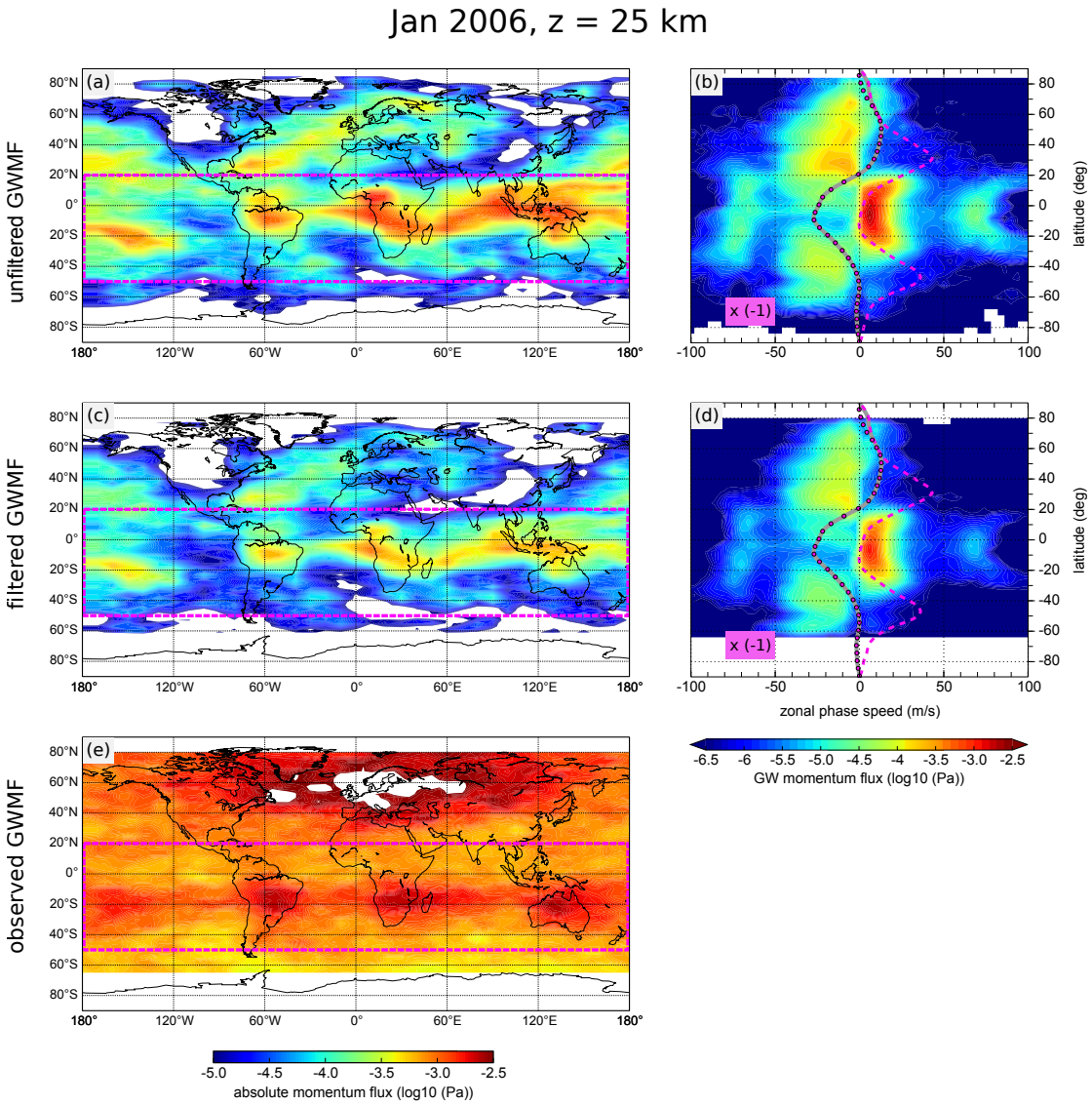

Figure 6.8: Horizontal distribution of (a) unfiltered absolute GWMF and (c) filtered absolute GWMF in comparison with (e) horizontal distribution of observed absolute GWMF. Panel (b) shows phase speed spectrum of unfiltered zonal GWMF (absolute values) and panel (d) shows phase speed spectrum of filtered zonal GWMF (absolute values). In phase speed spectra, GWMF values associated with negative values of phase speed (on the left-hand side) are multiplied with -1. Results are shown for January 2006 at 25 km altitude. For details see text.

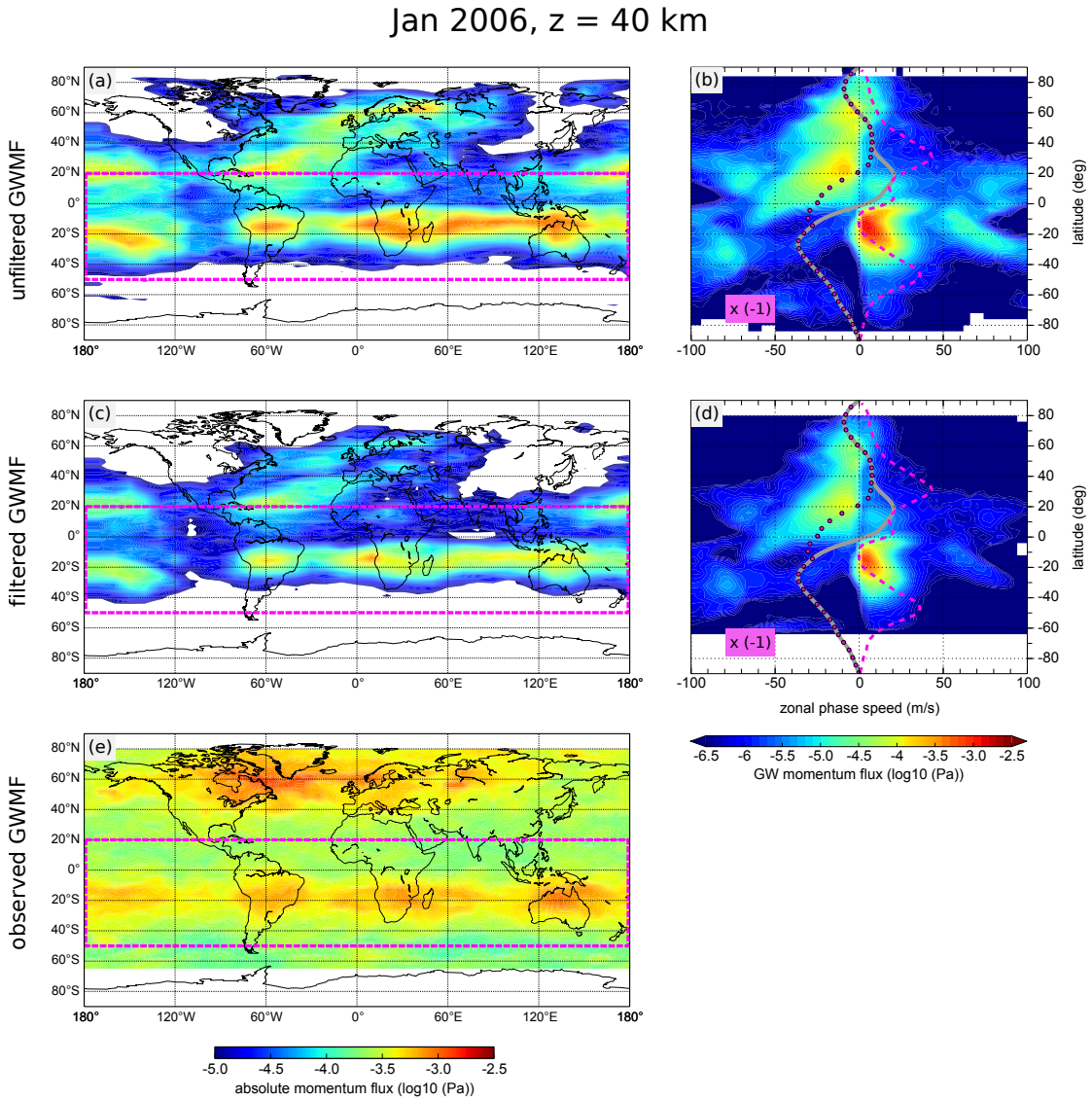

Figure 6.9: Same as Fig. 6.8, but for the altitude of 40 km.

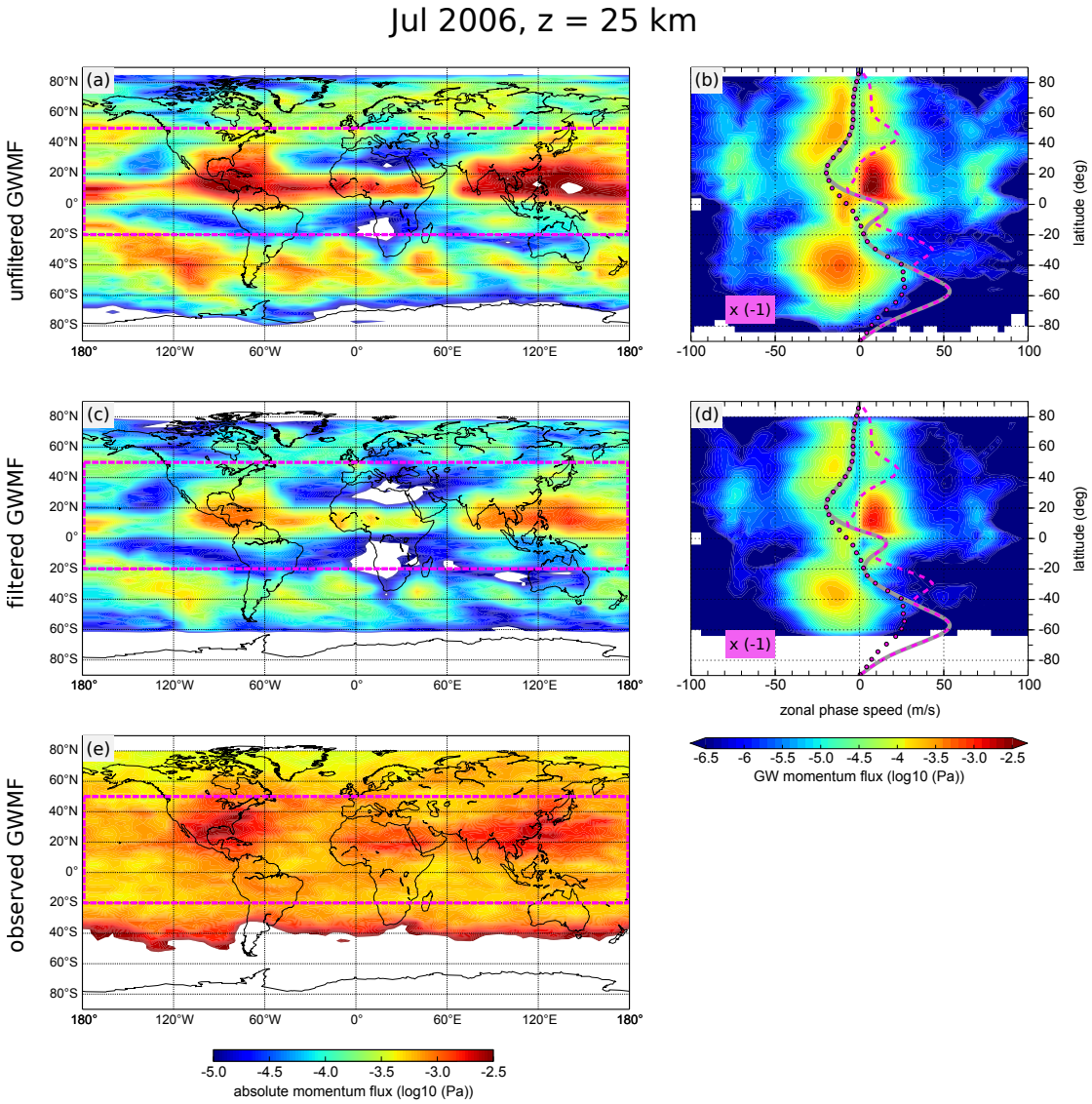

Figure 6.10: Same as Fig. 6.8, but for July 2006, at 25 km.

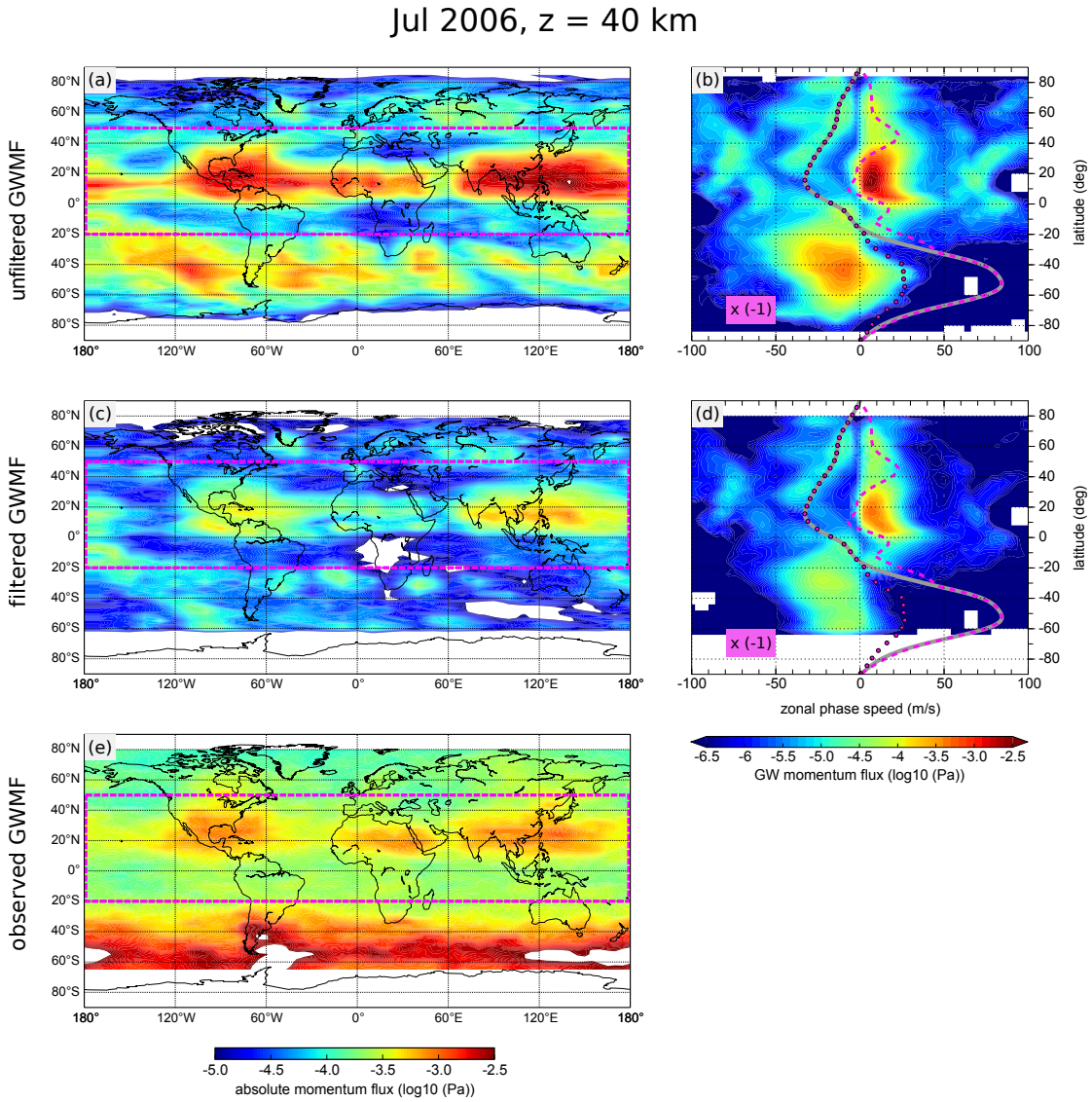

Figure 6.11: Same as Fig. 6.8, but for July 2006, at 40 km.

6.4 Conclusion

In this chapter, spatial and temporal scales of the CGWS scheme (*Song and Chun*, 2005) were systematically tuned to find the best match between simulated and observed horizontal and vertical wave number spectra of GWMF. The trajectory calculation for convective GWs generated by the CGWS scheme was performed using GROGRAT (*Marks and Eckermann*, 1995; *Eckermann and Marks*, 1997). For comparison with HIRDLS observations, a comprehensive observational filter, which was described in chapter 5 was applied. The observed spectra can be well reproduced in terms of spectral shape and location of the peak by super-imposing four scale sets. The spectral shape of GWMF in the summer subtropics is different for January and July. Matching of simulated and observed spectra can only be achieved by different combinations of scale sets of the convective source, indicating that this is an effect of the source properties rather than of the propagation conditions or observational filter.

We considered the contribution of these waves to the momentum balance by calculating zonal mean cross sections of absolute GWMF and its vertical gradients and compared them to respective observed quantities. The zonal average of filtered simulated GWMF is consistent with observed GWMF in the summer subtropics in both structure as well as magnitude. Applying the observational filter to the model, we find that in the mid stratosphere in regions of wind shear, slow GWs are refracted to very short vertical wavelength. Consequentially, these waves cannot pass the observational filter of HIRDLS and remain invisible while dissipating and exerting GWD at the location closely above the altitude where they become invisible to the instrument. Close to the stratopause waves of longer vertical wavelengths from all propagation directions reach saturation amplitudes and dissipate, in some cases without exerting much net drag. Similar to the absolute GWMF, the vertical gradient of filtered GWMF agrees well with the observed vertical gradient. Values of simulated zonal drag X are of the same order as the expected GW driving of the QBO (*Ern et al.*, 2014). This indicates that GWs from convection organized at scales of the order of 100 km or several 100 km are important for driving the QBO.

Horizontal distributions of absolute unfiltered and filtered GWMF are also presented in this chapter. These horizontal distributions show a good agreement with observed horizontal distributions in the structure as well as the magnitude. Main convection hot spots are well reproduced. We also showed the GWMF spectra in terms of zonal phase speed and latitude. These spectra show a main peak in the tropics and summer subtropics associated with eastward phase speeds between several m/s and about 30 m/s. As convective gravity waves are commonly believed to dominate the tropics and subtropics, these phase speed spectra are expected to match respective observations of the same regions.

The vertical gradient of absolute GWMF provided by measurements is not always an indication of drag. At places where gravity waves have grown to reach saturation amplitudes contributions from different propagation directions cancel each other. We see such a case, for instance, in the southern subtropics around

the stratopause in January. In addition, waves may leave the observational filter but do not break. For instance, it was argued by *Alexander* (2015) that in this way the comparison of vertical gradients of observed absolute GWMF with a momentum balance of the QBO shown by *Ern et al.* (2014) is not meaningful. The spectra inferred here show that zonal wind filtering of GWMF occurs for slow phase speed waves and in a very similar way for unfiltered and filtered simulations. Accordingly, in the zonal means there is a large similarity between simulated P (the quantity corresponding to observations) and the absolute values of simulated drag Q. The only effect we can find is that waves first leave the observational filter and break soon after above, which shifts the observed "drag" downward in comparison to the real drag, an effect which was already discussed by *Ern et al.* (2014). Regarding wave saturation effects, it has been discussed by *Ern et al.* (2015) that the situation becomes more complicated if wave saturation apart from critical levels occurs. In this case, additional information about the GW spectrum may be required (for example, like pre-filtering of the GW spectrum by the winds at lower altitudes) to correctly interpret vertical gradients of observed absolute GWMF.

Due to the limitations of current global observations, the synergetic use of physics-based models, observational filter and observations using both absolute values of GWMF and its vertical gradient is currently the most promising way to infer the true properties of GWs in the atmosphere. GWs from single convective cells with horizontal scales of a few kilometers cannot be constrained by limb sounder data and exist in parallel as studies using different instruments show (*Choi et al.*, 2009, 2012). The GWs exited by such events are clearly subgrid to global models and need to be parameterized, but also larger scale CGWs from organized convection may not well be represented depending on the convection parameterization (*Ricciardulli and Garcia*, 2000; *Kim et al.*, 2007; *Preusse et al.*, 2014) and would in this case need to be parameterized, even if the scales of potentially resulting GWs could be resolved by the dynamical core of the model.

Chapter 7

Summary and Outlook

In this thesis, characteristics of convectively forced gravity waves as well as their interaction with atmospheric background winds have been investigated. Due to the limitation of observations, especially observations which provide statistical information on the gravity wave spectrum, the scales of convective gravity waves as well as their dynamical contributions are still open issues. Three urgent questions were formulated in the introduction and are repeated and addressed below:

How are the observed gravity wave scales influenced by observation geometry and visibility effects?

The comprehensive observational filter has been developed and described in detail in chapter 5 of this thesis. The advance of this observational filter is that it considers for the first time both instrument visibility and observation geometry with a high level of accuracy. In particular, the observational filter comprises of four main processes: (1) visibility filter, (2) projection of the wavelength on the tangent-point track, (3) aliasing effect, and (4) calculation of the vertical observed wavelength. The first process (visibility filter) considers impacts caused by radiative transfer and retrieval (*Preusse et al.*, 2002), which directly influence the wave-induced temperature amplitude. The second process of the observational filter determines the wavelength along the measurement track and the associated reduction of GWMF by modifying this wavelength. The aliasing effect (the third process) estimates the projection of waves towards much longer wavelengths by aliasing and the corresponding reduction of GWMF. The calculation of the vertical observed wavelength (the fourth process) addresses effects of non-vertical altitude profiles.

What are the scales of gravity waves above convection?

To answer this question, in chapter 6 modeling of convective gravity waves was compared to observations. Convective gravity waves generated by this source scheme were propagated upwards using GROGRAT. Observational constraints were taken into account by applying the comprehensive observational filter on the simulated gravity waves. Scales used in previous studies MF1, MF2 are only to $\sim$2% and $\sim$17% visible to HIRDLS, respectively (cf. chapter 5).

A systematic variation and verification of spatial and temporal scales as free

parameters of the Yonsei model was performed in chapter 6. The simulated spectrum of gravity wave momentum flux with respect to horizontal and vertical wave numbers were calculated and compared to the respective observed spectrum. Based on this comparison, combinations of scale sets, which reproduce the observed gravity wave momentum flux spectrum were selected. The current approach is advanced since the observational filter is comprehensive and observations from limb sounders cover a large part of the gravity wave spectrum.

By using HIRDLS observations, the question of gravity wave scales above convection was partly answered. Results showed that the spectrum observed by HIRDLS can only be explained by considering large convective systems with horizontal scales of several hundred kilometers and temporal scales of several hours. These convective systems generate a large portion of the overall GWMF due to convective gravity waves. The short scales assumed in previous studies cannot explain the spectrum observed by HIRDLS. Those scales are associated with small convective cells and exist in addition. A full quantification is still missing. However, there seems to be a gap between the scales found in this thesis and scales used in previous studies (cf. chapter 6).

What are contributions to the atmospheric dynamics from convective gravity waves?

To answer this question, the momentum balance were considered by calculating zonal mean cross sections of absolute GWMF based on the scales determined above. These cross sections were compared to satellite observations. In order to study the interaction with atmospheric background wind, different vertical gradients of GWMF were calculated and compared to respective observed quantities. The zonal average of filtered simulated GWMF is consistent with observed GWMF in the summer subtropics in both structure as well as magnitude. Applying the observational filter to the model, it is found that in the mid stratosphere in regions of wind shear, slow gravity waves are refracted to very short vertical wavelengths and are therefore invisible to the instrument. These waves are found to dissipate and exert GWD at the location closely above the altitude where they become invisible to the instrument. Near the stratopause, waves of longer vertical wavelengths from all propagation directions reach saturation amplitudes and dissipate, in some cases, without exerting much net drag. Similar to the absolute GWMF, the vertical gradient of filtered GWMF agrees well with the observed vertical gradient. Values of simulated zonal drag X are of the same order as the expected GW driving of the QBO (*Ern et al.*, 2014). This indicates that GWs from convection organized at scales of the order of 100 km are important for driving the QBO.

Horizontal distributions of absolute unfiltered and filtered GWMF show a good agreement with observed horizontal distributions in structure as well as in magnitude. Main convection hot spots are well reproduced. GWMF spectra in terms of zonal phase speed and latitude show a main peak in the tropics and summer subtropics associated with eastward phase speeds between several m/s and about 30 m/s. Comparing different altitudes, modification of the spectrum by critical level filtering is identified.

Due to limitations of current measuring techniques as well as limited amount of observations, the complete picture of gravity wave spectrum in general, and of convective gravity wave spectrum in particular, is still on-going research. The investigations performed in this work present a unique approach to study the contribution of long-scale convective gravity waves to the dynamics of the atmosphere. The approach is advanced in many aspects, including a physics-based model, a comprehensive observational filter, determination of scales of convective systems based on observations, and a consideration of both absolute values of GWMF and its vertical gradients. It is noteworthy that observations from limb sounders cover a large part of the gravity wave spectrum. Knowing the contribution of these long-scale convective gravity waves provides an opportunity to further estimate the contributions of other parts of the convective gravity wave spectrum. These findings therefore contribute significantly to our current knowledge of gravity waves.

Appendix A

Techniques for observing gravity waves

A.1 Radiosonde

Standard radiosondes or PTU sondes measure temperature, humidity and horizontal wind. These data are provided as vertical profiles within an altitude range from about 200 m up to about 25–35 km. One of the advantages of radiosonde measurements is the high vertical resolution of 10–50 m. Radiosondes are typically launched twice daily at approximately 1000 stations worldwide. With an assumed rate of about 5 m/s, a vertical profile can be measured in 1-2 hours. Among various types of radiosonde, the Vaisala RS92 is widely used. For measurements in the stratosphere, the Vaisala RS92 radiosonde has an estimated random error of about 0.3 m/s for wind measurement and less than 0.3 K for temperature measurement (*Nash et al.*, 2005). Data provided by radiosondes are important for weather prediction models.

Owing to the high vertical resolution, measurements performed by radiosondes can provide significant information on short vertical wavelength gravity waves. Small perturbations due to gravity waves can be deduced from radiosonde measurements by filtering out the long vertical wavelength waves. A number of important gravity wave parameters can be derived, such as dominant vertical wavelength, based on spectral analysis of temperature perturbations (e.g. *Allen and Vincent*, 1995), potential and kinetic energy. In addition, the wave intrinsic frequency can be deduced using the hodograph method (*Gill*, 1982) or via the kinetic-potential-energy ratio (*Geller and Gong*, 2010), or the Stokes parameters method (*Eckermann and Vincent*, 1989; *Eckermann*, 1996). The GWMF is mainly derived by standard method using temperature perturbation and horizontal wind perturbation. Alternatively, GWMF can be derived by the approach introduced in *Ern et al.* (2004) using temperature perturbation, horizontal wavelength and dominant vertical wavelength. Another alternative method to calculate GWMF is based on

vertical and horizontal wind perturbations, which can be applied only to waves with large vertical wind amplitude. Among various studies focusing on radiosonde observations, several studies have shown seasonal variations as well as global distributions of gravity waves (*Allen and Vincent*, 1995; *Wang et al.*, 2005; *Gong et al.*, 2008). Nevertheless, radiosonde observations cover altitude ranges only up to 30 km, derived vertical wavelengths are restricted to an upper limit of 10 km and global coverages are very limited.

A.2 Rocketsonde

Rocketsondes or datasondes measure atmospheric temperature using a radiation-shielded thermistor. These instruments are launched by a sounding rocket and deployed from an altitude of 80 km or even higher. They are suspended below a parachute, which is called Starute. The uncertainty of rocketsondes measurement varies with the air density, and therefore with the altitude. The lower the air density is, the larger corrections have to be applied. Under operation of an experienced team, the uncertainty at 60 km altitude is less than 2 K. At 55 km and 30 km altitude, this uncertainty is less than 1 K and 0.5 K, respectively. In addition, winds can also be measured using radar-tracking of the Starute. Similar to radiosondes, the vertical wavelengths derived from rocketsondes are less than 10 km. Horizontal wavelength can be calculated via dispersion relation. Since temperature and wind perturbations can be determined, the GWMF can be calculated either by standard method using temperature perturbation and horizontal wind perturbation or by method suggested in *Ern et al.* (2004). Rocketsonde observations have been utilized by *Preusse et al.* (2003) to validate the observational filter for gravity waves for the CRyogenic Infrared Spectrometers and Telescopes for the Atmosphere (CRISTA).

A.3 Research aircraft

Research aircrafts provide in-situ, high-frequency wind and pressure measurements along the flight legs. These observations can be used to extract information on gravity waves. Research aircraft measurements possess several advantages. First, the technique employed is quite simple. Second, since the wind vector is measured, not only the value but also the direction of the vertical flux of horizontal gravity-wave momentum can be deduced directly. In addition, aircraft measurements can be performed at the altitude and location near the expected gravity wave sources in the troposphere. Therefore, these measurements can supply significant information about characteristics of waves near the source level as well as features and mechanism of gravity wave sources. On the other hand, research aircraft flights are expensive. Hence, measurements are limited in certain geographic areas to study specific gravity wave sources, such as convection (e.g. *Pfister et al.*, 1986; *Alexander and Pfister*, 1995; *Alexander et al.*, 2000) or mountain waves (e.g. *Brown*,

1983; *Nastrom et al.*, 1987; *Doyle et al.*, 2002). Aircraft measurements are therefore not able to provide global distributions of gravity waves. Moreover, aircraft measurements are also limited in the altitude range. Typical research aircrafts flight in the troposphere and can only reach the lower stratosphere. Processes such as propagation, dissipation and wave breaking above the lower stratosphere cannot be observed. In addition, aircraft measurements can detect only relatively short horizontal wavelength ($< 500\,\mathrm{km}$) gravity waves (*Alexander and Pfister*, 1995). In recent years, several measurements using unmanned aircrafts (for example Global Hawk) with considerably extended geographical range have been performed. These flights are, however, expensive and not allowed over land, leading to inadequate statistics. In the future, if these limitations can be overcame, unmanned aircrafts may provide a new possibility to obtain global distributions of GWMF.

A.4 Long-duration balloon

Long-duration balloons developed by the French Space Agency (CNES) can carry scientific payloads up to 50 kg and measure in-situ temperature, pressure, and balloon position every 30 s. These measurements can be used to obtain information on gravity waves. The balloons are designed to keep a constant volume during their flight and therefore drift along the surfaces of constant density between 17 and 21 km for several months. It should be noted that information provided by balloon measurements is mainly time series of meteorological parameters. In the frequency range of gravity waves, the balloon is assumed to be a perfect tracer of the wind. Horizontal wind component hence can be calculated based on the change of the balloon position. Vertical perturbations due to gravity waves can be inferred from vertical displacements of the balloons, which are proportional to the vertical displacements of the isentropic surfaces (*Vincent and Hertzog*, 2014). Since the balloons drift along the wind, the intrinsic frequency of gravity waves is measured. This is an advantage of the balloon measurements, which allows to calculate the GWMF directly without inferring horizontal and vertical wavelengths (*Boccara et al.*, 2008). Furthermore, since vertical velocity, horizontal velocity, as well as intrinsic frequency are measured simultaneously, directional gravity wave momentum fluxes can be estimated, making long-duration balloon a unique technique. In addition, owing to the long trajectories covering spacious geographical areas, balloon measurements can provide significant information on the relative role of different gravity-wave excitation mechanisms or supply a statistical representation of the gravity-wave field in the lower stratosphere (*Hertzog et al.*, 2008). Recently, two successful campaigns using long-duration balloons have been performed in 2005 (the Vorcore campaign) and in 2010 (the Concordiasi campaign). Observations from these campaigns have been used in various gravity wave studies (e.g. *Hertzog et al.*, 2008; *Plougonven et al.*, 2008; *Jewtoukoff et al.*, 2013; *Plougonven et al.*, 2013, 2015).

A.5 Radar

Radar observations have been used for gravity wave studying for a long time (e.g. *Vincent and Fritts*, 1987; *Sato*, 1993; *Tsuda et al.*, 1990, 1994b; *Nakamura et al.*, 1993). The observations are typically obtained by sending electromagnetic pulses (in the radio-frequency range) into the atmosphere and receiving backscattered signals, which were scattered due to inhomogeneities of the atmospheric refractive index. By comparing the Dopplershifted frequency of the scattered waves with the emitted frequency, vertical profiles of horizontal and vertical wind can be deduced. In addition, the horizontal wind component can also be estimated by analyzing the horizontal shift of the diffraction pattern caused by the scattering layer on the ground. This technique is known as spaced antennas (*Hocking*, 1997).

One of the favourable features of radar measurements is that the vertical wavelength of gravity waves can be directly deduced. The horizontal wavelength can be inferred using hodograph with limitation of wave period from 0.5 to 15 hours. On one hand, radars are advanced in observing small-vertical-scale waves owing to their high vertical resolution. In particular, the vertical resolution of up to several hundreds meters allows to resolve waves with vertical wavelength as short as 1 km. On the other hand, radar measurements are limited in the altitude range. Typically, radars can measure from near the surface to about 15-25 km. In the middle and upper stratosphere due to very low density of scattering inhomogeneities, measurements cannot be performed. In the mesosphere and lower thermosphere, the VHF and MF radars are again able to provide wind measurements. The upper height limit of radar measurements in the lower stratosphere depends on the radar frequency, the power as well as the radar configuration. Due to this limit in the lower stratosphere, analyses are restricted to gravity waves with vertical wavelengths less than 10 km. For radars, GWMF can be calculated either directly based on the dual-beam technique (*Vincent and Reid*, 1983) or by using the hodograph analysis (*Serafimovich et al.*, 2006; *Hoffmann et al.*, 2006). For both approaches, GWMF of waves with periods of longer than 1 hour is typically provided. The Middle Atmosphere Alomar Radar System (MAARSY) can provide information of waves with intrinsic periods of about 15 min (*Stober et al.*, 2013).

Another advantage of radars is the possibility to perform measurements continuously for long periods of time regardless meteorological conditions. Nevertheless, measurements performed at only a limited number of locations makes radar observations not able to provide global distributions of gravity waves.

A.6 Lidar

By detecting Rayleigh backscatter and rotational vibrational Raman backscatter, lidars provide time series of temperature and wind profiles. In the troposphere, lidars measure the temperature-dependent Boltzmann distribution of rotational Raman lines. At higher altitudes (above 10–20 km), Rayleigh and vibrational

Raman backscatter are used to measured the relative air density profile. These measurements at higher altitudes are then hydrostatically integrated to deduce absolute temperatures. Above 10 km altitude, the wind velocities in two different directions along the line-of-sight are estimated based on Doppler shift of molecular backscatter.

Lidar measurements are advanced in covering a wide altitude range starting from the troposphere up to the lower mesosphere. Moreover, with typical integration of 30–60 min, temperature and wind profiles are derived with high vertical resolution, which allows to detect gravity waves with vertical wavelength as short as 1 km in the upper stratosphere and lower mesosphere. This vertical resolution depends upon altitude. Statistical errors of lidar measurements also depend upon altitude. Below 40 km, these errors are in the range of 1–2 K and 1–2 m/s for temperature and wind, respectively (*Gerding et al.*, 2008; *Baumgarten*, 2010). Gravity wave parameters are derived using long (more than 3 hours) time series measurements. To infer gravity wave parameters, the background profile is first estimated by averaging all time series data. Next, time series of gravity-wave induced perturbations are calculated by subtracting the averaged profile from all individual profiles (e.g. *Rauthe et al.*, 2008). If both temperature and wind data are provided, GWMF can also be calculate from lidar measurements.

Lidar observations have been limited to a few specific locations. The Leibniz-Institute of Atmospheric Physics, for example, employ Rayleigh-Mie-Raman lidars for temperature soundings at Kühlungsborn, Germany (at 54° N, 12° E) (*Alpers et al.*, 2004). In addition, wind soundings are performed at ALOMAR (Andenes, Norway, at 69° N, 16° E) (*Baumgarten*, 2010). These measurements provide long-term data sets for studying gravity wave variations and comparing with observations from other measurement techniques.

Despite the fact that lidars are able to measure only during the night time and the observations are limited to only certain locations, measurements supplied by lidars have been used for investigating seasonal variations of gravity waves in many studies (e.g *Wilson et al.*, 1991; *Marsh et al.*, 1991; *Whiteway and Carswell*, 1995).

A.7 Airglow imaging

Structures of gravity waves at mesospheric altitudes can be inferred by analyzing airglow images of three layers in this altitude region. Some efforts also have been made to combine the measurements from various layers. From these airglow images, the least–square technique is used to determine horizontal parameters of the wave pattern by fitting the wave crests of each ground mapping to sets of concentric circles (*Hapgood and Taylor*, 1982). By this approach, radius of all circles are first estimated. Next, the horizontal wavelength can be calculated based on average distance between the circles as well as the expansion rate of them. This method allows to infer horizontal wavelength and horizontal velocity with an accuracy of about 5%. Assumption of the airglow layer altitude introduces an

additional error into the estimation. For instance, an error in altitude estimation of 5 km would increase the total error by 6%. In case wind profiles are measured simultaneously, GWMF can also be deduced from airglow imaging. With assumed buoyancy frequency, the upward propagating energy can also be deduced (*Taylor et al.*, 1987, e.g.). Moreover, wave spectrum can also be determined using spectral analysis (e.g. *Taylor and Garcia*, 1995; *Gardner et al.*, 1996).

Airglow imaging technique is, however, limited to only a small altitude range in the vicinity of the mesopause, between 86 km and about 120 km and measurements can only be performed during the night time. Moreover, airglow imaging is most sensitive to waves with horizontal wavelengths less than 100 km. Despite these limitations, airglow imaging have been utilized in numerous gravity wave studies (e.g. *Taylor et al.*, 1987; *Swenson and Espy*, 1995; *Isler et al.*, 1997; *Haque and Swenson*, 1999).

A.8 Spaceborne instruments

Spaceborne measurements provide a great opportunity to observe gravity waves from space. Spaceborne techniques are diverse, including, for example, nadir sounding, near-nadir sounding, limb sounding, sub-limb sounding, GPS Radio-occultation.

Nadir-viewing spaceborne instruments

Spaceborne nadir and near-nadir viewing instruments are able to image gravity waves in the stratosphere. These instruments are advanced in providing (quasi-) horizontal two-dimensional cross-sections of gravity wave induced perturbations in microwave frequency range. One example of this intrument type is the Advanced Microwave Sounding Unit–A (AMSU–A) onboard meteorological weather satellites and the Aqua satellite. Microwave radiances observed by this instrument can be used to infer temperature amplitudes (e.g. *Eckermann and Wu*, 2006; *Eckermann et al.*, 2006). A favourable feature of this instrument type is that the horizontal wavelength as well as wave propagation direction can be directly estimated. However, this type of instrument is only sensitive to gravity waves with horizontal wavelengths of more than 150 km.

The measurements provided by the Atmospheric Infrared Sounder (AIRS) instrument were utilized to analyze vertical cross-sections of gravity wave field along the satellite track. This analysis allows to derive directly the vertical wavelength (e.g. *Alexander and Teitelbaum*, 2007; *Hoffmann and Alexander*, 2009). In comparison with AMSU–A, AIRS has a better horizontal resolution owing to smaller footprint size ($\sim$13.5 km in comparison with $\sim$48 km).

For both AMSU–A and AIRS, the vertical resolution is restricted by the relatively broad weighting functions of the instrumental channels and therefore can only observe gravity waves with vertical wavelengths of more than 10 km. For this type of instrument, estimation of GWMF is complicated because the radiance re-

sponse to wave-induced perturbation depends upon the observation geometry of the instrument. As a consequence, only a limited number of studies have computed GWMF for the quasi-monochromatic observed perturbations (*Eckermann et al.*, 2007; *Alexander et al.*, 2009).

GPS Radio-occultation

The possibility of using GPS radio-occultation (GPS-RO) to retrieve 3D wave vectors from closely collocated GPS measurements has been recently examined by *Wang and Alexander* (2010). In their study, *Wang and Alexander* (2010) considered the early phase of the COSMIC GPS-RO mission when 6 satellites were located on near-by orbits, leading to a remarkably high number of coincident measurements. In some regions, complete set of GW parameters including momentum flux and horizontal propagation direction can be inferred from the derived gravity wave temperature perturbations. The inferred 3D wave fields show significant consistence with our current knowledge of gravity waves. Nevertheless, this technique assumes existence of a dominant wave mode in each single longitude $\times$ latitude $\times$ time cell, while in reality, gravity waves are likely intermittent and localized. Together with sparse sampling inherent, this assumption leads to some uncertainties of this technique. Moreover, several wave modes can exist in a single cell. This, however, cannot be described in the current approach of this technique and will lead to some additional uncertainties. Furthermore, since the COSMIC satellites currently are relocated on further distant orbits, 3D features are no longer be retrieved. Finally, as the information supplied by 1D retrievals from various viewing directions is combined, some concerns about this technique exist.

Emission limb sounding

Limb sounding of gravity waves provided important information on gravity waves with global coverage. For example, the Limb Infrared Monitor of the Stratosphere (LIMS) instrument (*Gille and Russell*, 1984) covered an altitude range from 15 to 60 km. Temperature measurements by LIMS have a high vertical resolution of about 1.5 km. However, due to the observation geometry as well as the Kalman filter used for removing large-scale waves, derived gravity waves from LIMS observations have vertical wavelengths from 6 to 50 km and horizontal wavelengths of more than 200 km (*Fetzer and Gille*, 1994). The Cryogenic Infrared Spectrometers and Telescopes for the Atmosphere (CRISTA) (e.g. *Riese et al.*, 1999) has better horizontal resolution and slightly better vertical resolution in comparison with LIMS. The altitude range covered by CRISTA depends on observation mode, but can be from about 20 to about 100 km. Temperature measurements of CRISTA have been analyzed to deduce gravity wave information (e.g. *Preusse et al.*, 1999) and good agreement with observations from LIMS was found (*Preusse et al.*, 2000).

More details about limb sounding technique as well as a comprehensive obser-

vational filter for this technique is described in chapter 5.

A.9 Potential new technique: GLORIA

The Gimbaled Limb Observer for Radiance Imaging of the Atmosphere (GLORIA) is an advanced instrument for infrared limb imaging of the atmosphere from aircraft. A great asset of GLORIA is the combination of a Fourier transform infrared spectrometer with a two-dimensional detector array. This combination allows to provide unprecedented two-dimensional high spatial resolution limb images. In addition, the instrument is mounted on a highly flexible gimbaled structure, which allows the horizontal view angle to vary from 45° to 135° with respect to the flight direction. GLORIA can also be placed on spacecrafts. In case of spacecrafts, its measurements would provide an excellent opportunity to deduce 3D gravity wave vectors and could lead to significant improvements of our knowledge of gravity waves (*Preusse et al.*, 2009b). When mounted on an aircraft flying in a circle, measurements by GLORIA using multiple viewing directions are able to provide 3D distributions of temperatures and trace gases. These 3D distributions can be obtained for an enclosed atmospheric volume of typically 400 km diameter based on tomographic retrieval methods (*Ungermann et al.*, 2011). With these methods, the vertical resolution is expected to be better than 500 m and the horizontal resolution is in the order of 30 km without preferential direction.

It is noteworthy that 3D retrieval can start about 2 km below the flight altitude. Therefore, if the Geophysica aircraft is used as a carrier for GLORIA, the highest altitude that 3D retrieval can reach is about 18 km. Since GWMF can only be inferred from temperature perturbations above the tropopause, valuable data for studying gravity waves may be obtained when the aircraft flights at mid and high latitudes in the winter hemisphere. The longest vertical wavelength that can be resolved by such flights is about twice of the observed vertical domain, i.e. about 20 km. Furthermore, as a circular-pattern flight takes more than one hour, low ground-based frequency waves (e.g. mountain waves) in a quasi stationary flow should be considered.

Appendix B

Applicability of the comprehensive observational filter to other types of instruments

In chapter 5 of this work we have discussed the observational filter for GWMF from spaceborne observations and focused on the case of instruments measuring optically thin emissions in limb scanning geometry. The measurement method determines the visibility filter as well as the observation geometry. Other kinds of instruments require different observational filters. In this section we will describe whether and how the general approach outlined here may be adapted to other techniques. We will start this by reconsidering some general limitations.

The direct inference of GWMF from wind perturbations requires to measure instantaneously all three components of the wind with an accuracy which cannot be reached from space with any technique existing or under development[1]. Instead, estimates of GWMF are based on the polarization relations and require to determine the horizontal and vertical wavelength in addition to the temperature amplitude (*Ern et al.*, 2004). In general, the phase of a gravity wave changes both in space and time and, analyzing the wavelengths and periods of a GW, this information must not be mixed (e.g. *de la Torre and Alexander*, 1995; *de la Torre et al.*, 1999; *Eckermann et al.*, 2006). However, considering a snapshot, we may focus on the spatial variations only and disregard temporal evolutions. As shown by *Alexander et al.* (2010), the shortest intrinsic periods visible to infrared limb sounding are ∼1 hour. Low Earth orbit (LEO) satellites have a velocity of ∼8 km s^{-1}, i.e. a typical GW wavelength of 500 km or less is covered in less than one minute. It is therefore safe to assume measurements from one orbit-segment to be instantaneous. On the other hand, the duration of an orbit is ∼1.5 hours. Although at the turning latitudes of the orbit, subsequent orbits may be sufficiently

[1]The vertical wind perturbations due to gravity waves usually have small magnitudes and measurements with a high accuracy are particularly required.

close for considering the same GW event, the phase of this wave likely has changed in the 1.5 hours which passed between these observations. For emission sounding with a single instrument it is therefore not promising to combine the observations of subsequent orbits nor is it promising to combine two instruments on different platforms. Of course, insight can be gained in case studies by revisiting the same region (e.g. *Preusse et al.*, 2002; *Eckermann et al.*, 2006, 2007), but one should not combine the phase information to infer wavelengths.

B.1 Potential Future Limb Imager

Gravity wave information has been retrieved from a number of infrared limb sounders, that is CRISTA (e.g. *Preusse et al.*, 2002; *Ern et al.*, 2006), CLAES (*Preusse and Ern*, 2005), SABER (*Preusse et al.*, 2009a; *Ern et al.*, 2011) and HIRDLS (e.g. *Alexander et al.*, 2008; *Wright et al.*, 2010; *Ern et al.*, 2011). Only CRISTA uses multiple viewing directions, but the observation tracks are separated by 600 km and thus too far apart for common analysis of the same GW events. In addition, all these instruments had to assume spherical symmetry for the retrieval and they cannot observe wavelengths which are shorter than the Nyquist wavelength of their sampling. Thus, the complex visibility filter, the projection of the wave to the measurement track and aliasing are inevitable for these instruments. They could, however, be remedied, if an instrument were designed for the purpose of measuring GWs (*Riese et al.*, 2005; *Preusse et al.*, 2009b). Viewing backward and sampling sufficiently frequently, 2D tomographic retrievals can be employed, which allow to reconstruct the true amplitude in that part of the spectrum generally visible to limb sounders (*Ungermann et al.*, 2010). This largely simplifies the visibility filter and strongly reduces its effect. Using 2D imaging, also across-track information would be achieved, which would allow for reconstruction of the 3D wave vector. Accordingly, the projection to the tangent-point track becomes obsolete. Finally, oblique-profile effects are removed in the retrieval.

B.2 Microwave Limb Sounder

In contrast to infrared limb sounders, for the microwave limb sounder (MLS) both on UARS (*Wu and Waters*, 1996b,a) and EOS-AURA (*Wu and Eckermann*, 2008) saturated radiances were utilized for GW studies. In this case the radiance does not stem from the tangent point, but from a part of the limb ray which is higher in altitude and closer to the instrument. The altitude associated with these observations is determined by the wavelength of the microwave radiation chosen for the analysis, and the sensitive volume is oriented oblique in the atmosphere. Accordingly, this geometry is called sub-limb (*Wu et al.*, 2006). Sub-limb observations

have a strong bias of waves (intrinsically) propagating towards the instrument (*Jiang et al.*, 2004b) and are most sensitive for waves at the edge of the visibility range of limb sounders (*McLandress et al.*, 2000; *Preusse et al.*, 2008). Due to the lack of vertical wavelength information, only in a single instance GWMF from MLS was published (*Jiang et al.*, 2006). For the comparison of modeled and measured radiance variances, the observational filter described here may be adapted: The equations for the visibility filter can be taken from *McLandress et al.* (2000). In case of MLS the large-scale structures of the atmosphere (e.g. planetary waves) are removed by along-track high-pass filtering. This is an essential part of the observational filter. For UARS MLS, which views 90° to the flight direction, along-LOS projection for the visibility filter and along-track projection for the background removal need to be considered separately (*Jiang et al.*, 2004b). For AURA-MLS which views forward, both steps may be combined in one observational filter.

B.3 GPS-RO

So far we have considered techniques where measurements were taken by a single instrument and the spacio-temporal collocation was reached by considering subsequent measurements on one orbit segment. In this case any given wave can be viewed only by a very limited number of geometries, i.e. ascending/descending orbit nodes and in case of SABER southward/northward looking viewing mode. The situation is very different for radio occultations between dedicated receiver satellites and transmitter satellites of the global positioning system (GPS-RO). For the COSMIC mission this involved 12 transmitter satellites and 6 receiver satellites resulting in ∼2000 GPS-RO profiles per day distributed quasi-randomly over the globe. Using maximum miss-distances and miss-times such as 15 deg and 2 hours, groups of three profiles may be identified from which to infer the 3D wave vector (*Wang and Alexander*, 2010; *Faber et al.*, 2013). This results in triples with an average distance of 1000 km and a sufficient number of events to generate meaningful seasonal-average maps. This different procedure has a number of consequences for the observational filter: First, the wave is viewed from different directions. This may not only lead to different amplitude degradations for the individual profiles, but also introduce different phase shifts in each of the profiles of the triple (*Belloul and Hauchecorne*, 1997; *Preusse et al.*, 2002). Second, in order to gain the best estimate of the 3D wave vector a complicated phase-dewrapping is required (*Faber et al.*, 2013). Because of these two points, it is likely best to estimate observational filter effects by performing the phase dewrapping for three given profile locations from simulated phases, which are calculated by applying individual LOS projection and visibility filtering including phase shifts. Finally, the general concept needs to be changed. In case of the emission sounders, for each wave the latitude position determines how this wave is viewed. In case of GPS a certain region may be viewed by completely different combinations of viewing geometries. That could, for instance, be solved by a stochastic approach.

B.4 Nadir Sounding

There is a number of studies utilizing nadir sounding of thermal emissions in the infrared and microwave spectral region. This technique has the advantage of resolving the horizontal wave structure. However, GWMF was only deduced in case studies, for example for the AIRS instrument (*Alexander and Teitelbaum*, 2011). Nadir sounding satellites have, in principle, a more simple geometry. The horizontal resolution depends mainly on the footprint size and sampling, the vertical resolution is given by the radiative transfer. For the outer track the geometry approaches sub-limb and the observational filter becomes more complicated (*Eckermann et al.*, 2007). The latter allows also for deducing directional propagation preferences from AIRS radiances (*Gong et al.*, 2012). Finally, the actual observational filter may depend as much on the analysis technique as on the instrument itself.

B.5 Summary

To sum up, the observational filter described in this thesis can be adapted to other measurement techniques. In particular, for the potential future limb imager, the visibility filter will be more simple. Projection of the wave on the measurement track, aliasing effect and oblique-profile effect are not further needed. In case of MLS, for radiance variances, the observational filter can also be adapted using equations from *McLandress et al.* (2000) for the visibility filter, and considering the large-scale structure removal by along-track high-pass filtering. However, much more effort is needed to adapt the current observational filter to GPS-RO: in contrast to emission measurements, the observations geometry varies with each individual sounding even for a given latitude. True nadir sounding has a simpler observational filter than infrared limb and can be treated accordingly. Finally, it is important to mention that the infrared limb sounding technique can cover a large part of the GW spectrum. A comprehensive observational filter for this technique therefore is essential for quantitatively confining resolved and parameterized GWs in global models.

Appendix C

Background removal and noise

In chapter 5 we have developed the observational filter for infrared limb sounders. The observational filter was defined in a deterministic way and the different involved steps are inevitable. For a given wave and a given instrument (including orbit direction) all effects described here will apply only in the way as they are described here. These effects do not depend on the specific method used for the interpretation of the data, for instance, which kind of spectral analysis is used for the vertical profiles (e.g whether to use MEM/HA (*Preusse et al.*, 2002), S-transform (*Alexander et al.*, 2008), or multi-component S-transform (*Wright and Gille*, 2013)). This independence of these effects works well in case of infrared limb sounders, since the background removal does not strongly affect the visible wavelengths and since the instrument noise level is low. This separability is not given e.g. in the case of MLS, where the background removal significantly influences the visible wavelengths (cf. MLS in Appendix B). Of course background removal and noise still may influence the measured GWMF distributions, but it is much more straightforward to take them into account in the error estimates of the measured distribution. We will discuss both effects briefly in this section.

C.1 Background removal

In case of infrared limb sounders the background is usually removed by determining planetary waves up to wave number 6 and subtracting these waves from the individual measurements. Though the basic approach is the same, different techniques have been applied including Kalman filter (*Fetzer and Gille*, 1994), Kalman filter and additional split into ascending and descending orbits for tidal removal (*Preusse et al.*, 2001), S-transform (*Alexander et al.*, 2008) and spatio-temporal decomposition (*Ern et al.*, 2011, 2013). Though the wave number 6 is technically driven by the orbit geometry of LEOs, which allows for the determination of planetary waves up to a maximum of 7 (*Salby*, 1982), it turns out to be a rather good choice at least for the stratosphere and mesosphere: The main contributions of planetary scale waves in terms of variances are mainly contained

in zonal wave numbers up to 4 (e.g. *Ern et al.*, 2008; *Ern and Preusse*, 2009). This means that planetary waves can be completely removed. Gravity waves have much shorter wavelengths than zonal wave number 6 and are therefore not removed. The latter was shown, for instance, by *Preusse et al.* (2006) who find that the horizontal wavelength distribution of measured GWs follows largely a fixed ratio between intrinsic frequency of GWs and Coriolis parameter $\hat{\omega}/f$ than following the wave number limit which would have been implied by the background removal. Though the background removal thus does not influence the observational filter, the determination of the planetary scale waves is an error source. If these waves are not captured in full, GW variance will be overestimated, if part of the GW structure is erroneously projected into planetary scale waves, GW variance will be underestimated.

C.2 Noise

The noise level of infrared limb sounders is typically a fraction of 1 K in the stratosphere and typically more than 1 or 2 K in the upper mesosphere. Noise levels for HIRDLS and SABER as well as the references where to find them are given in (*Ern et al.*, 2014). This compares to typical GW amplitudes of a few K in the stratosphere and more than 10 K in the upper mesosphere. Noise for the leading spectral components employed for GWMF estimation is further reduced by using a number of points in the spectral analysis of the vertical profiles. In regions of prominent sources and favourable propagation conditions, the influence of noise is hence at least an order of magnitude below the typical size of GW variance and GWMF. The case may be different in the summer high-latitude lower stratosphere where the wind reversal between tropospheric westerlies and stratospheric easterlies largely prevents GWs from entering the stratosphere (cf. e.g. *Kalisch et al.*, 2014, and references therein). In this region, noise may indeed have a larger influence on the determined level of GWMF and this region could be used for a check of the noise-induced background level of GW variance and GWMF.

For the technique applied in our own research one may perform kind of a plausibility check. For the evaluation of GWMF we use only the major spectral component. In regions where GWs are prominent the influence of noise on this component is marginal (see paragraph above). We now can compare the total variance determined directly from the temperature residuals after background removal (P1), the total variance of GWs from the major spectral component as analyzed for single profiles (P2), and the total variance of GWs from profile pairs where the vertical wavelength of the two single profiles reasonably well agree (P3). If the vertical wavelength agrees in profile pairs, one may argue that one chiefly has captured true GW events, whereas in the single profiles there could be a higher fraction of results dominated by noise. However, the variance values for single profiles (P2) and profile pairs (P3) agree very well (*Ern et al.*, 2014; *Geller et al.*, 2013). This is a plausibility check that after the spectral analysis the contribution

of noise is low. On the other hand the major spectral component captures about 70% of the initial variance (*Ern et al.*, 2014). This means that we likely have also captured the main part of the GWMF. Since at a certain location likely more than one GW is found quite frequently, also the remaining part of the variance is probably dominated by GWs. This, in turn, indicates that even in the direct variance estimate the contribution of noise is quite small.

The observational filter of infrared limb sounders as described here is deterministic and independent of the individual evaluation method. The removal of the background and instrument noise will cause different GWMF errors depending on the chosen method. Noise and background removal therefore rather belong to the error of the distribution than to the application of the observational filter and may be estimated e.g. by simulated data in a Monte Carlo simulation. This is, however, not topic of this thesis.

Appendix D

Dependences of β and γ on latitude

Figure D.1 shows variations of β and γ against latitude. In particular, Fig. D.1a and D.1b present the variances for the northward-viewing mode and Fig. D.1c and D.1d for the southward-viewing mode of SABER. For HIRDLS, the dependences of β and γ on latitude are shown in Fig. D.1e and D.1f. For all panels in this figure, ascending orbit is presented in the left column and descending orbit is in the right column.

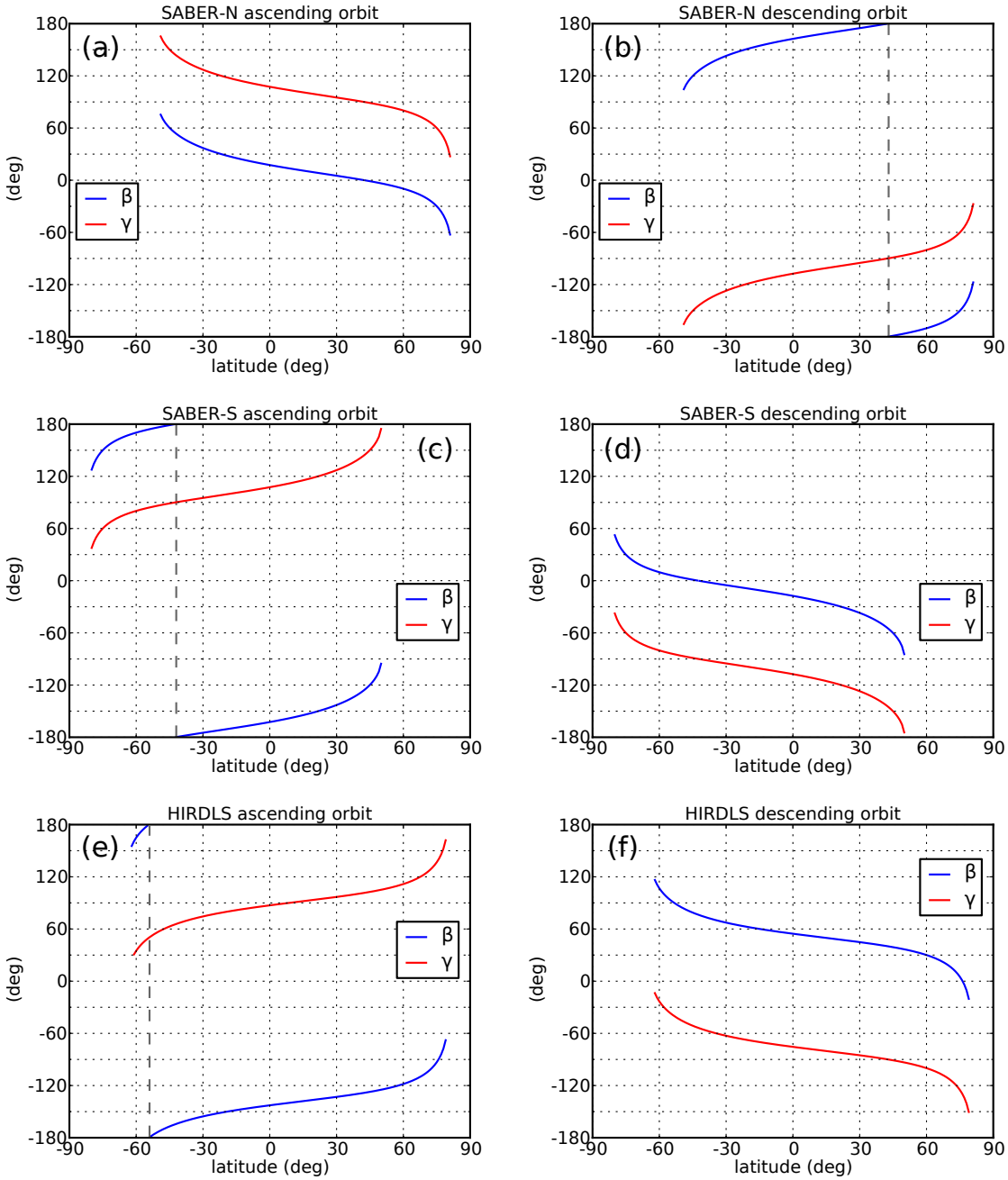

Figure D.1: Dependences of β and γ on latitude for different orbit directions of **(a–d)** SABER and **(e, f)** HIRDLS. For details see text.

Appendix E

Scaling factor α

In this appendix, in order to demonstrate the impact of the tuning factor α, we compare zonal averages of GWMF and its gradient for $\alpha = 1$ (no amplitude tuning at the launch level) and for $\alpha = 5$.

Comparison of zonal averages of GWMF

Zonal averages of GWMF are shown in Fig. E.1 for January 2006 and in Fig. E.2 for July 2006. In each of these figures, the left column shows zonal averages of GWMF for $\alpha = 1$ and the right column shows zonal averages of GWMF for $\alpha = 5$. The unfiltered GWMF is shown in the upper row and the filtered GWMF is shown in the lower row.

For January, the zonal averages of GWMF are very similar for $\alpha = 1$ and for $\alpha = 5$. This similarity is true for both unfiltered GWMF and filtered GWMF. This similarity can be seen by comparing Fig. E.1a to Fig. E.1b and comparing Fig. E.1c to Fig. E.1d. However, the magnitude of GWMF for $\alpha = 5$ is higher than the one for $\alpha = 1$.

For July, similar features are also found. Zonal averages of GWMF for $\alpha = 1$ and for $\alpha = 5$ have the same structure, but the magnitude of GWMF for $\alpha = 5$ is higher than the one for $\alpha = 1$. This is also true for both unfiltered GWMF and filtered GWMF and can be seen by comparing the left column to the right column in Fig. E.2.

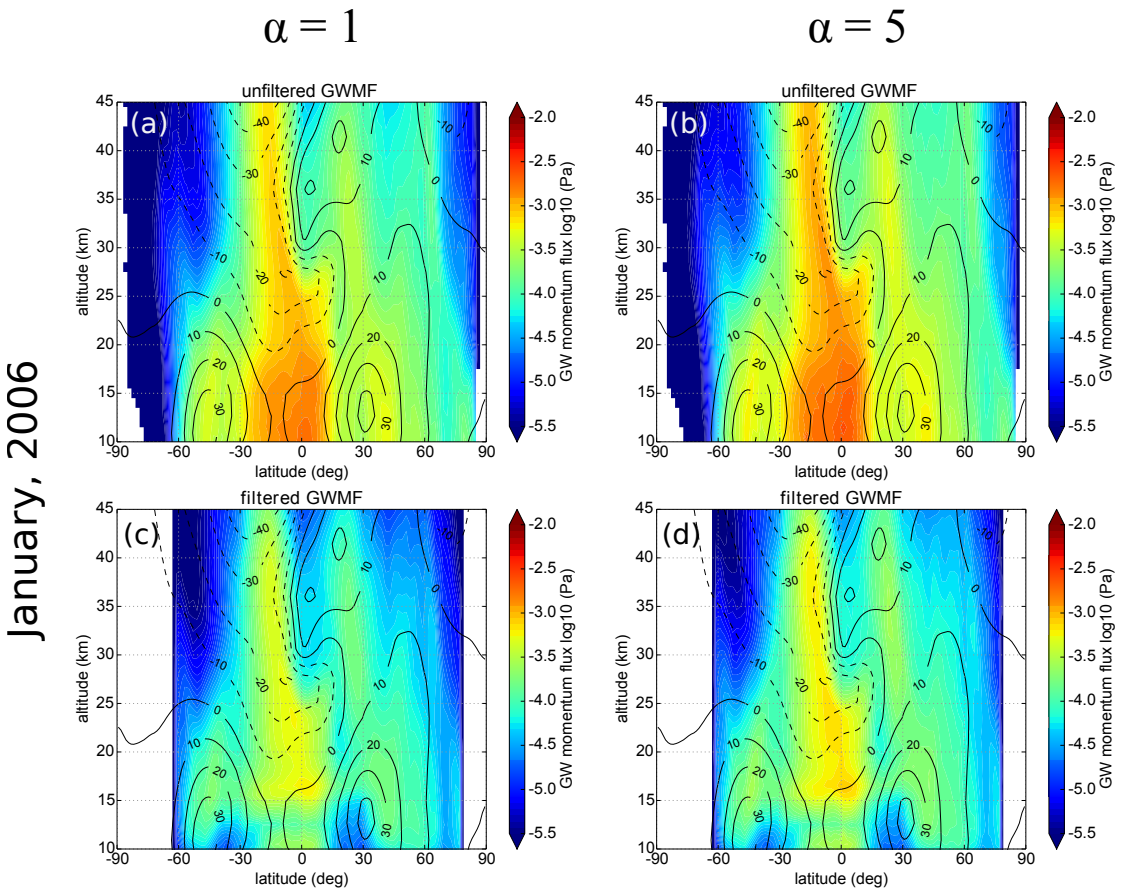

Figure E.1: Zonal averages of GWMF for January 2006 for $\alpha = 1$ (left column) and $\alpha = 5$ (right column). The upper row shows unfiltered GWMF and the lower row shows filtered GWMF.

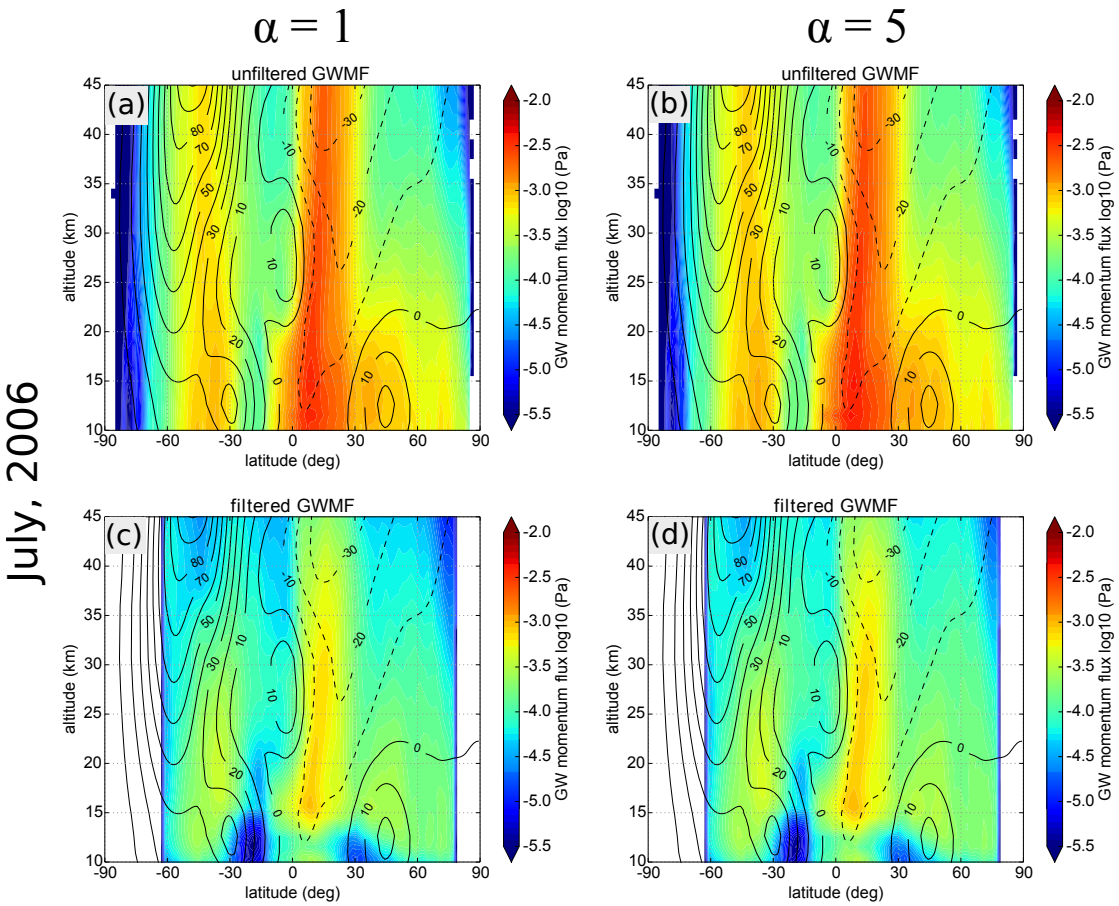

Figure E.2: Same as Fig. E.1 but for July 2006.

Comparison of vertical gradients of GWMF

Zonal averages of vertical gradients of GWMF are shown in Fig. E.3 for January 2006 and in Fig. E.4 for July 2006. In each of these figures, the left column shows vertical gradients for $\alpha = 1$ and the right column shows vertical gradients for $\alpha = 5$. The first row shows simulated zonal drag X, the second row shows simulated Q and the third row shows simulated P.

As we have discussed in chapter 6, reducing initial amplitude at launched level by $1/\sqrt{\alpha}$ and simultaneously multiplying GWMF by α can change the pattern of vertical gradients. In particular, it may shift the saturation upwards. For the simulated zonal drag X, this upward shift can be seen clearly for both January and July. For January, positive drag at $\sim$5 ° S and $\sim$10 ° N is shifted from below 30 km to about 30 km altitude. The magnitude of positive drag at these places also increases. At about 15 ° N and about 43 km, negative drag is also shifted upwards. These changes can be seen by comparing Fig. E.3a to Fig. E.3b. For July, comparison of Fig. E.4a and Fig. E.4b shows slight shifts in altitude of positive drag at $\sim$5 ° N, $\sim$23 km and negative drag at $\sim$5 ° S, $\sim$33 km altitude. The magnitude of positive drag at $\sim$5 ° N, $\sim$23 km increases slightly. In addition, the decrease in magnitude of positive drag from $\sim$40 to $\sim$45 km seems to indicate that this drag is shifted upwards. However, the data at altitudes higher than 45 km are not calculated in the current simulations.

Concerning simulated Q, comparison of Fig. E.3c and Fig. E.3d shows a decrease of vertical gradient at $\sim$5 ° S, $\sim$30 km altitude and an increase of vertical gradient at $\sim$15 ° S, 40-45 km altitudes. Also, the magnitude of vertical gradient at $\sim$15 ° N, 40-45 km altitudes increases. This is likely related to an upward shift of the vertical gradient. For July, similar features can also be found. A decrease of magnitude at $\sim$5 ° N, 23 km altitude and an increase of magnitude at $\sim$15 ° N, 40-45 km can be seen by comparing Fig. E.4c to Fig. E.4d.

Simulated P generally increases at the altitudes of higher than $\sim$25 km for both January and July. This can be seen by comparing Fig. E.3e to Fig. E.3f for January and by comparing Fig. E.4e to Fig. E.4f for July.

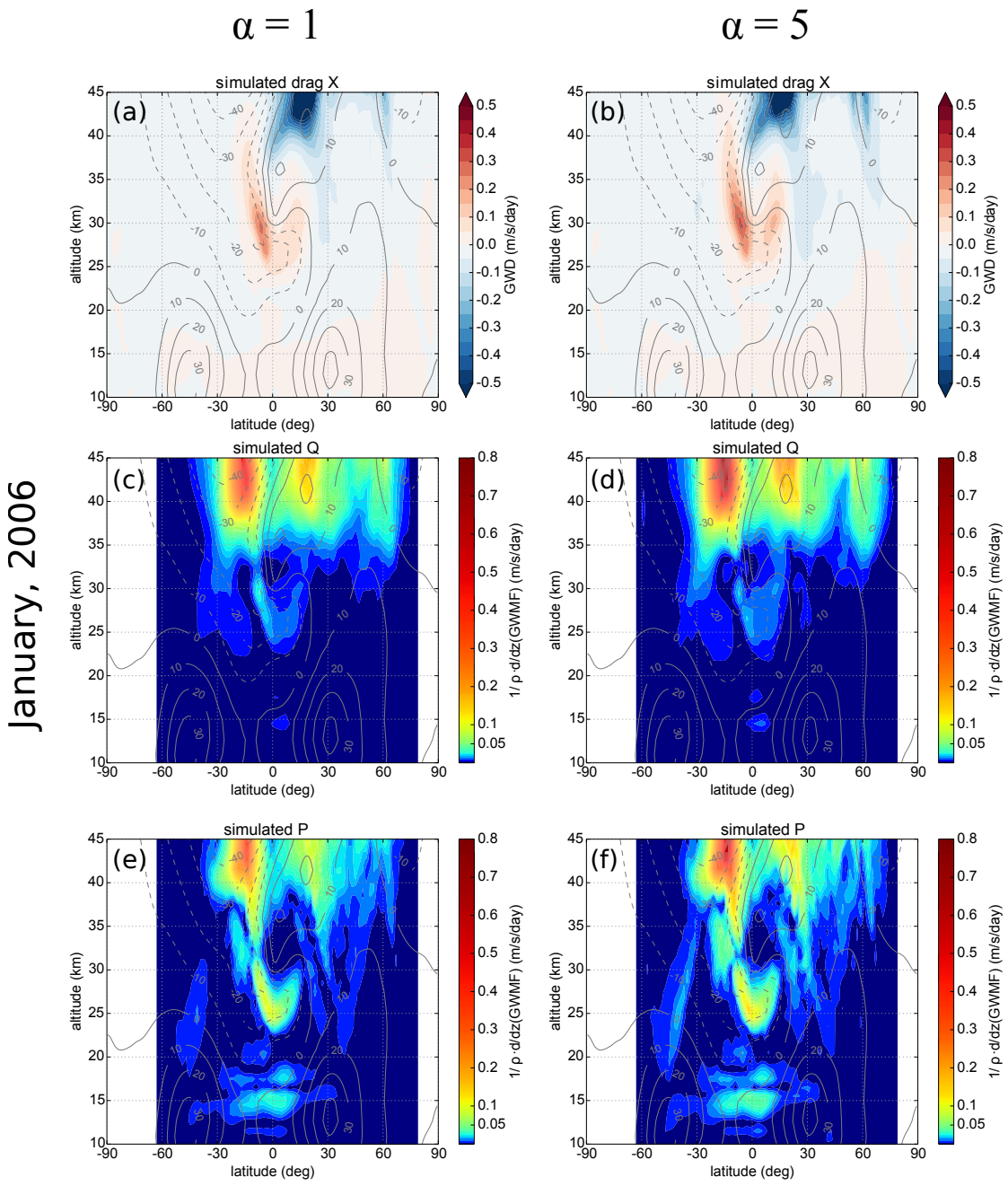

Figure E.3: Vertical gradients of GWMF for January 2006 for $\alpha = 1$ (left column) and $\alpha = 5$ (right column). The upper row shows zonal drag X, the middle row shows simulated Q and the lower row shows simulated P.

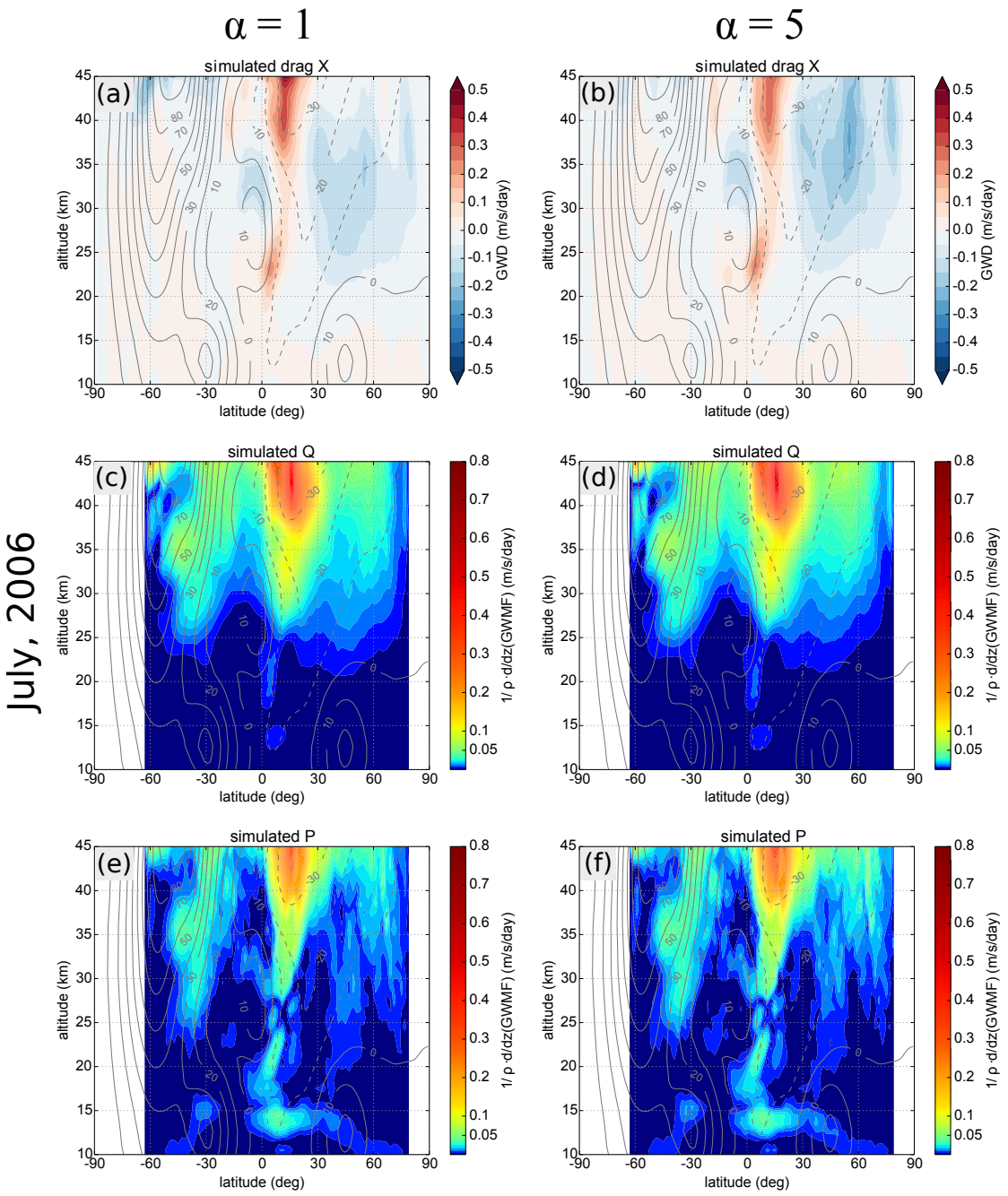

Figure E.4: Same as Fig. E.3 but for July 2006.

Acknowledgements

I would like to address my first thanks to my direct supervisor-Prof. Dr. Martin Riese for trusting and supporting me in this interesting research topic. I am very thankful for his helpful discussions about my scientific results as well as scientific papers to be published. Also, I would like to thank Prof. Dr. Martin Riese for always supporting me in learning German, with which I can understand German culture and enjoy life in Germany better, also adapt faster to our research group.

I am very grateful to my scientific supervisor-Dr. Peter Preuße for his support, scientific discussions, as well as his helpful comments on scientific papers. His creative ideas and opinions contributed a lot to this work.

I would like to address my sincere thank to Dr. Manfred Ern for regular scientific discussions, which help me to gain a lot of knowledge of the research topic. I am very thankful for his great work on observations of gravity waves from satellite instruments, based on which my simulations were compared to. Many thanks for his comments on my scientific papers.

Further thanks go to Dr. Silvio Kalisch for his frequent supports, scientific and non-scientific discussions.

Special thanks go again to Prof. Dr. Martin Riese, Dr. Peter Preuße, Dr. Manfred Ern, Dr. Martin Kaufmann, and Dr. Silvio Kalisch for helping me a lot with non-scientific issues since my very beginning time in Germany till now. Without their helps and advice, I would not be able to concentrate fully on my PhD.

I would like to express my sincere gratitude to all remaining colleagues from the IEK-7 at Forschungszentrum Jülich, who create and share a pleasure working environment.

I would like to acknowledge HITEC (Helmholtz Interdisciplinary Doctoral Training in Energy and Climate Research) graduate school for providing funding for my PhD studying.

Bibliography

Alexander, M. J. (1998), Interpretations of observed climatological patterns in stratospheric gravity wave variance, *J. Geophys. Res.*, *103*, 8627–8640.

Alexander, M. J. (2015), Global and seasonal variations in three-dimensional gravity wave momentum flux from satellite limb-sounding temperatures, *Geophys. Res. Lett.*, *42*(16), 6860–6867, doi:10.1002/2015GL065234.

Alexander, M. J., and D. A. Ortland (2010), Equatorial waves in High Resolution Dynamics Limb Sounder (HIRDLS) data, *J. Geophys. Res.*, *115*, D24111, doi:10.1029/2010JD014782.

Alexander, M. J., and L. Pfister (1995), Gravity wave momentum flux in the lower stratosphere over convection, *Geophys. Res. Lett.*, *22*(15), 2029–2032, doi:10.1029/95GL01984.

Alexander, M. J., and K. H. Rosenlof (1996), Nonstationary gravity wave forcing of the stratospheric zonal mean wind, *J. Geophys. Res.*, *101*(D18), 23,465–23,474.

Alexander, M. J., and K. H. Rosenlof (2003), Gravity-wave forcing in the stratosphere: Observational constraints from the upper atmosphere research satellite and implications for parameterization in global models, *J. Geophys. Res.*, *108*(D19), doi:10.1029/2003JD003373.

Alexander, M. J., and H. Teitelbaum (2007), Observation and analysis of a large amplitude mountain wave event over the Antarctic Peninsula, *J. Geophys. Res.*, *112*, D21103, doi:10.1029/2006JD008368.

Alexander, M. J., and H. Teitelbaum (2011), Three-dimensional properties of Andes mountain waves observed by satellite: A case study, *J. Geophys. Res. Atmos.*, *116*, doi:10.1029/2011JD016151.

Alexander, M. J., J. R. Holton, and D. R. Durran (1995), The gravity wave response above deep convection in a squall line simulation, *J. Atmos. Sci.*, *52*, 2212–2226.

Alexander, M. J., J. H. Beres, and L. Pfister (2000), Tropical stratospheric gravity wave activity and relationships to clouds, *J. Geophys. Res.*, *105*(D17), 22,299–22,309, doi:10.1029/2000JD900326.

Alexander, M. J., J. Gille, C. Cavanaugh, M. Coffey, C. Craig, V. Dean, T. Eden, G. Francis, C. Halvorson, J. Hannigan, R. Khosravi, D. Kinnison, H. Lee, S. Massie, and B. Nardi (2008), Global estimates of gravity wave momentum flux from High Resolution Dynamics Limb Sounder (HIRDLS) observations, *J. Geophys. Res.*, *113*, doi:10.1029/2007JD008807.

Alexander, M. J., S. D. Eckermann, D. Broutman, and J. Ma (2009), Momentum flux estimates for South Georgia Island mountain waves in the stratosphere observed via satellite, *Geophys. Res. Lett.*, *36*, doi:10.1029/2009GL038587.

Alexander, M. J., M. Geller, C. McLandress, S. Polavarapu, P. Preusse, F. Sassi, K. Sato, S. D. Eckermann, M. Ern, A. Hertzog, Y. Kawatani, M. Pulido, T. Shaw, M. Sigmond, R. Vincent, and S. Watanabe (2010), Recent developments in gravity wave effects in climate models, and the global distribution of gravity wave momentum flux from observations and models, *Q. J. Roy. Meteorol. Soc.*, *136*, 1103–1124, doi:10.1002/qj.637.

Allen, S. J., and R. A. Vincent (1995), Gravity wave activity in the lower atmosphere: Seasonal and latitudinal variations, *J. Geophys. Res.*, *100*, 1327–1350.

Alpers, M., R. Eixmann, C. Fricke-Begemann, M. Gerding, and J. Höffner (2004), Temperature lidar measurements from 1 to 105 km altitude using resonance, Rayleigh, and Rotational Raman scattering, *Atmos. Chem. Phys.*, *4*(3), 793–800, doi:10.5194/acp-4-793-2004.

Andrews, D. G., J. R. Holton, and C. B. Leovy (1987), *Middle Atmosphere Dynamics*, *International Geophysics Series*, vol. 40, Academic Press.

Arfken, G. B., and H. J. Weber (1995), *Mathematical Methods for Physicists*, 4th edition ed., 1029 pp., Academic Press, Boston.

Bailey, L. P., and J. C. Gille (1986), Inversion of limb radiance measurements: an operational algorithm, *J. Geophys. Res.*, *91*, 2757–2774.

Baumgarten, G. (2010), Doppler Rayleigh/Mie/Raman lidar for wind and temperature measurements in the middle atmosphere up to 80 km, *Atmos. Meas. Tech.*, *3*(6), 1509–1518, doi:10.5194/amt-3-1509-2010.

Belloul, M. B., and A. Hauchecorne (1997), Effect of periodic horizontal gradients on the retrieval of atmospheric profiles from occultation measurements, *Radio Sci.*, *32*(2), 469–478, doi:10.1029/96RS03599.

Beres, J. H., M. J. Alexander, and J. R. Holton (2002), Effects of tropospheric wind shear on the spectrum of convectively generated gravity waves, *J. Atmos. Sci.*, *59*(11), 1805–1824.

Beres, J. H., M. J. Alexander, and J. R. Holton (2004), A method of specifying the gravity wave spectrum above convection based on latent heating properties and background wind, *J. Atmos. Sci.*, *61*(3), 324–337.

Björn, L. (1984), The cold summer mesopause, *Adv. Space Res.*, *4*(4), 145–151, doi:10.1016/0273-1177(84)90277-1.

Boccara, G., A. Hertzog, R. A. Vincent, and F. Vial (2008), Estimation of gravity wave momentum flux and phase speeds from quasi-Lagrangian stratospheric balloon flights. Part I: Theory and simulations, *J. Atmos. Sci.*, *65*(10), 3042–3055, doi:10.1175/2008JAS2709.1.

Boer, G., and K. Hamilton (2008), QBO influence on extratropical predictive skill, *Clim. Dynam.*, *31*(7-8), 987–1000, doi:10.1007/s00382-008-0379-5.

Bosilovich, M. G., F. R. Robertson, and J. Chen (2011), Global energy and water budgets in MERRA, *J. Climate*, *24*(22), 5721–5739.

Brown, P. R. A. (1983), Aircraft measurements of mountain waves and their associated momentum flux over the British Isles, *Q. J. Roy. Meteorol. Soc.*, *109*(462), 849–865, doi:10.1002/qj.49710946211.

Burrage, M. D., R. A. Vincent, H. G. Mayr, W. R. Skinner, N. F. Arnold, and P. B. Hays (1996), Long-term variability in the equatorial middle atmosphere zonal wind, *J. Geophys. Res. Atmos.*, *101*(D8), 12,847–12,854, doi:10.1029/96JD00575.

Butchart, N., I. Cionni, V. Eyring, T. G. Shepherd, D. W. Waugh, H. Akiyoshi, J. Austin, C. Brühl, M. P. Chipperfield, E. Cordero, M. Dameris, R. Deckert, S. Dhomse, S. M. Frith, R. R. Garcia, A. Gettelman, M. A. Giorgetta, D. E. Kinnison, F. Li, E. Mancini, C. McLandress, S. Pawson, G. Pitari, D. A. Plummer, E. Rozanov, F. Sassi, J. F. Scinocca, K. Shibata, B. Steil, and W. Tian (2010), Chemistry-climate model simulations of twenty-first century stratospheric climate and circulation changes, *J. Climate*, *23*, 5349–5374, doi:10.1175/2010JCLI3404.1.

Carslaw, K. S., T. Peter, J. T. Bacmeister, and S. D. Eckermann (1999), Widespread solid particle formation by mountain waves in the Arctic stratosphere, *J. Geophys. Res.*, *104*(D1), 1827–1836.

Choi, H. J., and H. Y. Chun (2011), Momentum flux spectrum of convective gravity waves. Part I: An update of a parameterization using mesoscale simulation, *J. Atmos. Sci*, *68*, 739–759, doi:10.1175/2010JAS3552.1.

Choi, H.-J., H.-Y. Chun, and I.-S. Song (2009), Gravity wave temperature variance calculated using the ray-based spectral parameterization of convective gravity waves and its comparison with Microwave Limb Sounder observations, *J. Geophys. Res.*, *114*, D08111, doi:10.1029/2008JD011330.

Choi, H.-J., H.-Y. Chun, J. Gong, and D. L. Wu (2012), Comparison of gravity wave temperature variances from ray-based spectral parameterization of convective gravity wave drag with AIRS observations, *J. Geophys. Res.*, *117*, D05115, doi:10.1029/2011JD016900.

Chun, H.-Y., and J.-J. Baik (1998), Momentum flux by thermally induced internal gravity waves and its approximation for large-scale models, *J. Atmos. Sci.*, *55*, 3299–3310.

Chun, H.-Y., and J.-J. Baik (2002), An updated parameterization of convectively forced gravity wave drag for use in large-scale models, *J. Atmos. Sci.*, *59*(5), 1006–1017.

Chun, H.-Y., M.-D. Song, J.-W. Kim, and J.-J. Baik (2001), Effects of gravity wave drag induced by cumulus convection on the atmospheric general circulation, *J. Atmos. Sci.*, *58*(3), 302–319.

Chun, H.-Y., I.-S. Song, J.-J. Baik, and Y.-J. Kim (2004), Impact of a convectively forced gravity wave drag parameterization in NCAR CCM3, *J. Climate*, *17*, 3530–3547.

Clark, T. L., T. Hauf, and J. P. Kuettner (1986), Convectively forced internal gravity waves: Results from two-dimensional numerical experiments, *Q. J. Roy. Meteorol. Soc.*, *112*(474), 899–925, doi:10.1002/qj.49711247402.

de la Torre, A., and P. Alexander (1995), The interpretation of wavelengthsand periods as measured from atmospheric and periods as measured from atmospheric balloons, *J. Appl. Met.*, *34*(12), 2747–2754, doi:10.1175/1520-0450(1995)034<2747:TIOWAP>2.0.CO;2.

de la Torre, A., P. Alexander, and A. Giraldez (1999), The kinetic to potential energy ratio and spectral separability from high-resolution balloon soundings near the Andes mountains, *Geophys. Res. Lett.*, *26*(10), 1413–1416, doi: 10.1029/1999GL900265.

Dee, D. P., S. M. Uppala, A. J. Simmons, P. Berrisford, P. Poli, S. Kobayashi, U. Andrae, M. A. Balmaseda, G. Balsamo, P. Bauer, P. Bechtold, A. C. M. Beljaars, L. van de Berg, J. Bidlot, N. Bormann, C. Delsol, R. Dragani, M. Fuentes, A. J. Geer, L. Haimberger, S. B. Healy, H. Hersbach, E. V. Holm, L. Isaksen, P. Kallberg, M. Koehler, M. Matricardi, A. P. McNally, B. M. Monge-Sanz, J. J. Morcrette, B. K. Park, C. Peubey, P. de Rosnay, C. Tavolato, J. N. Thepaut, and F. Vitart (2011), The ERA-Interim reanalysis: configuration and performance of the data assimilation system, *Q. J. R. Meteorol. Soc.*, *137*(656, Part a), 553–597, doi:10.1002/qj.828.

Dewan, E. M., R. H. Picard, R. R. O'Neil, H. A. Gardiner, J. Gibson, J. D. Mill, E. Richards, M. Kendra, and W. O. Gallery (1998), MSX satellite observations of thunderstorm-generated gravity waves in mid-wave infrared images of the upper stratosphere, *Geophys. Res. Lett.*, *25*(7), 939–942.

Doyle, J. D., H. Volkert, A. Dörnbrack, K. P. Hoinka, and T. F. Hogan (2002), Aircraft measurements and numerical simulations of mountain waves over the

central Alps: A pre-MAP test case, *Q. J. Roy. Meteorol. Soc.*, *128*(584), 2175–2184, doi:10.1256/003590002320603601.

Dunkerton, T. J. (1982), Theory of the mesopause semiannual oscillation, *J. Atmos. Sci.*, *39*(12), 2681–2690.

Dunkerton, T. J. (1984), Inertia gravity waves in the stratosphere, *J. Atmos. Sci.*, *41*, 3396–3404.

Dunkerton, T. J. (1997), The role of gravity waves in the quasi-biennial oscillation, *J. Geophys. Res.*, *102*, 26,053–26,076.

Ebdon, R. A. (1975), The quasi-biennial oscillation and its association with tropospheric circulation patterns, *Meteorol. Mag.*, *104*, 282–297.

Eckermann, S. D. (1996), Hodographic analysis of gravity waves: Relationships among Stokes parameters, rotary spectra and cross-spectral methods, *J. Geophys. Res.*, *101*, 169–174.

Eckermann, S. D., and C. J. Marks (1997), GROGRAT: a new model of the global propagation and dissipation of atmospheric gravity waves, *Adv. Space Res.*, *20*, 1253–1256.

Eckermann, S. D., and R. A. Vincent (1989), Falling sphere observations of anisotropic gravity wave motions in the upper stratosphere over Australia, *Pure Appl. Geophys.*, *130*, 509–532.

Eckermann, S. D., and D. L. Wu (2006), Imaging gravity waves in lower stratospheric AMSU-A radiances, Part 1: simple forward model, *Atmos. Chem. Phys.*, *6*, 3325–3341, doi:10.5194/acp-6-3325-2006.

Eckermann, S. D., I. Hirota, and W. K. Hocking (1995), Gravity wave and equatorial wave morphology of the stratosphere derived from long-term rocket soundings, *Q. J. Roy. Meteorol. Soc.*, *121*(521), 149–186.

Eckermann, S. D., D. L. Wu, J. D. Doyle, J. F. Burris, T. J. McGee, C. A. Hostetler, L. Coy, B. N. Lawrence, A. Stephens, J. P. McCormack, and T. F. Hogan (2006), Imaging gravity waves in lower stratospheric AMSU-A radiances, Part 2: validation case study, *Atmos. Chem. Phys.*, *6*, 3343–3362, doi:10.5194/acp-6-3343-2006.

Eckermann, S. D., J. Ma, D. L. Wu, and D. Broutman (2007), A three-dimensional mountain wave imaged in satellite radiance throughout the stratosphere: Evidence of the effects of directional wind shear, *Q. J. Roy. Meteorol. Soc.*, *133*(629), 1959–1975, doi:10.1002/qj.187.

Ern, M., and P. Preusse (2009), Quantification of the contribution of equatorial Kelvin waves to the QBO wind reversal in the stratosphere, *Geophys. Res. Lett.*, *36*, L21801, doi:10.1029/2009GL040493.

Ern, M., and P. Preusse (2012), Gravity wave momentum flux spectra observed from satellite in the summertime subtropics: Implications for global modeling, *Geophys. Res. Lett.*, *39*, L15810, doi:10.1029/2012GL052659.

Ern, M., P. Preusse, M. J. Alexander, and C. D. Warner (2004), Absolute values of gravity wave momentum flux derived from satellite data, *J. Geophys. Res.*, *109*, doi:10.1029/2004JD004752.

Ern, M., P. Preusse, and C. D. Warner (2005), A comparison between CRISTA satellite data and Warner and McIntyre gravity wave parameterization scheme: horizontal and vertical wavelength filtering of gravity wave momentum flux, *Adv. Space Res.*, *35*(11), 2017–2023, doi:10.1016/j.asr.2005.04.109.

Ern, M., P. Preusse, and C. D. Warner (2006), Some experimental constraints for spectral parameters used in the Warner and McIntyre gravity wave parameterization scheme, *Atmos. Chem. Phys.*, *6*, 4361–4381.

Ern, M., P. Preusse, M. Krebsbach, M. G. Mlynczak, and J. M. Russell III (2008), Equatorial wave analysis from SABER and ECMWF temperatures, *Atmos. Chem. Phys.*, *8*, 845–869.

Ern, M., P. Preusse, J. C. Gille, C. L. Hepplewhite, M. G. Mlynczak, J. M. Russell III, and M. Riese (2011), Implications for atmospheric dynamics derived from global observations of gravity wave momentum flux in stratosphere and mesosphere, *J. Geophys. Res.*, *116*, D19107, doi:10.1029/2011JD015821.

Ern, M., P. Preusse, S. Kalisch, M. Kaufmann, and M. Riese (2013), Role of gravity waves in the forcing of quasi two-day waves in the mesosphere: An observational study, *J. Geophys. Res. Atmos.*, *118*(9), 3467–3485, doi:10.1029/2012JD018208.

Ern, M., F. Ploeger, P. Preusse, J. C. Gille, L. J. Gray, S. Kalisch, M. G. Mlynczak, J. M. Russell, and M. Riese (2014), Interaction of gravity waves with the QBO: A satellite perspective, *J. Geophys. Res. Atmos.*, *119*(5), 2329–2355, doi:10.1002/2013JD020731.

Ern, M., P. Preusse, and M. Riese (2015), Driving of the SAO by gravity waves as observed from satellite, *Ann. Geophys.*, *33*(4), 483–504, doi:10.5194/angeo-33-483-2015.

Evan, S., M. J. Alexander, and J. Dudhia (2012), WRF simulations of convectively generated gravity waves in opposite QBO phases, *J. Geophys. Res.*, *117*, D12117, doi:10.1029/2011JD017302.

Faber, A., P. Llamedo, T. Schmidt, A. de la Torre, and J. Wickert (2013), On the determination of gravity wave momentum flux from GPS radio occultation data, *Atmos. Meas. Tech.*, *6*, 3169–3180, doi:10.5194/amt-6-3169-2013.

Fetzer, E. J., and J. C. Gille (1994), Gravity wave variances in LIMS temperatures. Part I: Variability and comparison with background winds, *J. Atmos. Sci.*, *51*, 2461–2483.

Fovell, R., D. Durran, and J. R. Holton (1992), Numerical simulations of convectively generated stratospheric gravity waves, *J. Atmos. Sci.*, *49*, 1427–1442.

Fritts, D., and M. Alexander (2003), Gravity wave dynamics and effects in the middle atmosphere, *Rev. Geophys.*, *41*(1), doi:10.1029/2001RG000106.

Fritts, D. C., and P. K. Rastogi (1985), Convective and dynamical instabilities due to gravity wave motions in the lower and middle atmosphere: theory and observations, *Radio Sci.*, *20*, 1247–1277.

Garcia, R. R., and W. J. Randel (2008), Acceleration of the Brewer-Dobson circulation due to increases in greenhouse gases, *J. Atmos. Sci.*, *65*(8), 2731–2739, doi:10.1175/2008JAS2712.1.

Garcia, R. R., and M. L. Salby (1987), Transient response to localized episodic heating in the tropics. Part II: Far-field behavior, *J. Atmos. Sci.*, *44*(2), 499–532.

Garcia, R. R., and S. Solomon (1985), The effect of breaking gravity waves on the dynamics and chemical composition of the mesosphere and lower thermosphere, *J. Geophys. Res.*, *90*, 3850–3868.

Gardner, C. S., M. Coble, G. C. Papen, and G. R. Swenson (1996), Observations of the unambiguous 2-dimensional horizontal wave number spectrum of OH intensity perturbations, *Geophys. Res. Lett.*, *23*(25), 3739–3742, doi:10.1029/96GL03158.

Geller, M. A., and J. Gong (2010), Gravity wave kinetic, potential, and vertical fluctuation energies as indicators of different frequency gravity waves, *J. Geophys. Res.*, *115*(D11), 1–8.

Geller, M. A., M. J. Alexander, P. T. Love, J. Bacmeister, M. Ern, A. Hertzog, E. Manzini, P. Preusse, K. Sato, A. A. Scaife, and T. Zhou (2013), A comparison between gravity wave momentum fluxes in observations and climate models, *J. Climate*, *26*(17), 6383–6405, doi:10.1175/JCLI-D-12-00545.1.

Gerding, M., J. Höffner, J. Lautenbach, M. Rauthe, and F.-J. Lübken (2008), Seasonal variation of nocturnal temperatures between 1 and 105 km altitude at 54 °N observed by lidar, *Atmos. Chem. Phys.*, *8*(24), 7465–7482, doi:10.5194/acp-8-7465-2008.

Gill, A. E. (1982), *Atmosphere-ocean Dynamics*, Academic Press.

Gille, J., J. Barnett, P. Arter, M. Barker, P. Bernath, C. Boone, C. Cavanaugh, J. Chow, M. Coffey, J. Craft, C. Craig, M. Dials, V. Dean, T. Eden, D. P. Edwards, G. Francis, C. Halvorson, L. Harvey, C. Hepplewhite, R. Khosravi, D. Kinnison, C. Krinsky, A. Lambert, H. Lee, L. Lyjak, J. Loh, W. Mankin, S. Massie, J. McInerney, J. Moorhouse, B. Nardi, D. Packman, C. Randall, J. Reburn, W. Rudolf, M. Schwartz, J. Serafin, K. Stone, B. Torpy, K. Walker, A. Waterfall, R. Watkins, J. Whitney, D. Woodard, and G. Young (2008), High Resolution Dynamics Limb Sounder: Experiment overview, recovery, and validation of initial temperature data, *J. Geophys. Res. Atmos.*, *113*(D16), doi: 10.1029/2007JD008824.

Gille, J. C., and J. M. Russell (1984), The limb infrared monitor of the stratosphere - experiment description, performance and results, *J. Geophys. Res.*, *89*, 5125–5140.

Gille, J. C., J. J. Barnett, J. G. Whitney, M. A. Dials, D. Woodard, W. P. Rudolf, A. Lambert, and W. Mankin (2003), The High-Resolution Dynamics Limb Sounder (HIRDLS) experiment on AURA, *Proceedings of SPIE*, *5152*, 161–171.

Gong, J., D. L. Wu, and S. D. Eckermann (2012), Gravity wave variances and propagation derived from AIRS radiances, *Atmos. Chem. Phys*, *12*(4), 1701–1720, doi:10.5194/acp-12-1701-2012.

Gong, J., M. A. Geller, and L. Wang (2008), Source spectra information derived from US high-resolution radiosonde data, *J. Geophys. Res. Atmos.*, *113*(D10), doi:10.1029/2007JD009252.

Gordley, L. L., B. T. Marshall, and D. A. Chu (1994), LINEPAK: Algorithms for modeling spectral transmittance and radiance, *J. Quant. Spectrosc. Radiat. Transfer*, *52*, 563–580.

Gray, L. J., and J. A. Pyle (1986), The semi-annual oscillation and equatorial tracer distributions, *Q. J. Roy. Meteorol. Soc.*, *112*(472), 387–407, doi: 10.1002/qj.49711247207.

Grimsdell, A. W., M. J. Alexander, P. T. May, and L. Hoffmann (2010), Model study of waves generated by convection with direct validation via satellite, *J. Atmos. Sci.*, *67*(5), 1617–1631, doi:10.1175/2009JAS3197.1.

Hamilton, K., R. John Wilson, J. D. Mahlman, and L. J. Umscheid (1995), Climatology of the SKYHI Troposphere–Stratosphere–Mesosphere General Circulation Model, *J. Atmos. Sci.*, *52*(1), 5–43.

Hapgood, M. A., and M. J. Taylor (1982), Analysis of airglow image data, *Ann. Geophys.*, *38*, 805–813.

Haque, R., and G. R. Swenson (1999), Extraction of motion parameters of gravity-wave structures from all-sky OH image sequences, *Appl. Optics*, *38*, 4433–4442.

Hasha, A., O. Bühler, and J. Scinocca (2008), Gravity wave refraction by three-dimensionally varying winds and the global transport of angular momentum, *J. Atmos. Sci.*, *65*, 2892–2906.

Hertzog, A., G. Boccara, R. A. Vincent, F. Vial, and P. Cocquerez (2008), Estimation of gravity wave momentum flux and phase speeds from quasi-Lagrangian stratospheric balloon flights. Part II: Results from the Vorcore campaign in Antarctica, *J. Atmos. Sci.*, *65*(10), 3056–3070, doi:10.1175/2008JAS2710.1.

Hitchman, M. H., and C. B. Leovy (1988), Estimation of the Kelvin wave contribution to the semiannual oscillation, *J. Atmos. Sci.*, *45*(9), 1462–1475.

Hocking, W. K. (1997), Strengths and limitations of MST radar measurements of middle-atmosphere winds, *Ann. Geophys.*, *15*(9), 1111–1122, doi:10.1007/s00585-997-1111-1.

Hoffmann, L., and M. J. Alexander (2009), Retrieval of stratospheric temperatures from Atmospheric Infrared Sounder radiance measurements for gravity wave studies, *J. Geophys. Res.*, *114*, doi:10.1029/2008JD011241.

Hoffmann, P., A. Serafimovich, D. Peters, P. Dalin, R. Goldberg, and R. Latteck (2006), Inertia gravity waves in the upper troposphere during the MaCWAVE winter campaign - Part I: Observations with collocated radars, *Ann. Geophys.*, *24*(11), 2851–2862, doi:10.5194/angeo-24-2851-2006.

Holton, J. R. (1982), The role of gravity wave induced drag and diffusion on the momentum budget of the mesosphere, *J. Atmos. Sci.*, *39*(4), 791–799.

Holton, J. R., and H.-C. Tan (1980), The influence of the equatorial quasi-biennial oscillation on the global circulation at 50 mb, *J. Atmos. Sci.*, *37*(10), 2200–2208.

Huang, F. T., H. G. Mayr, C. A. Reber, J. M. Russell, M. G. Mlynczak, and J. G. Mengel (2008), Ozone quasi-biennial oscillations (QBO), semiannual oscillations (SAO), and correlations with temperature in the mesosphere, lower thermosphere, and stratosphere, based on measurements from SABER on TIMED and MLS on UARS, *J. Geophys. Res.*, *113*(A1), doi:10.1029/2007JA012634.

Isler, J. R., M. J. Taylor, and D. C. Fritts (1997), Observational evidence of wave ducting and evanescence in the mesosphere, *J. Geophys. Res. Atmos.*, *102*(D22), 26,301–26,313, doi:10.1029/97JD01783.

Jewtoukoff, V., R. Plougonven, and A. Hertzog (2013), Gravity waves generated by deep tropical convection: Estimates from balloon observations and mesoscale simulations, *J. Geophys. Res. Atmos.*, *118*(17), 9690–9707, doi:10.1002/jgrd.50781.

Jia, J. Y., P. Preusse, M. Ern, H.-Y. Chun, J. C. Gille, S. D. Eckermann, and M. Riese (2014), Sea surface temperature as a proxy for convective gravity wave excitation: a study based on global gravity wave observations in the middle atmosphere, *Ann. Geophys.*, *32*(11), 1373–1394, doi:10.5194/angeo-32-1373-2014.

Jiang, J., B. Wang, K. Goya, K. Hocke, S. Eckermann, J. Ma, D. Wu, and W. Read (2004a), Geographical distribution and interseasonal variability of tropical deep convection: UARS MLS observations and analyses, *J. Geophys. Res. Atmos.*, *109*, D03111, doi:10.1029/2003JD003756.

Jiang, J., S. Eckermann, D. Wu, and J. Ma (2004b), A search for mountain waves in MLS stratospheric limb radiances from the winter Northern Hemisphere: Data analysis and global mountain wave modeling, *J. Geophys. Res. Atmos.*, *109*(D3), doi:10.1029/2003JD003974.

Jiang, J. H., S. D. Eckermann, D. L. Wu, and D. Y. Wang (2006), Inter-annual variation of gravity waves in the Arctic and Antarctic winter middle atmosphere, *Adv. Space Res.*, *38*(11), 2418–2423, doi:10.1016/j.asr.2005.09.036.

Kalisch, S. (2014), Three-dimensional ray-tracing simulations of convective gravity waves, Ph.D. thesis, University of Wuppertal.

Kalisch, S., P. Preusse, M. Ern, S. D. Eckermann, and M. Riese (2014), Differences in gravity wave drag between realistic oblique and assumed vertical propagation, *J. Geophys. Res. Atmos.*, *119*, 10,081–10,099, doi:10.1002/2014JD021779.

Karoly, D. J., G. L. Roff, and M. J. Reeder (1996), Gravity wave activity associated with tropical convection detected in TOGA COARE Sounding data, *Geophys. Res. Lett.*, *23*(3), 261–264, doi:10.1029/96GL00023.

Kershaw, R. (1995), Parametrization of momentum transport by convectively generated gravity waves, *Q. J. Roy. Meteorol. Soc.*, *121*(525), 1023–1040, doi:10.1002/qj.49712152505.

Khosrawi, F., R. Müller, J. Urban, M. H. Proffitt, G. Stiller, M. Kiefer, S. Lossow, D. Kinnison, F. Olschewski, M. Riese, and D. Murtagh (2013), Assessment of the interannual variability and influence of the QBO and upwelling on tracer–tracer distributions of N_2O and O_3 in the tropical lower stratosphere, *Atmos. Chem. Phys.*, *13*(7), 3619–3641, doi:10.5194/acp-13-3619-2013.

Khouider, B., and M. W. Moncrieff (2015), Organized convection parameterization for the ITCZ, *J. Atmos. Sci.*, *72*(8), 3073–3096, doi:10.1175/JAS-D-15-0006.1.

Kilpatrick, T. J., and S.-P. Xie (2015), ASCAT observations of downdrafts from mesoscale convective systems, *Geophys. Res. Lett.*, *42*(6), 1951–1958, doi:10.1002/2015GL063025.

Kim, J.-E., and M. J. Alexander (2013), Tropical precipitation variability and convectively coupled equatorial waves on submonthly time scales in reanalyses and TRMM, *J. Climate*, *26*(10), 3013–3030, doi:10.1175/JCLI-D-12-00353.1.

Kim, S.-Y., H.-Y. Chun, and J.-J. Baik (2007), Sensitivity of typhoon-induced gravity waves to cumulus parameterizations, *Geophys. Res. Lett.*, *34*, L15814, doi:10.1029/2007GL030592.

Kim, Y.-J., S. D. Eckermann, and H.-Y. Chun (2003), An overview of the past, present and future of gravity-wave drag parameterization for numerical climate and weather prediction models - survey article, *Atmos.-Ocean*, *41*, 65–98, doi: 10.3137/ao.410105.

Lane, T. P., M. J. Reeder, and T. L. Clark (2001), Numerical modeling of gravity wave generation by deep tropical convection, *J. Atmos. Sci.*, *58*(10), 1249–1274.

Lange, M., and C. Jacobi (2003), Analysis of gravity waves from radio occultation measurements, *Springer Berlin*, pp. 479–484.

Li, F., J. Austin, and J. Wilson (2008), The strength of the Brewer-Dobson circulation in a changing climate: Coupled chemistry-climate model simulations, *J. Climate*, *21*, 40–57, doi:10.1175/2007JCLI1663.1.

Lighthill, M. J. (1967), Waves in fluids, *Comm. Pure Appl. Math.*, *20*(2), 267–293, doi:10.1002/cpa.3160200204.

Lindzen, R. S. (1981), Turbulence and stress owing to gravity wave and tidal breakdown, *J. Geophys. Res.*, *86*, 9707–9714.

Liu, C., and E. J. Zipser (2015), The global distribution of largest, deepest, and most intense precipitation systems, *Geophys. Res. Lett.*, *42*(9), 3591–3595, doi: 10.1002/2015GL063776.

Marks, C. J., and S. D. Eckermann (1995), A three-dimensional nonhydrostatic ray-tracing model for gravity waves: formulation and preliminary results for the middle atmosphere, *J. Atmos. Sci.*, *52*, 1959–1984.

Marsh, A., N. Mitchell, and L. Thomas (1991), Lidar studies of stratospheric gravity-wave spectra, *Planet. Space Sci.*, *39*(11), 1541–1548, doi:10.1016/0032-0633(91)90081-K.

Marshall, A. G., and A. A. Scaife (2009), Impact of the QBO on surface winter climate, *J. Geophys. Res. Atmos.*, *114*(D18), D18110, doi:10.1029/2009JD011737.

Marshall, B. T., L. L. Gordley, and D. A. Chu (1994), BANDPAK: Algorithms for modeling broadband transmission and radiance, *J. Quant. Spectrosc. Radiat. Transfer*, *52*, 581–599.

Matsuno, T. (1982), A quasi one-dimensional model of the middle atmosphere circulation interacting with internal gravity waves, *J. Met. Soc. Japan*, *60*, 215–226.

McDonald, A. J., S. E. George, and R. M. Woollands (2009), Can gravity waves significantly impact PSC occurrence in the Antarctic?, *Atmos. Chem. Phys.*, *9*, 8825–8840, doi:10.5194/acp-9-8825-2009.

McIntyre, M. E. (1998), Breaking waves and global scale chemical transport in the Earth's atmosphere, with spinoffs for the Sun's interior, *Prog. of Theor. Phys.*, *130*, 137–166.

McLandress, C. (1998), On the importance of gravity waves in the middle atmosphere and their parameterization in general circulation models, *J. Atmos. Terr. Phys.*, *60*, 1357–1383.

McLandress, C., and T. G. Shepherd (2009), Simulated anthropogenic changes in the Brewer-Dobson circulation, including its extension to high latitudes, *J. Climate*, *22*, 1516–1540, doi:10.1175/2008JCLI2679.1.

McLandress, C., M. J. Alexander, and D. L. Wu (2000), Microwave Limb Sounder observations of gravity waves in the stratosphere: A climatology and interpretation, *J. Geophys. Res.*, *105*(D9), 11,947–11,967.

Mlynczak, M. G. (1997), Energetics of the mesosphere and lower thermosphere and the SABER experiment, *Adv. Space Res.*, *20*, 1177–1183.

Nakamura, T., T. Tsuda, M. Yamamoto, S. Fukao, and S. Kato (1993), Characteristics of gravity waves in the mesosphere observed with the middle and upper atmosphere radar: 1. momentum flux, *J. Geophys. Res. Atmos.*, *98*(D5), 8899–8910, doi:10.1029/92JD02978.

Nash, J., R. Smout, T. Oakley, and S. Kurnosenko (2005), WMO intercomparison of high quality radiosonde systems: Final report, *Tech. rep.*, WMO Report.

Nastrom, G. D., D. C. Fritts, and K. S. Gage (1987), An investigation of terrain effects on the mesoscale spectrum of atmospheric motions, *J. Atmos. Sci.*, *44*(20), 3087–3096.

Newton, C. W. (1960), *Hydrodynamic interactions with ambient wind field as a factor in cumulus development*, Pergamon Press, New York.

Orr, A., P. Bechtold, J. Scinocca, M. Ern, and M. Janiskova (2010), Improved middle atmosphere climate and forecasts in the ECMWF model through a nonorographic gravity wave drag parameterization, *J. Climate*, *23*, 5905–5926.

Osprey, S. M., L. J. Gray, S. C. Hardiman, N. Butchart, A. C. Bushell, and T. J. Hinton (2010), The climatology of the middle atmosphere in a vertically extended version of the Met Office's climate model. Part II: Variability, *J. Atmos. Sci.*, *67*(11), 3637–3651.

Pascoe, C. L., L. J. Gray, and A. A. Scaife (2006), A GCM study of the influence of equatorial winds on the timing of sudden stratospheric warmings, *Geophys. Res. Lett.*, *33*(6), L06825, doi:10.1029/2005GL024715.

Peña-Ortiz, C., H. Schmidt, M. A. Giorgetta, and M. Keller (2010), QBO modulation of the semiannual oscillation in MAECHAM5 and HAMMONIA, *J. Geophys. Res. Atmos.*, *115*(D21), D21106, doi:10.1029/2010JD013898.

Pfister, L., W. Starr, R. Craig, M. Loewenstein, and M. Legg (1986), Small-scale motions observed by aircraft in the tropical lower stratosphere: Evidence for mixing and its relationship to large-scale flows, *J. Atmos. Sci.*, *43*(24), 3210–3225.

Pfister, L., K. R. Chan, T. P. Bui, S. Bowen, M. Legg, B. Gary, K. Kelly, M. Proffitt, and W. Starr (1993a), Gravity waves generated by a tropical cyclone during the step tropical field program: A case study, *J. Geophys. Res. Atmos.*, *98*(D5), 8611–8638, doi:10.1029/92JD01679.

Pfister, L., S. Scott, M. Loewenstein, S. Bowen, and M. Legg (1993b), Mesoscale disturbances in the tropical stratosphere excited by convection: Observations and effects on the stratospheric momentum budget, *J. Atmos. Sci.*, *50*(8), 1058–1075.

Piani, C., D. Durran, M. J. Alexander, and J. R. Holton (2000), A numerical study of three-dimensional gravity waves triggered by deep tropical convection and their role in the dynamics of the QBO, *J. Atmos. Sci.*, *57*(22), 3689–3702.

Pitteway, M. L. V., and C. O. Hines (1963), The viscous damping of atmospheric gravity waves, *Can. J. Phys.*, *41*(12), 1935–1948, doi:10.1139/p63-194.

Plougonven, R., A. Hertzog, and M. J. Alexander (2015), Case studies of nonorographic gravity waves over the Southern Ocean emphasize the role of moisture, *J. Geophys. Res. Atmos.*, *120*(4), 1278–1299, doi:10.1002/2014JD022332, 2014JD022332.

Plougonven, R., A. Hertzog, and H. Teitelbaum (2008), Observations and simulations of a large-amplitude mountain wave breaking over the Antarctic Peninsula, *J. Geophys. Res. Atmos.*, *113*(D16), doi:10.1029/2007JD009739.

Plougonven, R., A. Hertzog, and L. Guez (2013), Gravity waves over Antarctica and the Southern Ocean: consistent momentum fluxes in mesoscale simulations and stratospheric balloon observations, *Q. J. Roy. Meteorol. Soc.*, *139*(670, A), 101–118, doi:10.1002/qj.1965.

Preusse, P. (2001), Satellitenmessungen von schwerewellen in der mittleren atmosphäre mit CRISTA, Ph.D. thesis, University of Wuppertal.

Preusse, P., and M. Ern (2005), Indication of convectively generated gravity waves observed by CLAES, *Adv. Space Res.*, *35*, 1987–1991, doi: 10.1016/j.asr.2004.09.005.

Preusse, P., B. Schaeler, J. Bacmeister, and D. Offermann (1999), Evidence for gravity waves in CRISTA temperatures, *Adv. Space Res.*, *24*, 1601–1604.

Preusse, P., S. D. Eckermann, and D. Offermann (2000), Comparison of global distributions of zonal-mean gravity wave variance inferred from different satellite instruments, *Geophys. Res. Lett.*, *27*(23), 3877–3880.

Preusse, P., S. Eckermann, J. Oberheide, M. Hagan, and D. Offermann (2001), Modulation of gravity waves by tides as seen in CRISTA temperatures, *Adv. Space Res.*, *27*(10), 1773 – 1778, doi:10.1016/S0273-1177(01)00336-2.

Preusse, P., A. Dörnbrack, S. D. Eckermann, M. Riese, B. Schaeler, J. T. Bacmeister, D. Broutman, and K. U. Grossmann (2002), Space-based measurements of stratospheric mountain waves by CRISTA, 1. sensitivity, analysis method, and a case study, *J. Geophys. Res.*, *107*, doi:10.1029/2001JD000699.

Preusse, P., S. D. Eckermann, M. Ern, F. J. Schmidlin, M. J. Alexander, and D. Offermann (2003), Infrared limb sounding measurements of middle atmosphere gravity waves by CRISTA, *SPIE proceedings*, *4882*, 134–148.

Preusse, P., M. Ern, S. D. Eckermann, C. D. Warner, R. H. Picard, P. Knieling, M. Krebsbach, J. M. Russel III, M. G. Mlynczak, C. J. Mertens, and M. Riese (2006), Tropopause to mesopause gravity waves in August: measurement and modeling, *J. Atmos. Solar-Terr. Phys.*, *68*, 1730–1751.

Preusse, P., S. D. Eckermann, and M. Ern (2008), Transparency of the atmosphere to short horizontal wavelength gravity waves, *J. Geophys. Res.*, *113*(D24), doi: 10.1029/2007JD009682.

Preusse, P., S. D. Eckermann, M. Ern, J. Oberheide, R. H. Picard, R. G. Roble, M. Riese, J. M. Russell III, and M. G. Mlynczak (2009a), Global ray tracing simulations of the SABER gravity wave climatology, *J. Geophys. Res.*, *114*, doi:10.1029/2008JD011214.

Preusse, P., S. Schroeder, L. Hoffmann, M. Ern, F. Friedl-Vallon, J. Ungermann, H. Oelhaf, H. Fischer, and M. Riese (2009b), New perspectives on gravity wave remote sensing by spaceborne infrared limb imaging, *Atmos. Meas. Tech.*, *2*, 299–311.

Preusse, P., L. Hoffmann, C. Lehmann, M. J. Alexander, D. Broutman, H.-Y. Chun, A. Dudhia, A. Hertzog, M. Höpfner, Y.-H. Kim, W. Lahoz, J. Ma, M. Pulido, M. Riese, H. Sembhi, S. Wüst, V. Alishahi, M. Bittner, M. Ern, P. G. Fogli, S.-Y. Kim, V. Kopp, M. Lucini, E. Manzini, J. C. McConnell, J. Ruiz, G. Scheffler, K. Semeniuk, V. Sofieva, and F. Vial (2012), Observation

of gravity waves from space, *Final report, ESA study, CN/22561/09/NL/AF*, pp 195.

Preusse, P., M. Ern, P. Bechtold, S. D. Eckermann, S. Kalisch, Q. T. Trinh, and M. Riese (2014), Characteristics of gravity waves resolved by ECMWF, *Atmos. Chem. Phys.*, *14*(19), 10,483–10,508, doi:10.5194/acp-14-10483-2014.

Punge, H. J., P. Konopka, M. A. Giorgetta, and R. Müller (2009), Effects of the quasi-biennial oscillation on low-latitude transport in the stratosphere derived from trajectory calculations, *J. Geophys. Res.*, *114*(D3), D03102, doi:10.1029/2008JD010518.

Rauthe, M., M. Gerding, and F.-J. Lübken (2008), Seasonal changes in gravity wave activity measured by lidars at mid-latitudes, *Atmos. Chem. Phys.*, *8*(22), 6775–6787, doi:10.5194/acp-8-6775-2008.

Remsberg, E. E., B. T. Marshall, M. Garcia-Comas, D. Krueger, G. S. Lingenfelser, J. Martin-Torres, M. G. Mlynczak, J. M. Russell III, A. K. Smith, Y. Zhao, C. Brown, L. L. Gordley, M. J. Lopez-Gonzalez, M. Lopez-Puertas, C. Y. She, M. J. Taylor, and R. E. Thompson (2008), Assessment of the quality of the version 1.07 temperature-versus-pressure profiles of the middle atmosphere from TIMED/SABER, *J. Geophys. Res.*, *113*, doi:10.1029/2008JD010013.

Ricciardulli, L., and R. R. Garcia (2000), The excitation of equatorial waves by deep convection in the NCAR community climate model (CCM3), *J. Atmos. Sci.*, *57*, 3461–3487, doi:10.1175/1520-0469(2000)057<3461:TEOEWB>2.0.CO;2.

Rienecker, M. M., M. J. Suarez, R. Gelaro, R. Todling, J. Bacmeister, E. Liu, M. G. Bosilovich, S. D. Schubert, L. Takacs, G.-K. Kim, S. Bloom, J. Chen, D. Collins, A. Conaty, A. da Silva, W. Gu, J. Joiner, R. D. Koster, R. Lucchesi, A. Molod, T. Owens, S. Pawson, P. Pegion, C. R. Redder, R. Reichle, F. R. Robertson, A. G. Ruddick, M. Sienkiewicz, and J. Woollen (2011), MERRA: NASA's Modern-Era Retrospective Analysis for Research and Applications, *J. Climate*, *24*(14), 3624–3648, doi:10.1175/JCLI-D-11-00015.1.

Riese, M., R. Spang, P. Preusse, M. Ern, M. Jarisch, D. Offermann, and K. U. Grossmann (1999), Cryogenic Infrared Spectrometers and Telescopes for the Atmosphere (CRISTA) data processing and atmospheric temperature and trace gas retrieval, *J. Geophys. Res.*, *104*, 16,349–16,367, doi:10.1029/1998JD100057.

Riese, M., F. Friedl-Vallon, R. Spang, P. Preusse, C. Schiller, L. Hoffmann, P. Konopka, H. Oelhaf, T. von Clarmann, and M. Höpfner (2005), GLObal limb Radiance Imager for the Atmosphere (GLORIA): Scientific objectives, *Adv. Space Res.*, *36*, 989–995, doi:10.1016/j.asr.2005.04.115.

Rind, D., R. Suozzo, N. K. Balachandran, A. Lacis, and G. Russell (1988), The GISS global climate-middle atmosphere model. Part I: Model structure and climatology, *J. Atmos. Sci.*, *45*(3), 329–370, doi:10.1175/1520-0469(1988)045<0329:TGGCMA>2.0.CO;2.

Rosenlof, K. H. (1996), Summer hemisphere differences in temperature and transport in the lower stratosphere, *J. Geophys. Res. Atmos.*, *101*(D14), 19,129–19,136, doi:10.1029/96JD01542.

Russell III, J. M., M. G. Mlynczak, L. L. Gordley, J. Tansock, and R. Esplin (1999), An overview of the SABER experiment and preliminary calibration results, *Proceeding SPIE*, (3756), 277–288, doi:10.1117/12.366382.

Salby, M. L. (1982), Sampling theory for asynoptic satellite observations. Part I: Space-time spectra, resolution, and aliasing, *J. Atmos. Sci.*, *39*, 2577–2600, doi:10.1175/1520-0469(1982)039<2577:STFASO>2.0.CO;2.

Salby, M. L., and R. R. Garcia (1987), Transient response to localized episodic heating in the tropics. Part I: Excitation and short-time near-field behavior, *J. Atmos. Sci.*, *44*, 458–498, doi:10.1175/1520-0469(1987)044<0458:TRTLEH>2.0.CO;2.

Sassi, F., and R. R. Garcia (1994), A one-dimensional model of the semiannual oscillation driven by convectively forced gravity waves, *J. Atmos. Sci.*, *51*(21), 3167–3182, doi:10.1175/1520-0469(1994)051<3167:AODMOT>2.0.CO;2.

Sassi, F., and R. R. Garcia (1997), The role of equatorial waves forced by convection in the tropical semiannual oscillation, *J. Atmos. Sci.*, *54*(15), 1925–1942, doi:10.1175/1520-0469(1997)054<1925:TROEWF>2.0.CO;2.

Sassi, F., R. R. Garcia, and B. A. Boville (1993), The stratopause semiannual oscillation in the NCAR Community Climate Model, *J. Atmos. Sci.*, *50*(21), 3608–3624, doi:10.1175/1520-0469(1993)050<3608:TSSOIT>2.0.CO;2.

Sato, K. (1993), Small-scale wind disturbances observed by the MU radar during the passage of Typhoon Kelly, *J. Atmos. Sci.*, *50*(4), 518–537, doi:10.1175/1520-0469(1993)050<0518:SSWDOB>2.0.CO;2.

Sato, K., H. Hashiguchi, and S. Fukao (1995), Gravity waves and turbulence associated with cumulus convection observed with the UHF/VHF clear-air Doppler radars, *J. Geophys. Res.*, *100*(D4), 7111–7119, doi:10.1029/95JD00198.

Scaife, A. A., N. Butchart, C. D. Warner, and R. Swinbank (2002), Impact of a spectral gravity wave parameterization on the stratosphere in the Met Office Unified Model, *J. Atmos. Sci.*, *59*(9), 1473–1489, doi:10.1175/1520-0469(2002)059<1473:IOASGW>2.0.CO;2.

Serafimovich, A., C. Zuelicke, P. Hoffmann, D. Peters, P. Dalin, and W. Singer (2006), Inertia gravity waves in the upper troposphere during the MaCWAVE winter campaign - Part II: Radar investigations and modelling studies, *Ann. Geophys.*, *24*(11), 2863–2875, doi:10.5194/angeo-24-2863-2006.

Shimizu, A., and T. Tsuda (1997), Characteristics of Kelvin waves and gravity waves observed with radiosondes over Indonesia, *J. Geophys. Res. Atmos.*, *102*(D22), 26,159–26,171, doi:10.1029/96JD03146.

Shu, J., W. Tian, D. Hu, J. Zhang, L. Shang, H. Tian, and F. Xie (2012), Effects of the quasi-biennial oscillation and stratospheric semiannual oscillation on tracer transport in the upper stratosphere, *J. Atmos. Sci.*, *70*(5), 1370–1389, doi:10.1175/JAS-D-12-053.1.

Sigmond, M., and J. F. Scinocca (2010), The influence of the basic state on the Northern Hemisphere circulation response to climate change, *J. Climate*, *23*(6), 1434–1446, doi:10.1175/2009JCLI3167.1.

Solomon, S., R. R. Garcia, F. S. Rowland, and D. J. Wuebbles (1986), On the depletion of Antarctic ozone, *Nature*, *321*(6072), 755–758, doi:10.1038/321755a0.

Song, I. S., and H. Y. Chun (2005), Momentum flux spectrum of convectively forced internal gravity waves and its application to gravity wave drag parameterization. Part I: theory, *J. Atmos. Sci.*, *62*, 107–124, doi:10.1175/JAS-3363.1.

Song, I.-S., H.-Y. Chun, and T. P. Lane (2003), Generation mechanisms of convectively forced internal gravity waves and their propagation to the stratosphere, *J. Atmos. Sci.*, *60*(16), 1960–1980, doi:10.1175/1520-0469(2003)060<1960:GMOCFI>2.0.CO;2.

Stober, G., S. Sommer, M. Rapp, and R. Latteck (2013), Investigation of gravity waves using horizontally resolved radial velocity measurements, *Atmos. Meas. Tech.*, *6*(10), 2893–2905, doi:10.5194/amt-6-2893-2013.

Swenson, G. R., and P. J. Espy (1995), Observations of 2-dimensional airglow structure and Na density from the ALOHA, October 9, 1993 'storm flight', *Geophys. Res. Lett.*, *22*(20), 2845–2848, doi:10.1029/95GL02795.

Taylor, M. J., and F. J. Garcia (1995), A two-dimensional spectral analysis of short period gravity waves imaged in the OI(557.7 nm) and near infra red OH nightglow emissions over Arecibo, Puerto Rico, *Geophys. Res. Lett.*, *22*(18), 2473–2476, doi:10.1029/95GL02491.

Taylor, M. J., M. A. Hapgood, and P. Rothwell (1987), Observations of gravity wave propagation in the OI (557.7 nm), Na (589.2 nm) and the near infrared OH nightglow emissions, *Planet. Space Sci.*, *35*(4), 413–427, doi:10.1016/0032-0633(87)90098-5.

Townsend, A. A. (1966), Internal waves produced by a convective layer, *J. Fluid Mech.*, *24*, 307–319, doi:10.1017/S0022112066000661.

Trinh, Q. T., S. Kalisch, P. Preusse, H.-Y. Chun, S. D. Eckermann, M. Ern, and M. Riese (2015), A comprehensive observational filter for satellite infrared limb sounding of gravity waves, *Atmos. Meas. Tech.*, *8*(3), 1491–1517, doi:10.5194/amt-8-1491-2015.

Tsuda, T., Y. Murayama, M. Yamamoto, S. Kato, and S. Fukao (1990), Seasonal variation of momentum flux in the mesosphere observed with the MU radar, *Geophys. Res. Lett.*, *17*, 725–728, doi:10.1029/GL017i006p00725.

Tsuda, T., Y. Murayama, H. Wiryosumarto, S. W. B. Harijono, and S. Kato (1994a), Radiosonde observations of equatorial atmosphere dynamics over Indonesia: 1. Equatorial waves and diurnal tides, *J. Geophys. Res. Atmos.*, *99*(D5), 10,491–10,505, doi:10.1029/94JD00355.

Tsuda, T., Y. Murayama, T. Nakamura, R. A. Vincent, A. H. Manson, C. E. Meek, and R. L. Wilson (1994b), Variations of the gravity wave characteristics with height season and latitude revealed by comparative observations, *J. Atmos. Terr. Phys.*, *56*, 555–568, doi:10.1016/0021-9169(94)90097-3.

Ungermann, J., L. Hoffmann, P. Preusse, M. Kaufmann, and M. Riese (2010), Tomographic retrieval approach for mesoscale gravity wave observations by the PREMIER Infrared Limb-Sounder, *Atmos. Meas. Tech.*, *3*, 339–354, doi:10.5194/amt-3-339-2010.

Ungermann, J., J. Blank, J. Lotz, K. Leppkes, L. Hoffmann, T. Guggenmoser, M. Kaufmann, P. Preusse, U. Naumann, and M. Riese (2011), A 3-D tomographic retrieval approach with advection compensation for the air-borne limb-imager GLORIA, *Atmos. Meas. Tech.*, *4*(11), 2509–2529, doi:10.5194/amt-4-2509-2011.

Vincent, R., and M. Alexander (2000), Gravity waves in the tropical lower stratosphere: An observational study of seasonal and interannual variability, *J. Geophys. Res. Atmos.*, *105*(D14), 17,971–17,982, doi:10.1029/2000JD900196.

Vincent, R. A., and D. C. Fritts (1987), A climatology of gravity wave motions in the mesopause region at Adelaide, Australia, *J. Atmos. Sci.*, *44*(4), 748–760, doi:10.1175/1520-0469(1987)044<0748:ACOGWM>2.0.CO;2.

Vincent, R. A., and A. Hertzog (2014), The response of superpressure balloons to gravity wave motions, *Atmos. Meas. Tech.*, *7*(4), 1043–1055, doi:10.5194/amt-7-1043-2014.

Vincent, R. A., and I. M. Reid (1983), HF Doppler measurements of mesospheric gravity wave momentum fluxes, *J. Atmos. Sci.*, *40*, 1321–1333, doi:10.1175/1520-0469(1983)040<1321:HDMOMG>2.0.CO;2.

Wang, L., and M. J. Alexander (2010), Global estimates of gravity wave parameters from GPS radio occultation temperature data, *J. Geophys. Res. Atmos.*, *115*, doi:10.1029/2010JD013860.

Wang, L., M. A. Geller, and M. J. Alexander (2005), Spatial and temporal variations of gravity wave parameters. Part I: intrinsic frequency, wavelength, and vertical propagation direction, *J. Atmos. Sci.*, *62*, 125–142, doi:10.1175/JAS-3364.1.

Warner, D. C., and M. E. McIntyre (2001), An ultra-simple spectral parameterization for non-orographic gravity waves, *J. Atmos. Sci.*, *58*, 1837–1857, doi:10.1175/1520-0469(2001)058<1837:AUSPFN>2.0.CO;2.

Whiteway, J. A., and A. I. Carswell (1995), Lidar observations of gravity wave activity in the upper stratosphere over Toronto, *J. Geophys. Res. Atmos.*, *100*(D7), 14,113–14,124, doi:10.1029/95JD00511.

Wilson, R., M. L. Chanin, and A. Hauchecorne (1991), Gravity waves in the middle atmosphere observed by Rayleigh lidar: 2. Climatology, *J. Geophys. Res. Atmos.*, *96*(D3), 5169–5183, doi:10.1029/90JD02610.

Wright, C. J., and J. C. Gille (2013), Detecting overlapping gravity waves using the S-Transform, *Geophys. Res. Lett.*, *40*(9), 1850–1855, doi:10.1002/grl.50378.

Wright, C. J., S. M. Osprey, J. J. Barnett, L. J. Gray, and J. C. Gille (2010), High Resolution Dynamics Limb Sounder measurements of gravity wave activity in the 2006 Arctic stratosphere, *J. Geophys. Res.*, *115*, doi:10.1029/2009JD011858.

Wright, J. S., and S. Fueglistaler (2013), Large differences in reanalyses of diabatic heating in the tropical upper troposphere and lower stratosphere, *Atmos. Chem. Phys.*, *13*(18), 9565–9576, doi:10.5194/acp-13-9565-2013.

Wu, D. L., and S. D. Eckermann (2008), Global gravity wave variances from Aura MLS: Characteristics and interpretation, *J. Atmos. Sci.*, *65*(12), 3695–3718, doi:10.1175/2008JAS2489.1.

Wu, D. L., and J. W. Waters (1996a), Satellite observations of atmospheric variances: A possible indication of gravity waves, *Geophys. Res. Lett.*, *23*, 3631–3634, doi:10.1029/96GL02907.

Wu, D. L., and J. W. Waters (1996b), Gravity-wave-scale temperature fluctuations seen by the UARS MLS, *Geophys. Res. Lett.*, *23*, 3289–3292, doi:10.1029/96GL02924.

Wu, D. L., and J. W. Waters (1997), Observations of gravity waves with the UARS Microwave Limb Sounder, *Springer Verlag*, doi:10.1007/978-3-642-60654-0_8.

Wu, D. L., P. Preusse, S. D. Eckermann, J. H. Jiang, M. de la Torre Juarez, L. Coy, B. Lawrence, and D. Y. Wang (2006), Remote sounding of atmospheric gravity waves with satellite limb and nadir techniques, *Adv. Space Res.*, *37*, 2269–2277, doi:10.1016/j.asr.2005.07.031.

Zhu, X. (1994), A new theory of the saturated gravity wave spectrum for the middle atmosphere, *J. Atmos. Sci.*, *51*, 3615–3626, doi:10.1175/1520-0469(1994)051<3615:ANTOTS>2.0.CO;2.